Climate impact of a contrail cirrus outbreak and a novel prediction of relative humidity for weather forecast

Ziming Wang

SIGILL·UNIVERSITAT·LUDOVIC·MAXIM·

München 2024

Printed and/or published with the support of the German Academic Exchange Service

Climate impact of a contrail cirrus outbreak and a novel prediction of relative humidity for weather forecast

Ziming Wang

Dissertation
der Fakultät für Physik
der Ludwig-Maximilians-Universität
München

vorgelegt von
Ziming Wang
aus Xingtai, China

München, den 31. Jan 2024

Erstgutachter: Prof. Dr. Bernhard Mayer
Zweitgutachter: Prof. Dr. Christiane Voigt
Tag der mündlichen Prüfung: 20. Mar 2024

Contents

Zusammenfassung **vii**

Abstract **ix**

Publications **xi**

1 Introduction **1**
1.1 Background and motivation 1
1.2 Scientific topics 6

2 Fundamentals **9**
2.1 Radiative transfer theory 9
2.1.1 Radiative quantities 9
2.1.2 Black body radiation 10
2.1.3 Absorption and scattering 11
2.1.4 Radiative transfer equation 13
2.2 Climate impact of aviation 14
2.2.1 CO_2 and non-CO_2 aviation impact 14
2.2.2 Contrail cirrus formation and persistence 16
2.2.3 Contrail cirrus observations 19
2.3 Ice supersaturated regions 23
2.3.1 Physical definitions 23
2.3.2 Ice supersaturated regions observations 24
2.3.3 Ice supersaturated regions parameterizations in NWP 25
2.3.4 Influential meteorological conditions 27
2.4 Artificial neural networks 28
2.4.1 Multilayer perceptron 28
2.4.2 Training 29
2.4.3 Model interpretation 30

3 Instrumentation, data and methods **33**
3.1 Satellite remote sensing from MSG/SEVIRI 33
3.1.1 CiPS 34

3.1.2 GERB and RRUMS 34
3.2 Airborne measurements 35
3.2.1 In situ and lidar instruments aboard HALO 35
3.2.2 Water vapor measurements from IAGOS 36
3.3 Thermodynamic conditions and dynamical states from ERA5 38
3.4 The libRadtran radiative transfer model 39
3.5 CoCiP contrail cirrus prediction model 40

4 Observations of a contrail cirrus outbreak over the North Atlantic 43
4.1 Microphysical properties of contrail cirrus and natural cirrus 44
4.1.1 General situation 44
4.1.2 Identification of contrails, contrail cirrus and natural cirrus 50
4.1.3 Effective radii 54
4.2 Radiative effects of contrail cirrus and natural cirrus 55
4.2.1 RTM simulations of TOA irradiance 56
4.2.2 Diurnal cycle of TOA RF of the contrail cirrus outbreak 59
4.2.3 Uncertainty of effective radii and ice crystal shape 60

5 Machine learning based improvements of ERA5 humidity predictions 63
5.1 Preparation for the neural network models 64
5.1.1 Input and output data collocation 64
5.1.2 Evaluation of temperature and RHi from ERA5 in the UTLS . . . 66
5.1.3 Correlating model meteorological variables with measured water vapor 68
5.1.4 Training and validation data 70
5.2 Model training 71
5.3 Interpretation of the humidity prediction model 73
5.4 Evaluation of the humidity prediction model 74
5.4.1 Validation in cloud-free and cloudy, lower stratosphere and upper troposphere 74
5.4.2 Validation against CIRRUS-HL measurements 75
5.4.3 Skill of ISSR prediction against IAGOS data 79
5.5 Investigation of the corrected atmospheric radiation budget 81
5.6 Application to other geographic regions and comparisons with the existing method 83

6 Predicted contrail cirrus from improved humidity 87
6.1 Contrail cirrus prediction with improved humidity 87
6.2 Contrail cirrus predictions against MSG observations 90
6.2.1 Macrophysical and optical properties 90
6.2.2 Radiative effects 91
6.3 Small-scale diversion strategy 93

7 Summary, conclusions and outlook 95

A List of abbreviations **107**

Bibliography **115**

Acknowledgements **137**

Zusammenfassung

Kondensstreifen bilden sich in der oberen Troposphäre (UT) durch Aerosolemissionen von Flugzeug und können bei Eisübersättigung bestehen bleiben. Kondensstreifen-Zirren stellen den größten Anteil des wärmenden Nettostrahlungsantriebs (RF) des Luftver-kehrs auf das Klima dar. Die mikrophysikalischen Eigenschaften und Strahlungseffekte von Kondensstreifen-Zirren und natürlichen Zirren unter den gleichen meteorologischen Bedingungen sind jedoch nach wie vor unklar, und die Verteilung von Wasserdampf in der UT und der unteren Stratosphäre (LS) ist mit großen Unsicherheiten behaftet.

In dieser Arbeit wird eine ausgedehnte, durch den Flugverkehr gestörte Zirrusregion im Nordatlantik (NAR) während des Midlatitude Cirrus (ML-CIRRUS) Experiments durch die Kombination von Flugzeugmessungen und geostationären Meteosat Second Generation Satelliten (MSG) Beobachtungen untersucht. Mit einer neuen Methode, die auf in situ Messungen der Eisanzahlkonzentrationen und des NO Gases basiert, wird zwischen Kondensstreifen, Kondensstreifen-Zirren und natürlichen Zirrenunterschieden. Die Effektivradien (R_{eff}) von Kondensstreifen erreichen höchstens 11 µm, während die R_{eff} von Kondensstreifen-Zirren bis zu 51 µm groß sein können. Der mittlere R_{eff} von Kondensstreifen und Kondensstreifen-Zirren ist 18% kleiner als der von natürlichen Zirren. Eine neue Methode zur Schätzung des instantanen RF-Wertes im solaren und thermischen Bereich wird auf der Grundlage von Strahlungstransportrechnungen entwickelt, die in situ und Lidar-Messungen, Satellitenbeobachtungen und Reanalysedaten nutzen. Der Zirrusausbruch wirkt am frühen Morgen wärmend und tagsüber kühlend. Diese Methoden könnten mit einem breiteren Datensatz zur Bewertung der Strahlungswirkung von Zirren und Kondensstreifen angewendet werden.

Um die Vorhersage der Luftfeuchte in Reiseflughöhe zu verbessern, wurde ein neuronales Netz (NN) entwickelt. Das Modell benutzt modellierte thermodynamische Bedingungen und dynamische Zustände aus ERA5-Reanalysedaten als Input und gemessene Luftfeuchte aus den Flugzeugbeobachtungen des In-Service Aircraft for Global Observing System (IAGOS) als Output. Dabei werden frühere (-6, -2 Stunden) mit aktuellen atmosphärischen Zuständen innerhalb von ±2 ERA5-Druckschichten um die Position der IAGOS-Flugzeuge kombiniert. Im Vergleich zu ERA5 verbessert dieser NN-Ansatz die Übereinstimmung zwischen vorhergesagter und beobachteter relativer Feuchte über Eis, mit einer Erhöhung der Korrelation um bis zu 0,25 und einer Verringerung des mittleren absoluten Fehlers um bis zu 9,07%. Die prognostizierte relative Feuchte des ANN-Ansatzes stimmt besser mit unabhängigen Flugzeugmessungen überein. Die Steigerung der Genauigkeit für die Vorhersage von Eisübersättigung beträgt etwa 43% in NAR im Jahr 2020. Eine erhöhte Feuchte in der LS, zusammen mit einer Verringerung in der UT, führt zu einem stärkeren Erwärmungseffekt des Wasserdampfs an der Oberfläche und zu einem schwächeren Erwärmungseffekt in der UTLS. In einem Testfall stimmen die simulierten Strahlungseffekte der Kondensstreifen besser mit den MSG-Beobachtungen überein als die Ergebnisse ohne Korrektur der Feuchtevorhersage. Dabei nehmen die optische Dicke und der RF-Wert des Kondensstreifens zu. Dank dieser Methode können Maßnahmen zur Kondensstreifenvermeidung effizienter durchgeführt werden.

Abstract

Contrails form in the upper troposphere (UT) from aircraft aerosol emissions and can persist in ice supersaturation conditions. Contrail cirrus constitute the largest net warming radiative forcing (RF) component to the total aviation effect on climate. However, microphysical properties and radiative effects of contrail cirrus and natural cirrus in the same meteorological conditions remain unclear, and the distribution of water vapor in the UTLS is subject to large uncertainties. The contrail cirrus radiative impact is still not completely resolved in remote sensing and climate modelling.

An extended cirrus region perturbed by aviation in the North Atlantic region (NAR) during the Midlatitude Cirrus (ML-CIRRUS) experiment is then investigated by combining airborne and geostationary Meteosat Second Generation satellite (MSG) observations. A new method for in situ measurements was used to distinguish between contrails, contrail cirrus and natural cirrus based on ice number and NO gas concentrations. Contrail effective radii (R_{eff}) reach at most 11 µm, while contrail cirrus R_{eff} can be as large as 51 µm. Contrail and contrail cirrus mean R_{eff} is 18% smaller than that of natural cirrus in this case. A new method to estimate top-of-atmosphere instantaneous RF in the solar and thermal range is developed based on radiative transfer model simulations exploiting in situ and lidar measurements, satellite observations and reanalysis data. For a larger spatial area around the flight path, the contrail cirrus outbreak is warming in the night and early morning and cooling during the day. This study could be applied to a broader data set for the assessment of radiative impacts of cirrus and contrail cirrus.

To improve the humidity prediction at the cruise levels, a novel approach is developed utilizing artificial neural networks (ANN). The model combines relevant parameters including modelled thermodynamic conditions and dynamical states from ERA5 reanalysis data as input, and measured humidity from the In-Service Aircraft for Global Observing System (IAGOS) aircraft observations as output. Correlation analyses indicate that the combination of previous (-6, -2 hour) and current atmospheric states within ±2 ERA5 pressure layers around the IAGOS flight latitude shows the high predictive skill for the current humidity status. Compared with ERA5, the ANN approach improves the consistency between predicted and observed humidity from IAGOS in cloudy and cloud-free UT and lower stratosphere (LS), with an increase in correlation by up to 0.25 and a decrease of mean absolute error up to 9.07% and 0.03 g/kg for relative humidity and specific humidity, respectively. The predicted relative humidity from the ANN approach shows better agreement to independent airborne measurements. The increase of the accuracy for ice supersaturation forecast is about 43% over NAR in 2020. An increased specific humidity in the LS but a decrease in the UT induce a stronger warming effect at the surface and a locally weaker warming effect of water vapor in the UTLS. The simulated contrail cirrus radiative effects better compares to MSG observations than the results without humidity forecast correction. In a test case, optical thickness and contrail RF increase for the improvements of humidity prediction. For contrail mitigation, the diversion of flights to avoid ice supersaturation can be implemented with higher efficiency when the ANN method is applied to weather forecast products.

Publications

Parts of the results and text in this thesis have been published, to be submitted, and under review in the following papers:

Wang, Z., Bugliaro, L., Jurkat-Witschas, T., Heller, R., Burkhardt, U., Ziereis, H., Dekoutsidis, G., Wirth, M., Groß, S., Kirschler, S., Kaufmann, S., and Voigt, C.: Observations of microphysical properties and radiative effects of a contrail cirrus outbreak over the North Atlantic, Atmos. Chem. Phys., 23, 1941–1961, https://doi.org/10.5194/acp-23-1941-2023, 2023.

Differences in the microphysical properties of contrail cirrus and natural cirrus in a contrail outbreak situation during the ML-CIRRUS campaign over the North Atlantic flight corridor can be observed from in situ measurements. The cirrus radiative effect in the area of the outbreak, derived from satellite observation-based radiative transfer modeling, is warming in the early morning and cooling during the day.

Wang, Z., Bugliaro, L., Hegglin, M. I., Gierens, K., Rohs, S., Petzold, A., Schumann, U., Kaufmann, S., Mayer, B., and Voigt, C.: Dynamic-based improvement of atmospheric humidity in the upper troposphere and lower stratosphere using machine learning, in preparation. This relative humidity correction work is planned for publication after the submission of the thesis.

Sensitivity analyses addressed how the actual atmospheric states influence the future evolution of humidity fields. Thus, an artificial neural network (ANN) model was built using modeled meteorological conditions particularly dynamical quantities with their temporal evolution and the corresponding measured humidity. The predicted humidity shows better agreement to measurements and higher capability to predict ice supersaturation, which can be applied to forecast humidity status and simulate corrected atmospheric water vapor radiation budget and contrail cirrus climate impact.

Wang, Z., Letu, H., Shang, H., and Bugliaro, L.: Technical note: Retrieval of the supercooled liquid fraction in mixed-phase clouds from Himawari-8 observations, Atmos. Chem. Phys., minor revision, https://doi.org/10.5194/egusphere-2023-2667, 2024.

The liquid droplet and ice particle radiative properties are used to derive the microphysics and differentiate supercooled and ice fraction. Supercooled liquid fraction is retrieved for the first time for mixed-phase clouds in the pixel level using passive geostationary satellite observations. The retrieved supercooled liquid fraction is well comparable to CALIPSO-GOCCP lidar products, and is capable of presenting the variation of supercooled liquid fraction in mixed-phase clouds in different cloud regimes.

Chapter 1

Introduction

1.1 Background and motivation

Condensation trails (contrails) are line-shaped ice clouds generated by jet aircraft in the upper troposphere at 8-13 km altitude. Depending on whether retaining the linear shape, they are referred to persistent contrails and contrail cirrus, respectively. Figure 1.1 depicts a contrail cirrus outbreak characterized by linear-shaped contrails (white lines), forming over the North Atlantic Region (NAR), extending southeast towards the European continent, and passing over Belgium, the Netherlands, Spain, and Germany. The observation is captured by the geostationary Meteosat Second Generation (MSG)/Spinning Enhanced Visible and InfraRed Imager (SEVIRI).

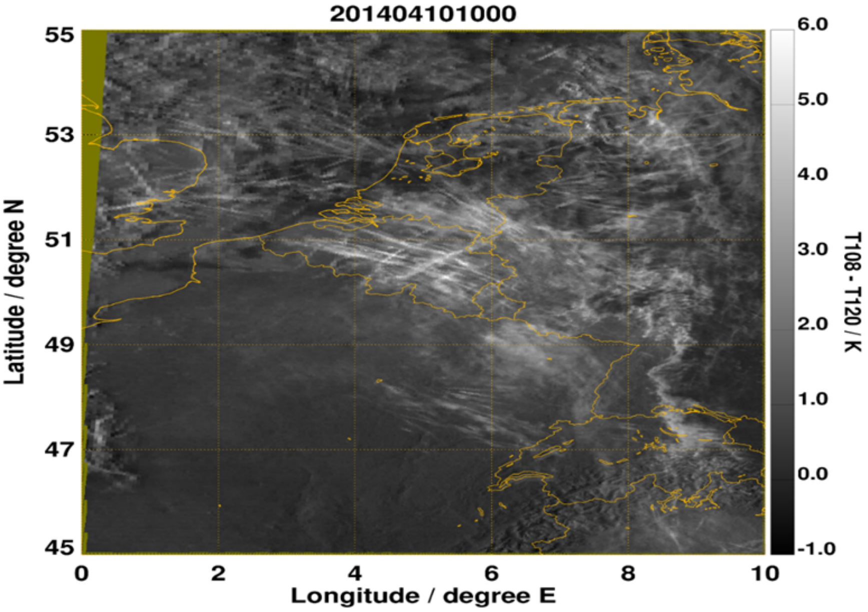
201404101000
55
53
51
49
47
45
Latitude / degree N
0
2
4
6
8
10
Longitude / degree E
6.0
5.0
4.0
3.0
2.0
1.0
0.0
-1.0
T108 - T120 / K

Figure 1.1: Brightness temperature difference image (10.8 µm and 12.0 µm) obtained from the SEVIRI sensor on the MSG-3 satellite. The image is at 10:00 UTC on 10 April 2014.

By reflecting incident solar radiation and trapping upwelling radiation within the Earth's atmosphere, contrail cirrus result in an imbalance of radiation budget in both the shortwave (SW) solar and longwave (LW) terrestrial spectrum [Stuber et al., 2006]. Thereby the contrail cirrus radiative forcing (RF) describes the change of the energy budget at the top of the atmosphere (TOA) or in the Earth-atmosphere system due to a perturbation of aircraft aerosol emissions [Lee et al., 2009]. Recent studies, for instance Lee et al. [2021], suggest that the effective radiative forcing (ERF) from contrail cirrus, which takes into account atmospheric adjustments, accounts for almost two thirds of net positive RF from aviation (all terms) and can be larger than the climate impact from aviation CO2 emissions (Figure 1.2). Only a small percentage of the flights worldwide [Teoh et al., 2023] contributes strongly to global contrail cirrus RF [Burkhardt and Kärcher, 2009], many of them associated with long-lived contrail cirrus outbreaks [Burkhardt et al., 2018]. Thus, the significant climate impact of contrail cirrus from aviation serves as the motivation for this thesis to investigate the contrail cirrus outbreak and explore potential strategies for contrail avoidance.

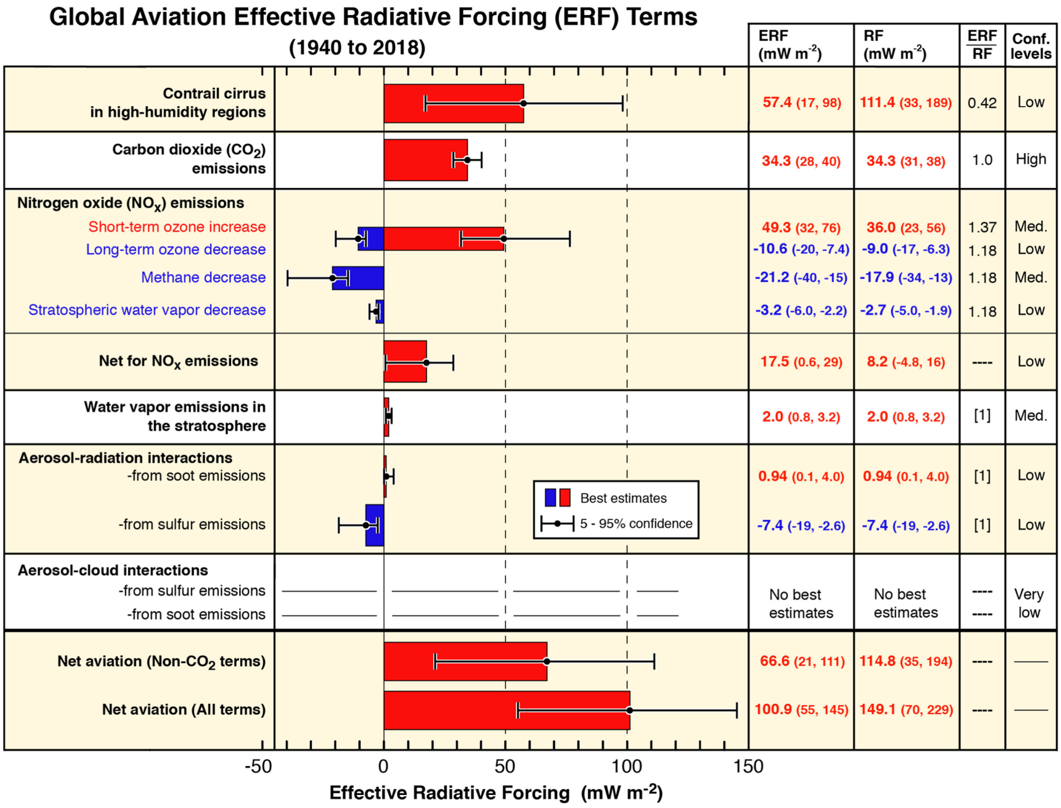

Figure 1.2: Climate forcing terms from global aviation from 1940 to 2018. The bars and whiskers show ERF best estimates and the 5–95% confidence intervals, respectively. Red bars indicate warming terms and blue bars indicate cooling terms. Numerical ERF are given in the columns with 5–95% confidence intervals along with ERF and confidence levels. From Lee et al. [2021].

Contrails form when the hot and humid jet engine exhaust at cruise levels mixes with the cool ambient atmosphere [Schumann, 1996]. The emitted soot particles act as condensation nuclei to form liquid droplets that freeze subsequently into ice crystals as the young contrails [Kärcher, 2018]. Ice supersaturated regions (ISSRs), with relative humidity with respect to ice (RHi) larger than 100%, support the growth, suppress the sublimation, and influence the deposition rate and further the sedimentation of ice crystals. In ISSRs, persistent contrails grow and spread out to form contrail cirrus [Schumann et al., 2017]. Natural cirrus are also high level clouds composed of ice crystals that form and evolve in ISSRs [Minnis et al., 2004]. The difference of microphysical properties and radiative effects of natural cirrus and contrail cirrus and their evolution are still subject of current research.

Airborne measurements and spaceborne observations have provided detailed properties of contrails and contrail cirrus. Contrail cirrus can be detected and separated from natural cirrus to some extent in in situ measurements by combining ice crystal microphysical data with observations of aircraft emissions such as nitrogen oxides (NO_x) or aerosols [Voigt et al., 2017]. Heymsfield et al. [2010a] provides a comprehensive overview of contrail and contrail cirrus properties and extensive data sets exist on their microphysical properties, their particle shapes [Gayet et al., 2012] and optical properties [Chauvigné et al., 2018], as well as the influence from aircraft on ice crystal number in cirrus [Jeßberger et al., 2013]. From satellite observations, linear contrails can be detected with polar orbiting and geostationary satellites [Mannstein et al., 2010]. Thanks to their high temporal resolution, contrails can be tracked [Vazquez-Navarro et al., 2010] and their LW and SW RF can be estimated [Vázquez-Navarro et al., 2015]. Some studies have taken the NAR and North America with the largest air traffic density as target regions, and analysed the temporal evolution of contrail cirrus coverage, outgoing radiation, and properties [Schumann et al., 2013]). Early climate models estimated contrail cirrus RF through associating air traffic with regional cirrus coverage and assumed equal radiative efficiencies of contrails and contrail cirrus [Stordal et al., 2005]. Subsequently, the numerical and global climate models represent contrail cirrus as a separate cloud class [Schumann, 2012, Bock and Burkhardt, 2016a].

Despite substantial progress in recent years, the characterization of geometrical, optical, and microphysical properties of contrails and their evolution within natural cirrus fields [Voigt et al., 2021] as well as the calculation of the radiative impact [Grewe et al., 2017] are still subject to large uncertainties partly due to the large number of variables, for example RHi, influencing the contrail life cycle [Kaufmann et al., 2018].

The upper troposphere and lower stratosphere (UTLS) are of special interest for investigations of microphysical properties of both contrail and natural cirrus clouds and their associated atmospheric RF. Cirrus in this region can survive for hours if the surrounding RHi is larger than 100%. However, the distribution of water vapor in the UTLS is subject to large uncertainties, even with the enhanced ISSRs parameterized scheme including the cloud glaciation process in the forecast model [Tompkins et al., 2007]. A significant wet bias in the lower LS humidity has been identified in the operational European Centre for Medium-Range Weather Forecasts (ECMWF) forecast and analysis data when compared with in situ measurements from the Midlatitude Cirrus [ML-CIRRUS, Voigt et al., 2017] experiment [Kaufmann et al., 2018], and Civil Aircraft for the Regular Investigation of the atmosphere Based on an Instrument Container (CARIBIC) passenger aircraft flights [Dyroff et al., 2015] (Figure 1.3). In contrast, a dry bias of RHi is observed in the UT from lidar measurements on aircraft [Krüger et al., 2022]. The assimilation of in situ measurements, radiosonde data sets and satellite observations into the numerical weather prediction (NWP) model is the state-of-the-art way to improve the weather forecast [Lawrence et al., 2019, van der Linden et al., 2020]. However, the procedure of saturation adjustment, where supersaturation relaxes to saturation if cloud formation occurs, still leads to the systematic underestimation of the frequency and degree of ISSRs at cruise altitudes in NWPs [Sperber and Gierens, 2023].

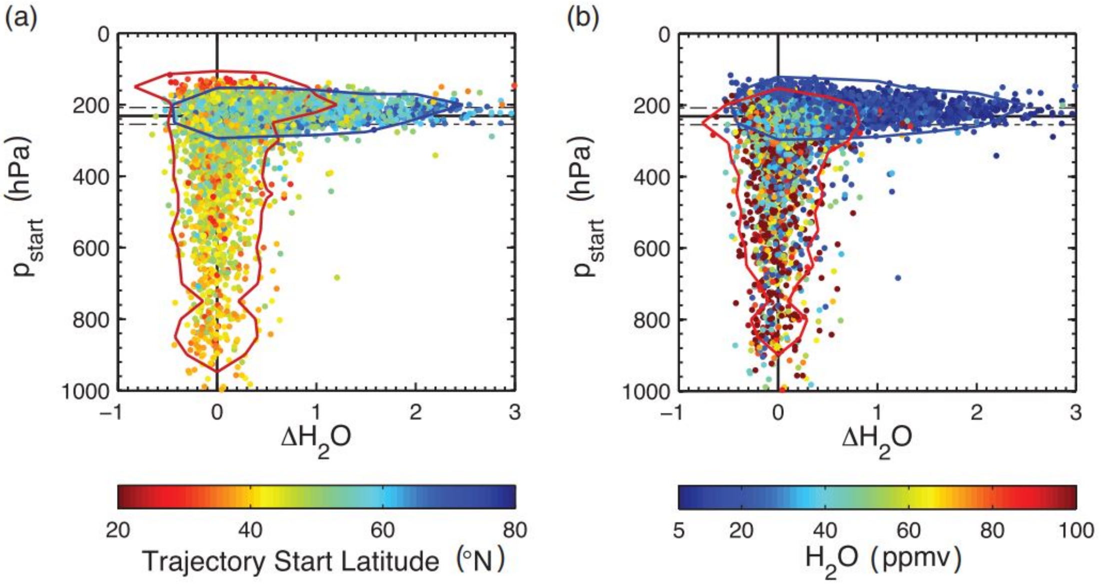

Figure 1.3: (a) Dependence of model bias on the pressure of the airmass five days prior to sampling as determined by backwards trajectory analyses. The contour lines depict the area in which 90% data of the two latitude bins 20–30°N (red) and 70–80°N (blue) fall. The horizontal solid line represents the mean sampling pressure. (b) same as for (a), however using H2O gas as colour code. Contour lines indicate where 90% of the data fall within the humidity bins < 10 ppmv (blue) and > 50 ppmv (red). From Dyroff et al. [2015].

The accurate prediction of humidity is a prerequisite for simulating contrail formation and persistence, and implementing contrail avoidance strategies. ISSRs typically have large horizontal (150 ± 250) km but shallow vertical extensions [Spichtinger et al., 2003]. Therefore, in the short term, a slight, weather-dependent adjustment in cruising altitude (±600 m) could minimize the flight distance within regions characterized by high humidity and warming contrails, thereby reducing the contrail lifetime and ERF. Unlike the gradual transition to sustainable aviation fuel or hydrogen-based combustion, a flight optimization strategy could eventually be implemented without substantial technological changes. In order to achieve this goal, current weather forecasts have to demonstrate their capability to predict ISSRs for warming contrails with a certain degree of accuracy. However, as discussed before, the distribution of ISSRs in the UTLS is subject to large uncertainties.

Gierens and Brinkop [2012] and Gierens et al. [2020] investigate the typical distributions of dynamical fields within ISSRs, and infer that accurate prediction of ice supersaturation, particularly for the associated strong contrails, may be possible by incorporating the dynamical state of the ambient atmosphere through general regression. Teoh et al. [2022a] use in situ measurements from In-Service Aircraft for Global Observing System (IAGOS) to develop a new RHi correction methodology, which confirms that the probability density function of ERA5-derived RHi inside ISSRs resembles the IAGOS measurements. Their simulated contrail cirrus net RF in NAR in 2019 exhibits a notable sensitivity to this ERA5 humidity correction (Figure 1.4). The estimated contrail cirrus net RF is doubled from simulations where the correction is applied. Kadow et al. [2020] has demonstrated the skill of artificial intelligence (AI) in improving observational surface temperatures when combined with climate model data. Lam et al. [2023] also suggests that AI could serve as an effective approach to mitigate uncertainties and biases in weather forecasting including atmospheric humidity fields.

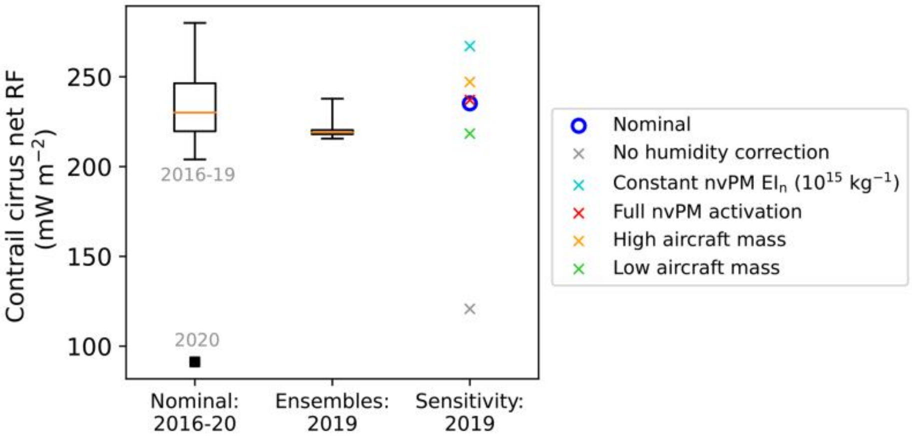

Figure 1.4: Comparisons of the contrail cirrus net RF in the NAR provided by the nominal simulations using ERA5 and the sensitivity analyses for 2019. From Teoh et al. [2022a].

A more comprehensive understanding of the origin of the humidity bias in the UTLS can contribute to the improvements of humidity prediction. Backward trajectories analyses from Dyroff et al. [2015], as shown in Figure 1.3, indicate that the moist bias is linked to air masses originating from high northern latitudes at the aircraft flight level. In the vertical direction, part of the model bias arises from small-scale stratospheric intrusions that remain unresolved by the model but are frequently observed features in the UTLS. Riese et al. [2012] and Krüger et al. [2022] further point out the connection between uncertainties in atmospheric mixing and the simulated composition of water vapor in the UTLS, along with its associated radiative effects.

The ambition of this thesis is to resolve the microphysical properties and radiative effects of natural cirrus, contrail cirrus and contrails in the same meteorological conditions, and improve the RHi forecast based on AI in the UTLS region to identify the climate impact of contrail cirrus for the research applications. Although some of the previous work have included the analysis of natural cirrus and contrail cirrus simultaneously, the evolution of contrails is still an open question. The large majority of the previous humidity correction is limited to regression fitting, during which the vertical stratospheric intrusions and horizontal airmass transport which lead to the humidity bias are less discussed.

1.2 Scientific topics

The main limiting factors for investigating microphysical properties and radiative effects of contrail cirrus and ambient natural cirrus in an contrail cirrus outbreak have been the small spatial scale of airborne measurements as well as the low spatiotemporal resolution of polar orbiting satellite instruments. The first part of this thesis aims to combine the detailed in situ data sets and lidar profiling and the large spatial scale and high temporal resolution of geostationary satellite observations (required to study the variation of the contrail cirrus outbreak) with a new cirrus classification method and a radiative transfer model (RTM) based TOA irradiance estimation algorithm. Large uncertainties for predicting the contrail cirrus life cycle and their climate impact stem from insufficient knowledge about atmospheric humidity at cruise levels. Here, satellite observations do not have the sufficient horizontal resolution for strong gradients in temperature and water vapor at the tropopause, and few models are able to predict the related short temporal scales and fast spatial development. Thus, the goals of this thesis also involve the improvement of the RHi prediction based on modelled parameters from ERA5 and measured water vapor from airborne campaigns using a machine learning technique. These efforts allow for a comprehensive and quantitative analysis of the microphysical properties and radiative effects of the contrail cirrus outbreak, and a significant advancement of RHi forecast for the estimation of the cirrus cloud life cycle and climate impact, as well as atmospheric water vapor radiation budget.

While much of the previous work on contrail cirrus and natural cirrus clouds has focused on their separate microphysical properties and radiative effects, the strength and novelty of this study is the combination of detailed in situ and lidar measurements (from the German High Altitude and LOng range research aircraft HALO) together with the large spatial coverage and high temporal resolution from a geostationary imager. This results in a new cirrus identification and RF retrieval algorithm, that allows for distinguishing natural cirrus, contrail cirrus and contrails in similar meteorological conditions from in situ measured cloud particle properties and enhanced Nitric oxide (NO) aircraft gas emissions, and for computing the corresponding RF, derived by satellite observations, atmospheric profiles of trace gases and natural clouds from ERA5, and RTM in a favourable air traffic region with a temporal resolution up to 5 min. This provides a quantitative analysis of the cirrus microphysical properties and radiative effects throughout the diurnal cycle of the outbreak and makes it possible to address scientific questions related to the physical processes of contrails. Thus, the following scientific question is addressed:

1. What are the microphysical properties and radiative effects of contrail cirrus and natural cirrus in a contrail cirrus outbreak?

For the identified cirrus classes ice crystal properties are estimated and related to RHi. It is suggested that the ISSRs where RHi is larger than 100% provide the water vapor for the growth of the ice crystals, while they prevent the sublimation, and affect the deposition rate and further the efficiency of sedimentation. Currently, widely used modelled humidity data records have large uncertainties in the UTLS region, which are due not only to thermodynamic conditions but also to dynamical processes. While the humidity correction from regression fitting between modelled humidity and long term and large scale humidity measurements has been presented in the literature, this thesis aims to improve humidity data records more accurately through building an artificial neural networks (ANN) algorithm between modelled thermodynamic conditions and previously neglected but crucial dynamical states from ERA5 as well as measured water vapor from IAGOS, allowing for the evaluation of changes in the atmospheric water vapor radiation budget. Hence, the following scientific question is addressed:

2. Is there a possibility to improve the RHi prediction from ERA5 with thermodynamic conditions and dynamical states?

To further investigate the prediction of contrails and their climate impact with the improved humidity using Contrail Cirrus Prediction model CoCiP simulations and satellite observations, the following scientific question is finally addressed:

3. How does an improved prediction of RHi influence the predicted climate impact of contrail cirrus?

To approach and answer these scientific questions, this thesis is divided into six chapters. Chapter 2 describes the theoretical background of this study including the radiative transfer theory, climate impact of aviation, ISSRs, and ANN. The satellite remote sensing, airborne measurements, data and methods used in this study are introduced and described in Chapter 3. Chapter 4 shows the observations of a contrail cirrus outbreak over the NAR (SQ-1). Chapter 4.1 describes a novel cirrus classification method and the further analysis of microphysical properties of natural cirrus, contrail cirrus and contrails, while the RF estimation of the contrail cirrus outbreak is presented in Chapter 4.2. Chapter 5 displays the improved relative humidity prediction (SQ-2). First, the preparation of the data sets and the model training are described in Chapter 5.1 and 5.2. Second, the humidity prediction model is interpreted and validated with independent data sets in Chapter 5.3 and 5.4. Third, the new atmospheric radiation budget induced from water vapor is investigated in Chapter 5.5, and other applications and comparisons with the existing method are shown in Chapter 5.6. Chapter 6 compares contrail cirrus from improved relative humidity to satellite observations (SQ-3). Finally, the conclusions drawn from this study together with an outlook on how to transfer my data evaluation techniques to future studies are presented in Chapter 7.

Chapter 2

Fundamentals

2.1 Radiative transfer theory

The physical phenomenon of energy transfer in the form of electromagnetic radiation through the atmosphere is called *atmospheric radiative transfer*. The radiation is propagated through a medium and affected by absorption, emission, and scattering processes. The foundations of the radiative transfer theory for this thesis, based mainly on Liou [2002] and Mayer and Kylling [2005], are summarized in this Chapter for the understanding and interpretation of satellite remote sensing.

2.1.1 Radiative quantities

Electromagnetic radiation can be described as a wave or as a stream of photons. The wave properties are characterised with its *frequency* ν (in s^{-1} or Hz) by the speed of light c at which it oscillates and its wavelength λ (the distance between two peaks, in the context of atmospheric radiation usually in nm or µm)

$$\nu = \frac{c}{\lambda} \,, \tag{2.1}$$

where c is the constant propagation velocity of the electromagnetic radiation in vacuum. The energy E (in J) of a photon is described by the *Planck-Einstein relation*

$$E = h\nu = \frac{hc}{\lambda} \,, \tag{2.2}$$

where h = 6.626×10^{-34} Js is the Planck constant. Since c and h are constants, the electromagnetic radiative energy is directly related to the wavelength and frequency.

Depending on wavelength, electromagnetic radiation is qualitatively categorized in major spectral ranges. The wavelengths at ca. 400–700 nm are called the visible spectrum. Longer wavelengths of 0.7–1000 µm are defined as the infrared spectrum, which includes the ranges of the near infrared at 0.7–1.4 µm, short-wavelength infrared at 1.4–3.0 µm, mid-wavelength infrared at 3.0–8.0 µm, long-wavelength infrared at 8.0-15.0 µm, and the far infrared at 15.0–1000 µm. This study focuses on measurements in the spectral ranges mentioned above.

The *radiant flux* Φ (in W) describes the radiant energy per unit time

$$\Phi = \frac{dE}{dt} \ . \tag{2.3}$$

And the *irradiance* I (in $\mathrm{W\,m^{-2}}$) describes the radiant flux received by or leaving a surface element dA per unit area:

$$I = \frac{dE}{dAdt} \ . \tag{2.4}$$

dA is used to define the polar coordinate system such that the zenith angle θ is the angle between the normal of the polar coordinate system dA and the direction towards the solid angle $d\Omega$. The normal vector points in the direction given by θ and the azimuth angle, and the *radiance* L (in $\mathrm{W\,m^{-2}\,s^{-1}}$) is corrected by a factor $\cos(\theta)$ to project dA parallel to the surface. Here, the *radiance* L describes the radiant flux received by or leaving a surface element dA per solid angle per area per time:

$$L = \frac{dE}{\cos(\theta) d\Omega dAdt} \ . \tag{2.5}$$

Finally, the *spectral radiance* L_λ (in $\mathrm{W\,m^{-2}\,s^{-1}\,nm^{-1}}$) describes the *radiance* L at a given wavelength

$$L_\lambda = \frac{dE}{\cos(\theta) d\Omega dAd\lambda dt} \ . \tag{2.6}$$

2.1.2 Black body radiation

All bodies absorb and emit electromagnetic radiation. A black body is an idealised object that absorbs all incident electromagnetic radiation. The approximation of a black body is a cavity: radiation enters, and is reflected inside again and again until it is finally absorbed. The emitted radiance (in $\mathrm{W\,m^{-2}\,s^{-1}\,nm^{-1}}$) of a black body is described by *Planck's law*,

$$B_\lambda(T) = \frac{2hc^2}{\lambda^5(e^{\frac{hc}{\lambda k_B T}} - 1)} \ , \tag{2.7}$$

where $k_B = 1.381 \times 10^{-23}\,\mathrm{JK^{-1}}$ is the Boltzmann constant. The spectral black body radiance B_λ is a function of the black body temperature T and independent of any other property of the black body. Black bodies only exist in theory. A real object (so-called *grey body*) at temperature T emits only a fraction of the electromagnetic radiation, and the emissivity ϵ_λ is introduced as

$$\epsilon_\lambda = \frac{L_\lambda}{B_\lambda(T)} \tag{2.8}$$

with $\epsilon_\lambda = 1$ for a black body but $\epsilon_\lambda < 1$ for a grey body. The absorptivity α_λ, reflectivity R_λ and transmissivity T_λ are defined as the ratios between the absorbed, reflected or transmitted radiance, respectively, and the incoming radiance. The Kirchhoff's law is derived under the condition of a thermodynamic equilibrium

$$\alpha_\lambda = \epsilon_\lambda \ . \tag{2.9}$$

2.1.3 Absorption and scattering

In the atmosphere, atmospheric molecules, including gas, aerosols, cloud droplets and ice crystals interact with the radiation through absorption, emission and scattering processes.

Absorption describes the process when an atom or molecule extracts energy from the incident beam of radiation according to Eq. 2.2 and transits to a discrete higher energy level, leading to the characteristic spectral lines and bands of given atoms and molecules. Processes require energy and hence lead to photon absorption including changes in molecular vibrational and rotational motion as well. **Emission** describes the process opposite to **absorption**.

Important atmospheric gases in Figure 2.1 are water vapor, carbon dioxide and ozone, with water vapor producing an absorption band around 6.3 µm, carbon dioxide around 4.3 µm and especially 15 µm, and ozone around 9.6 µm. Furthermore, the influences from other gases are comparably small such that they can be neglected when considering a broad-band radiometer. The spectral region 8 – 12 µm is called *atmospheric window*, as it is mostly transparent except for ozone. The window reveals a fragmented portion extending from the ultraviolet to mid-wavelength infrared, spanning the range of 0.2 to 5.5 µm.

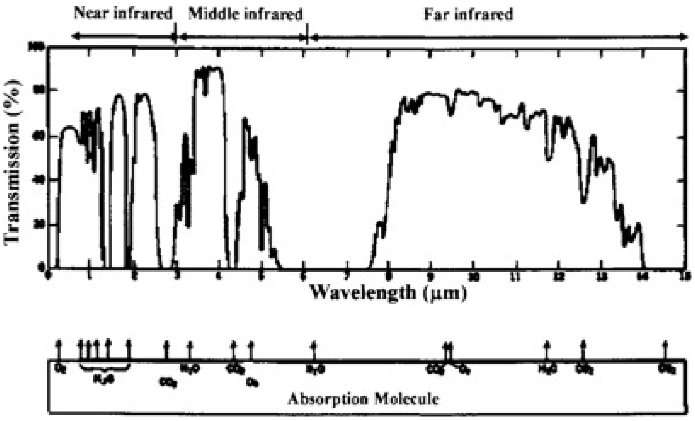

Figure 2.1: A clear electromagnetic spectral transmission window can be seen between 8 and 12 µm in the main window spectrum. A fragmented part of the window spectrum is also shown in the ultraviolet to mid-wavelength infrared between 0.2 and 5.5 µm. From Jiang and Razeghi [2002].

Scattering describes the redirection of electromagnetic radiation from the direction of propagation [Efremenko and Kokhanovsky, 2021]. How the incident radiation is scattered depends on the wavelength and the properties of the scattering molecule or particle (*complex refractive index*, shape, size). Herein, the bulk properties of solids and liquids relevant to absorption and scattering are given by the *complex refractive index* m

$$m = n + ik \ , \tag{2.10}$$

where the real and imaginary parts n and k of the *complex refractive index* indicate the ability of scattering and absorption, respectively. Liquid water clouds and cirrus clouds composed of large droplets and ice crystals are similar to black bodies in the atmospheric window, whereas thin cirrus clouds of small particles (i.e., $R_{eff} < 30\,\mu\text{m}$) have a size-dependent absorption peak around 12 µm which results in a spectral signature that can be used for cloud phase discrimination and cloud detection [Smith et al., 1998].

The *size parameter* x describes the relationship between the wavelength of the incoming electromagnetic radiation λ and the radius of a scattering particle r,

$$x = \frac{2\pi r}{\lambda} \ . \tag{2.11}$$

Figure 2.2 shows the scattering pattern of electromagnetic radiation with $\lambda = 0.5\,\mu\text{m}$ scattered by spherical particles with three different sizes. Larger particles lead to the scattered radiation in the forward direction, with increasingly complex scattering patterns. The angular re-distribution of scattered radiation from the incident direction Ω' to the direction Ω is described by the scattering phase function $P(\Omega', \Omega)$.

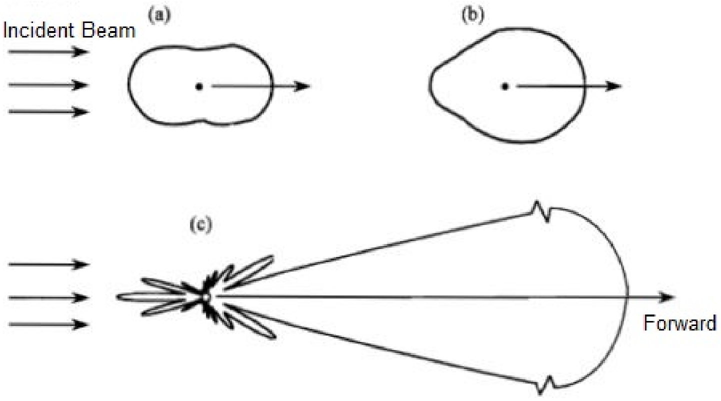

Figure 2.2: The angular distribution of visible radiation at 0.5 µm by spherical particles of three sizes: (a) 10^{-4} µm, (b) 0.1 µm and (c) 1 µm. The forward scattering pattern for the 1 µm particle is extremely large and is scaled here. Figure adapted from Liou [2002].

For spherical objects with $x > 1$ or x $\approx$ 1, the Lorenz-Mie scattering is referred to, and the corresponding theory can be derived directly from Maxwell's equations. The strong scattering is exhibited in the forward direction and is roughly wavelength-independent. Spherical aerosol particles and cloud droplets (with sizes of roughly 1–10 µm) can be treated with Lorenz-Mie theory. For $x \ll 1$, Lorenz-Mie scattering simplifies to Rayleigh scattering. Rayleigh scattering leads to a radiance being proportional to λ^{-4} and equal scattering in forward and backward direction. This approximation is applied to gas molecules (a $\approx 1 \times$

10^{-4} µm). For $x \gg 1$, scattering can be described by geometric optics, i.e., light can be modeled by parallel rays and refracted according to Snell's law. This simplification can be used for raindrops ($r \approx 1\,\mathrm{cm}$) and large ice particles.

In contrast to approximately spherical cloud liquid water droplets, cloud ice crystals have a variety of more complex shapes. The scattering properties of ice crystals can be derived for a set of idealised crystal shapes, e.g. plates, columns, bullet rosettes, droxtals, and aggregates, for a range of sizes using various methods (e.g. geometric optics, T-matrix, finite difference time domain). The total scattering effect can then be estimated by averaging the scattering properties over multiple size distributions with prescribed crystal shapes (see e.g. Yang et al. [2015]).

Independent of the method, a set of optical properties parameterizes the scattering and absorption properties. The absorption and scattering cross sections σ_{abs} and σ_{sca} are defined as the ratio between the radiance absorbed or scattered (in all directions), respectively, by the molecule or particle and the incident radiance. The unit of a geometrical area represents the effective area of the object presented to the incident beam with respect to scattering and absorption. The extinction cross section σ_{ext} is the sum of both, i.e.,

$$\sigma_{ext} = \sigma_{abs} + \sigma_{sca} \ . \tag{2.12}$$

The extinction coefficient β_{ext} is defined as

$$\beta_{ext} = \sigma_{ext} n \ , \tag{2.13}$$

with n denoting the particle number density. Similar relations for the absorption and scattering coefficients β_{abs} and β_{sca} are given by

$$\beta_{ext} = \beta_{abs} + \beta_{sca} \ . \tag{2.14}$$

The single scattering albedo ω is given by

$$\omega = \frac{\beta_{sca}}{\beta_{ext}} = \frac{\beta_{sca}}{\beta_{abs} + \beta_{sca}} \ . \tag{2.15}$$

And τ is known as the *optical depth* of the atmospheric path length s

$$\tau = \int \beta_{ext} \, ds \ . \tag{2.16}$$

2.1.4 Radiative transfer equation

A beam of electromagnetic radiation propagating through an atmospheric volume with the infinitesimal thickness ds loses energy due to absorption and scattering. The combined loss in energy in length due to absorption and scattering is quantified by the Beer-Lambert-Bouguer law and given by

$$\frac{dL_{ext,\lambda}}{ds} = -\beta_{ext,\lambda} L_{\lambda} \ . \tag{2.17}$$

The beam also gains radiant energy along the direction of propagation due to emission by the medium. A body with a temperature T emits radiation in all directions according to Planck's law (Eq. 2.7). Assuming local thermodynamic equilibrium and invoking Kirchhoff's law, the gain in spectral radiance due to emission along the path length is given by

$$\frac{dL_{emi,\lambda}}{ds} = \beta_{abs,\lambda} B_\lambda(T) \ , \tag{2.18}$$

where $\beta_{abs,\lambda}$ is the emission (absorption) coefficient of the medium.

Finally, the beam can gain energy if radiation from the outside is scattered into the direction of propagation. The gain in spectral radiance due to scattering from an arbitrary direction Ω' into the direction of propagation Ω is given by

$$\frac{dL_{sca,\lambda}(\Omega', \Omega)}{ds} = \beta_{sca,\lambda} P(\Omega', \Omega) L_\lambda(\Omega') \ . \tag{2.19}$$

Integrating over all incident angles Ω' yields

$$\frac{dL_{sca,\lambda}(\Omega)}{ds} = \frac{\beta_{sca,\lambda}}{4\pi} \int_{4\pi} P(\Omega', \Omega) L_\lambda(\Omega') \, d\Omega' \ . \tag{2.20}$$

Combining Eqs. 2.17, 2.18 and 2.20, the equation of radiative transfer can be formulated as

$$\begin{aligned} \frac{dL_\lambda}{ds} &= \frac{dL_{ext,\lambda}}{ds} + \frac{dL_{emi,\lambda}}{ds} + \frac{dL_{sca,\lambda}(\Omega)}{ds} \\ &= -\beta_{ext,\lambda} L_\lambda + \beta_{abs,\lambda} B_\lambda(T) + \frac{\beta_{sca,\lambda}}{4\pi} \int_{4\pi} P(\Omega', \Omega) L_\lambda(\Omega') \, d\Omega' \end{aligned} \tag{2.21}$$

Equations of radiative transfer have applications in a wide variety of subjects including optics, astrophysics, atmospheric science, and remote sensing. For the calculation of the radiative transfer in this work, the libRadtran framework is used [Emde et al., 2016, Mayer and Kylling, 2005].

2.2 Climate impact of aviation

2.2.1 CO_2 and non-CO_2 aviation impact

Global aviation operations contribute to anthropogenic climate change via a complex set of processes that lead to a net surface warming [Lee et al., 2021]. Aviation emissions of carbon dioxide (CO_2), and also a number of non-CO_2 climate forcing agents including nitrogen oxides (NO_x), water vapor, soot and sulfate aerosols, and increased cloudiness due to contrail formation are important. Aviation grew strongly over the past decades in terms of activity, with revenue passenger kilometers increasing from 109 to 8269 billion km yr^{-1} (1960–2018), and in terms of climate change impacts, with CO_2 emissions increasing by a factor of 6.8 to 1034 Tg CO_2 yr^{-1}. Over the period 2013–2018, the growth rates in both terms show a marked increase.

In the Fifth Assessment Report (AR5) of the Intergovernmental Panel on Climate Change (IPCC) published in 2011, these non-CO_2 agents caused 4% of the total global radiative forcing (RF) from all human activities. Persistent contrails and contrail cirrus, or together as aircraft-induced clouds (AIC), represent the largest aviation RF component - comparable to RF induced by natural variations of the solar incident energy - followed by aviation CO_2 emissions [Kärcher, 2018]. Within AIC, the long-lived contrail cirrus outbreaks account for 80% of the RF [Burkhardt and Kärcher, 2009].

Lee et al. [2021] present a new and comprehensive quantitative approach to evaluate aviation climate forcing terms. Both RF and effective radiative forcing (ERF) and their sums are calculated over the period 1940–2018 in Figure 1.2. RF is the instantaneous change in energy flux in the atmosphere caused by natural or anthropogenic climate change factors. As an alternative, ERF includes not only instantaneous forcing but also adjustments from the atmosphere and surface. Contrail cirrus yields the largest positive net (warming) ERF term followed by CO_2 and NO_x emissions. In addition, the formation and emission of sulfate aerosol contribute a negative (cooling) term. The mean contrail cirrus ERF/RF ratio of 0.42 indicates that contrail cirrus is less effective in surface warming compared to other terms. For 2018, the net aviation ERF is $+100.9\,\mathrm{mW\,m^{-2}}$ (5-95% likelihood range of (55, 145)), with major contributions from contrail cirrus ($57.4\,\mathrm{mW\,m^{-2}}$), CO_2 ($34.3\,\mathrm{mW\,m^{-2}}$), and NO_x ($17.5\,\mathrm{mW\,m^{-2}}$). Non-$CO_2$ terms sum to yield a net positive (warming) ERF that accounts for more than half (66%) of the aviation net ERF in 2018. The contribution normalized to aviation fuel use indicates that the contribution of global aviation is 3.5 (4.0, 3.4) % of the net anthropogenic ERF of 2290 (1130, 3330) $\mathrm{mW\,m^{-2}}$. Uncertainty distributions show that non-CO_2 forcing terms significantly contribute to the uncertainty in the aviation net ERF, with an approximate 8-fold impact compared to CO_2. The best estimates of the ERFs from aviation aerosol-cloud interactions for soot and sulfate remain undetermined. CO_2-warming-equivalent emissions based on the global warming potential method [Cain et al., 2019] indicate that aviation emissions are currently warming the climate at approximately three times the rate of that associated with aviation CO_2 emissions alone. CO_2 and NO_x aviation emissions and contrail cirrus radiative effects remain a continued focus of anthropogenic climate change research and policy discussions.

Recent global climate model simulations further discuss about the uncertainties in the estimation of contrail cirrus climate impact in Lee et al. [2021]. And the new released simulation results show reduced contrail RF. For example, higher atmospheric temperature and lower relative humidity (RHi) at the cruise level lead to the sublimation of contrails, which is not included in the previous model study. Bier and Burkhardt [2022] demonstrate the impact of parametrizing microphysical processes behind in the jet and vortex phase on contrail cirrus properties and RF. The contrail cirrus formation process will be described in the next Chapter. The effects of sublimation is included and the newly simulated ice crystal numbers agree well with in situ measurements over central Europe. The corresponding estimated global mean contrail cirrus RF for the year 2006 is 44 (31-49) $\mathrm{mW\,m^{-2}}$, around 22% lower than the numbers estimated in Bock and Burkhardt [2016b]. A recent independent approach using a physically based contrail cirrus prediction model with the humidity correction on a global scale calculates the annual mean contrail cirrus net RF of

64 mW m^{-2} in 2019, which is 44% lower than current best estimates for 2018 (111 mW m^{-2}) before COVID-19 [Teoh et al., 2023], in line with the decreasing trend shown in Bier and Burkhardt [2022].

2.2.2 Contrail cirrus formation and persistence

Contrail cirrus formation

Aircraft wake evolution is classified into four different regimes namely, the jet, vortex, dissipation and diffusion regimes [Gerz et al., 1998]. The schematic diagram of these regimes is shown in Figure 2.3 and 2.4 and explained in the following sections.

Figure 2.3 depicts the physical processes in the contrail formation stage.

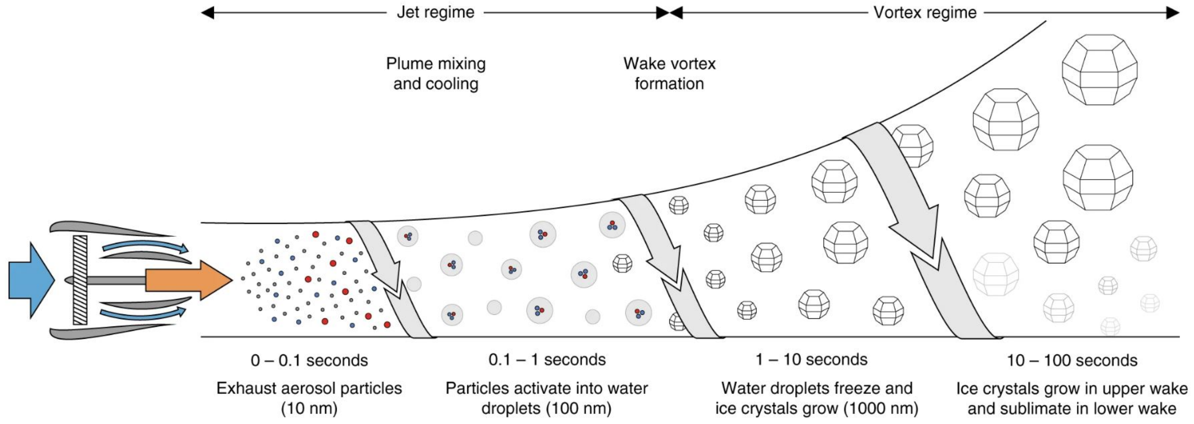
Jet regime
Vortex regime
Plume mixing and cooling
Wake vortex formation
0 – 0.1 seconds
Exhaust aerosol particles (10 nm)
0.1 – 1 seconds
Particles activate into water droplets (100 nm)
1 – 10 seconds
Water droplets freeze and ice crystals grow (1000 nm)
10 – 100 seconds
Ice crystals grow in upper wake and sublimate in lower wake

Figure 2.3: Processes influencing the contrail formation stage. The first stage is jet regime. Plumes, which comprise exhaust aerosol particles, expand from jet engines, activate into water droplets, and merge with vortices, forming an inhomogeneous wake. The further evolution of ice crystals depends largely on vortex regime. The downward motion of the vortex warms the air, which causes ice crystal sublimation in the lower part of the wake. Ice crystals present in the upper part of the wake continue to grow by uptake of ice supersaturated ambient water vapor. From Kärcher [2018].

After aircraft emission, the first development stages of contrails are **jet regime** in few seconds [Kleine et al., 2018]. In this regime, the contrail ice crystals nucleate and simultaneously, the vortices form and trap the freshly nucleated ice crystals in their cores. Ice crystals nucleate in contrails when the aircraft emitted hot and humid air mixes with the ambient cool air if saturation with respect to water is reached locally (so called contrail formation Schmidt-Appleman criterion, Appleman [1953], Schumann [1996]). Then droplets form by condensation of water vapor on emitted soot particles and entrained ambient aerosols and subsequently freeze [Bier et al., 2017, Kärcher et al., 2015, Kärcher and Voigt, 2017, Kärcher, 2018, Kleine et al., 2018]. The immediate freezing of the water droplets is essential to form persistent contrails because the upper troposphere is not saturated with respect to water but saturated with respect to ice [Verma and Burkhardt, 2022], which can allow ice crystals but not water droplets to persist. The number of nucleated ice crystals in a contrail is subject to the atmospheric state as well as aircraft and fuel parameters. In the case of contrail formation within natural cirrus, the surrounding ice crystals get absorbed into the combustion chamber and sublimate. Furthermore, natural ice crystals mix with the exhaust plume and sublimate as long as the plume is subsaturated. Contrails may also overlap, merge, and interact with natural cirrus [Duda et al., 2001, Sanz-Morère et al., 2021]. Contrail cirrus primarily differs from natural cirrus by their larger ice number concentrations (N) [Heymsfield et al., 2010b, Voigt et al., 2010, 2017]. Consequently, microphysical process rates, which control their life cycle and radiative effects can be very different to those in natural cirrus, and are dependent on soot number emissions [Bier et al., 2017].

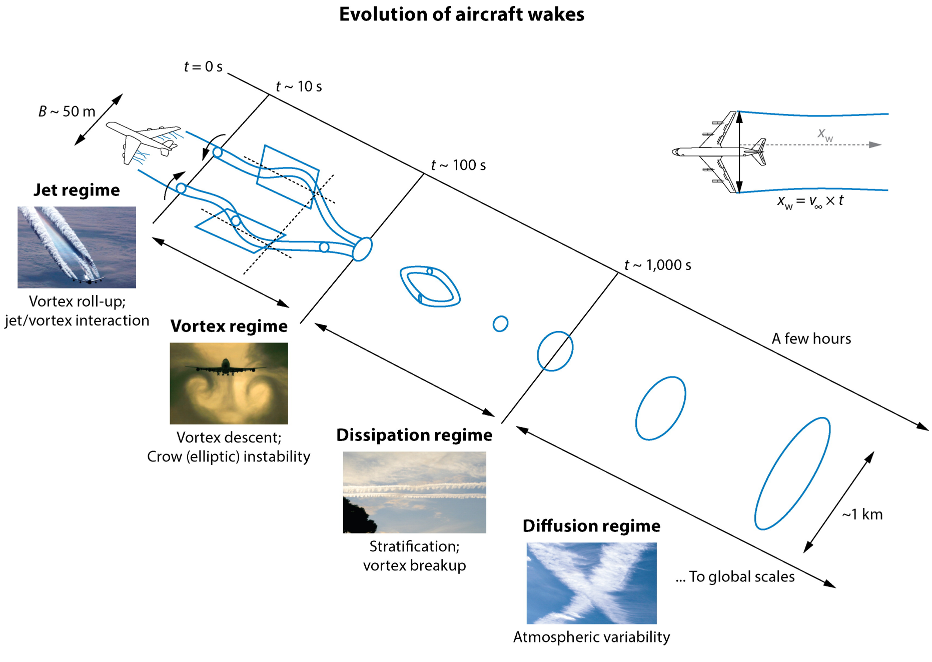
Evolution of aircraft wakes
t = 0 s
t ~ 10 s
t ~ 100 s
t ~ 1,000 s
A few hours
B ~ 50 m
x_w
$x_w = v_\infty \times t$
Jet regime
Vortex roll-up; jet/vortex interaction
Vortex regime
Vortex descent; Crow (elliptic) instability
Dissipation regime
Stratification; vortex breakup
Diffusion regime
Atmospheric variability
... To global scales
~1 km

Paoli R, Shariff K. 2016.
Annu. Rev. Fluid Mech. 48:393–427

Figure 2.4: Classification of aircraft wake evolution into four regimes. From Paoli and Shariff [2016].

Following the jet regime, the **vortex regime** starts, where the vortices propagate downward depending on atmospheric stability and aircraft properties. The density contrast between the air in the vortex and the surrounding air creates vorticity that is shed upwards, so called the secondary wake [Gerz et al., 1998]. The secondary wake stays close to the flight level. The primary wake often descends a few hundred meters [Kleine et al., 2018]. Many ice crystals within the primary wake sublimate due to adiabatic heating and the associated decrease in RHi, while the ice crystals in the secondary wake are more likely to survive [Unterstrasser, 2016]. Survival of the ice crystals in the vortex regime depends on atmospheric temperature, humidity, number of nucleated ice crystals and the maximum vertical displacement of the vortices. After the vortex descent, most of the air that was forced downwards rises again by the temperature difference, creating a vertically extended contrail. Recent global climate model simulations show that higher temperatures and lower relative humidities lead to significantly decreased ice crystal numbers during the vortex phase [Bier and Burkhardt, 2022]. Initial contrail ice crystal numbers per fuel mass are on average 50%–65% decreased relative to the soot number emission index in the extratropics and more in tropics. In the extratropics, this is mainly caused by a high ice crystal loss during the vortex phase and in the (sub)tropics and at lower flight levels by decreased ice nucleation.

In the **dissipation regime**, vortices collapse and release the ice crystals. The surviving ice crystals grow by uptake of the available water vapor if ambient air is ice supersaturated, causing an increase in the ice water content. The growth and the sizes of the ice crystals are dependent on the ambient RHi. In the case of contrail formation within cirrus, cirrus ice crystals and contrail ice crystals compete for the available water vapor. Not the aircraft dynamic controls the aircraft wake evolution but atmospheric variability controls the further mixing and diffusion of the contrail plume. The diffusion regime may last for a few hours [Paoli and Shariff, 2016]. Atmospheric turbulence plays an important role in the mixing, spreading and diffusion of the contrail plume. The vertical wind shear causes an increase in the further spreading of the contrail [Bock and Burkhardt, 2016a, Burkhardt and Kärcher, 2009, Jensen et al., 1998, Schumann et al., 1998, 2017].

Contrail cirrus persistence

The spreading stage makes contrail geometrically and optically thin. In saturated or subsaturated air, the contrail cover and optical depth decreases. Spreading in the highly supersaturated air causes the growth of contrail ice crystals and an increase of the contrail cover. During the **diffusion regime**, the ambient RHi also plays a critical role in developing young contrails. The contrail ice particles may sublimate or grow dependent on the atmospheric conditions, mainly ice supersaturation [Burkhardt and Kärcher, 2011, Bier et al., 2017, Schumann et al., 2017]. For example, contrail ice crystals persist and grow further if they spread in ice supersaturated air and sublimate if the air becomes subsaturated or ice crystals sediment into subsaturated air [Paoli and Shariff, 2016]. However, in the presence of natural cirrus ice crystals, the development of the contrail is affected because contrail ice crystals may not grow as large as they can grow in the absence of cirrus ice crystals since contrail and cirrus ice crystals compete for available water vapor. On the other hand, the development of cirrus is also affected due to the presence of contrail ice crystals which will lead to a change in sedimentation rate and ice water distribution in the cirrus [Tesche et al., 2016]. Natural cirrus locally optically thicken by embedded contrails [Tesche et al., 2016], and contrails can also cause a decrease in natural cloudiness [Verma and Burkhardt, 2022].

2.2.3 Contrail cirrus observations

Macrophysical and microphysical properties

To study cirrus clouds from space it is critical to distinguish the cirrus clouds from the surrounding cirrus-free areas i.e. to derive a cirrus cloud flag that classifies each observed scene as cirrus-free or cirrus-covered. The cloud top height (CTH) describes the distance between the Earth's surface and the top of the cirrus cloud. CTH is an important variable as it is closely related to the cloud top temperature and hence determines the outgoing thermal radiation.

As for microphysical properties, the ice optical thickness (IOT) stems from Eq. 2.16 and is defined as the vertically integrated attenuation of electromagnetic radiation due to scattering and absorption by cloud ice crystals within an atmospheric column ranging from the surface to the top of atmosphere.

The ice water content (IWC) (in $\mathrm{g\,m^{-3}}$) measures the mass of ice per unit volume of air

$$IWC = \int \rho_{ice} V(r) n(r)\,dr \tag{2.22}$$

where $\rho_{ice} = 917\,\mathrm{kg\,m^{-3}}$ is the mass density of ice and $V(r)$ and $n(r)$ are the mean volume and number of cloud ice crystals in the size distribution interval r to $r + dr$ of the particle maximum dimension per unit volume of air. Hence,

$$V_{ice} = \int V(r) n(r)\,dr \tag{2.23}$$

is the total volume of ice per unit volume of air (in $\mathrm{m^3 m^{-3}}$). IWC is, in contrast to IOT, a physical quantity, that can be directly used for comparisons with climate and weather models. The effective radius (R_{eff}, in m) describes the area weighted mean radius for an ensemble of cloud particles [Hansen and Travis, 1974]. For spherical cloud particles it is defined as the ratio

$$R_{eff} = \frac{\int r\pi r^2 n(r)\,dr}{\int \pi r^2 n(r)\,dr} \tag{2.24}$$

Several definitions of R_{eff} for an ensemble of non-spherical ice crystals have been presented in the literature [e.g., McFarquhar and Heymsfield, 1998] for an inter comparison. In this study the following definition is used

$$R_{eff} = \frac{3V_{ice}}{4A_{ice}} \tag{2.25}$$

where A_{ice} is the total projected area of ice per unit volume of air. The fraction 3/4 is introduced for consistency with Eq. 2.24 for spherical particles. Following Eqs. 2.22 and 2.23 the total volume of ice per unit volume of air can be expressed in terms of IWC

$$V_{ice} = \frac{IWC}{\rho_{ice}} \tag{2.26}$$

Similarly, the total projected area of ice per unit volume of air (in $\mathrm{m^2 m^{-3}}$) can be expressed in terms of the (volume) extinction coefficient β_{ext}

$$A_{ice} = \int A(r) n(r)\, dr = \int \frac{\sigma_{ext}(r)}{Q_{ext}} n(r)\, dr = \frac{\beta_{ext}}{Q_{ext}} \tag{2.27}$$

where $A(r)$ is the mean projected area of cloud ice crystals in the size interval r to $r + dr$ per unit volume of air and Q_{ext} is the (constant) extinction efficiency. Using Eqs. 2.26 and 2.27, Eq. 2.25 can be rewritten as

$$R_{eff} = \frac{3Q_{ext}IWC}{4\rho_{ice}\beta_{ext}} \tag{2.28}$$

Eq. 2.28 is used to estimate the R_{eff} of cloud ice crystals by Jensen et al. [2009], Hong and Liu [2015].

To study the macrophysical and microphysical properties of a contrail cirrus outbreak, in situ measurements and satellite remote sensing technique are used. In the past few years, various measurement campaigns have been performed to study differences between natural cirrus and contrail cirrus microphysical properties, e.g. International Cirrus Experiment (ICE) 1989 [Gayet et al., 1996], CONtrail and Cirrus ExpeRimenT (CONCERT) 2008 [Voigt et al., 2010], and ML-Cirrus 2014 [Voigt et al., 2017]. Schumann et al. [2017] give a comprehensive summary on contrail measurements from campaigns and from satellite over the individual contrail regimes. The ice crystal number concentration N in the few minutes old contrails is comparably 2 to 3 orders of magnitude higher than that in the surrounding cirrus cloud because of the different ice nucleation mechanisms in the contrail cirrus and natural cirrus clouds [Voigt et al., 2010, 2011, Bräuer et al., 2021]. The high soot emission from conventional kerosene fuel causes a high number concentration of ice crystals in the young contrails [Kleine et al., 2018]. The mean diameters of ice crystals in the few minutes old contrails are below 10 µm; on the other hand, the mean diameter of the aged natural cirrus ice crystals is comparably larger (100 µm) [Schröder et al., 2002, Schumann et al., 2017, Voigt et al., 2017]. Aged contrail cirrus can be difficult to distinguish from natural cirrus in terms of the number concentration as well as size of the ice crystals [Voigt et al., 2017].

From the fields of satellite observations, both natural cirrus and contrail cirrus are distinguishable on thermal infrared images, such as channels 10.8 µm and 12.0 µm of SEVIRI because of their relatively low brightness temperature with regard to other elements in the image. Due to smaller crystal sizes, especially young contrails [Gayet et al., 1996] tend to show higher transmissivity in channel 10.8 µm than in channel 12.0 µm compared to natural cirrus. By creating the brightness temperature difference (BTD) 10.8-12.0 µm, contrails are more easily detectable [Mannstein et al., 1999, 2010]. Contrails are also detected using their linear structures. Noteworthy are the attempts of Meinert et al. [1997] to train neural networks for contrail detection. The great number of samples and neurons needed and the very long training times made this method unavailable. In recent years there are some new promising attempts in this area such as Zhang et al. [2018]. For the ABI instrument [Advanced Baseline Imager; Schmit et al., 2015] aboard GOES-16 and GOES-17 Meijer et al.

[2022] have developed a contrail detection algorithm using convolutional neural networks. Following the cloud detection, the CTH, IOT and R_{eff} can also be retrieved from passive satellite imagers during both day and night using different methods mainly including CO2 slicing [Menzel et al., 2008], and visible and near infrared two channel retrieval [Nakajima and King, 1990].

Remote sensing of contrail radiative effects

Passive satellite sensors like the imaging radiometers SEVIRI [Schmetz et al., 2002], ABI, MODIS [Moderate Resolution Imaging Spectroradiometer; King et al., 1992] and AVHRR (Advanced Very High Resolution Radiometer) measure radiances of thermal radiation emitted by the Earth and reflected solar radiation leaving the Earth–atmosphere system at TOA. A passive imaging radiometer cannot resolve vertical cloud features and has a limited sensitivity to thin and sub-visual (visible optical thickness < 0.03) cirrus clouds, but typically it views an area large enough (by scanning or otherwise) to observe complete cloud systems.

Imaging radiometers measure the TOA radiances within given wavelength ranges, referred to as channels or spectral bands and are described by *spectral response functions* φ_λ that indicate the sensitivity of a channel to a given wavelength. Hence, the measured radiances in the thermal range cannot be described directly with Eq. 2.7, but are instead given by

$$L = \frac{\int \varphi_\lambda L_\lambda \, d\lambda}{\int \varphi_\lambda \, d\lambda} = \frac{\int \varphi_\lambda B_\lambda T_b \, d\lambda}{\int \varphi_\lambda \, d\lambda} \tag{2.29}$$

where φ_λ is the *spectral response function* of a given channel, B_λ is the spectral black body radiance and the (equivalent black body) brightness temperature T_b represents the temperature a black body would have in order to emit according to the spectral radiance L_λ of the observed grey body. For channels in the solar spectrum, the reflectance R can be calculated, describing the incident solar radiation reflected by the observed object

$$R = \frac{\pi \int \varphi_\lambda L_\lambda \, d\lambda}{\cos(\vartheta) \int \varphi_\lambda I_\lambda \, d\lambda} = \frac{\pi L}{\cos(\vartheta) I} \tag{2.30}$$

where I_λ is the spectral solar irradiance, I is the solar irradiance received by a given channel and ϑ is the solar zenith angle.

The solar radiation is partly reflected back to space by the Earth's surface and atmosphere as *reflected solar radiation (RSR)*, and is partly absorbed by the Earth-atmosphere system. The absorbed radiation is later re-emitted according to the Earth's and atmosphere's temperature and emissivity. Most of the emitted radiation is at longer wavelengths, referred to as *outgoing longwave radiation (OLR)* observed at TOA. Cloud ice crystals and water droplets absorb thermal radiation and emit it in all directions. The radiant energy emitted by a cloud out to space depends mainly on its top temperature. Less thermal radiation reaches TOA if the absorbing cloud is optically thicker, since a larger fraction of the thermal radiation is emitted back towards the Earth's surface. The stronger radiative contrast to (cirrus) cloud free scenes, so called longwave RF, is given by the low emission temperature of cloud top, not by the high emission temperature of cloud bottom. Shortwave RF is not mentioned here but can be inferred.

Atmospheric gases also absorb and emit thermal radiation, with water vapor, CO_2, CH_4 and O_3 being some of the most important absorbers of thermal radiation in the atmosphere. The absorption by the single molecules strongly depends on wavelength. The thermal radiation at TOA, reaching a passive imaging radiometer, thus consists of the radiation directly transmitted from the Earth's surface and the radiation absorbed and emitted out to space by clouds, aerosols and atmospheric gases. Hence, different cirrus clouds leave their unique mark on the TOA radiances observed by an imaging radiometer, depending primarily on the cirrus cloud temperature (height) and optical properties, but also on the presence and properties of underlying liquid water clouds, aerosols, atmospheric gas concentrations and the Earth's surface properties (temperature, emissivity), which regulate the thermal radiation emitted by the Earth.

The instantaneous net RF at TOA is the change of the total irradiation under a situation with cirrus minus the irradiances in the same situation without cirrus. In fact, the SW component of the cirrus RF $RF_{SW_{TOA}}$ can be diagnosed as

$$RF_{SW_{TOA}} = SW_{\uparrow no\,cirrus} - SW_{\uparrow cirrus} \tag{2.31}$$

Notice that $SW_{\uparrow cirrus}$ corresponds to the RSR that can be observed by the satellite. Similarly, the LW RF $RF_{LW_{TOA}}$ can be diagnosed from

$$RF_{LW_{TOA}} = LW_{\uparrow no\,cirrus} - LW_{\uparrow cirrus} \tag{2.32}$$

Again, the cirrus term $LW_{\uparrow cirrus}$ in Eq. 2.32 corresponds to the OLR that can be computed from satellite observations. The net cirrus RF $RF_{NET_{TOA}}$ is defined as

$$RF_{NET_{TOA}} = RF_{SW_{TOA}} + RF_{LW_{TOA}} \tag{2.33}$$

Despite the attention and numerous studies on RF and other properties of contrail and contrail cirrus in the past decades [Mannstein et al., 1999, Minnis et al., 2004, Palikonda et al., 2005, Atlas et al., 2006, Burkhardt and Kärcher, 2011, Iwabuchi et al., 2012, Duda et al., 2013, Schumann et al., 2021a], the level of understanding of this particular aspect of aviation is still classified as low, and the estimation of emitted soot aerosols and cloud interactions is determined as very low [Lee et al., 2021]. Although the global contrail cirrus RF value may seem small, the local effect is larger in regions with high contrail coverage. The contrail cirrus RF increases in the main air traffic corridors over Europe and the US [Bier and Burkhardt, 2022, Teoh et al., 2023] and contributes significantly to the anthropogenic RF in these regions. The difficulty in distinguishing natural cirrus clouds from AIC is one of the roots of large uncertainties in contrail RF [Mannstein and Schumann, 2005]. Vázquez-Navarro et al. [2015] used a contrail detection algorithm [CDA, Mannstein et al., 1999] and an automatic contrail tracking algorithm [ACTA, Vazquez-Navarro et al., 2010] to locate and track the development of contrails. RRUMS [Rapid

Retrieval of Upwelling irradiance from MSG/SEVIRI; Vázquez-Navarro et al., 2013] and COCS [Cirrus Optical properties derived from CALIOP and SEVIRI; Kox et al., 2014] are additionally used to retrieve contrail RF, energy forcing, optical thickness and CTH in Vázquez-Navarro et al. [2015]. In fact, not many studies have focused on the observation of the contrail-to-contrail cirrus evolution.

Airborne measurements can provide detailed in situ data sets and lidar profiling, and geostationary satellite observations are capable of capturing the large spatial scale and high temporal resolution of contrail cirrus evolution. Thus it would also be a good option to combine knowledge from in situ measurements and satellite observations to identify the differences between natural cirrus and contrail cirrus and to study the diurnal cycle of the contrail cirrus outbreak. This study will be shown in Chapter 4.

2.3 Ice supersaturated regions

2.3.1 Physical definitions

Ice supersaturation is an important atmospheric condition for the formation of cirrus clouds and in particular for the persistence of cirrus and contrail ice crystals [Burkhardt and Kärcher, 2011, Gierens and Brinkop, 2012, Heymsfield et al., 2010a]. Therefore, it is essential to understand ice supersaturation conditions and their probability of occurrence in high altitudes. Ice supersaturated regions are formed when water vapor exceeds its saturation vapor pressure value, e.g. due to an ascending motion of air leading to adiabatic cooling or injection of water vapor into the air. Ice saturation vapor pressure is the thermodynamic equilibrium state between water vapor and ice (also called saturation vapor pressure with respect to ice) [Pruppacher and Klett, 2010]. The saturation vapor pressure over ice increases nonlinearly with increasing temperature according to the Clausius-Clapeyron equation. However, the atmosphere is not always in thermodynamic equilibrium state, the concentration of water vapor can exceed its saturation vapor pressure and that is called supersaturation with respect to ice. Often, it is seen that upper tropospheric air is supersaturated with respect to ice and subsaturated with respect to water because the saturation vapor pressure over ice is smaller than the saturation vapor pressure over water. The ice saturation ratio, or in another word, RHi, is defined as $\frac{P_{H2O}}{P^*_{H2O}}$, where P_{H2O} is the partial vapor pressure of water vapor and P^*_{H2O} is the saturation vapor pressure with respect to ice. Ice supersaturation corresponds to RHi $> 100\%$.

The upper tropospheric air can stay ice supersaturated in the absence of ice crystals or ice nuclei; otherwise, processes, i.e. ice nucleation in the presence of suitable ice nuclei and deposition of available water vapor on already existing ice crystals, take place to bring back the air to the equilibrium state of saturation. However, nucleation of ice crystals is a complicated process that does not start immediately once saturation with respect to ice is reached because nucleation of ice crystals needs significantly high ice supersaturation depending on the nucleation pathway [Gettelman et al., 2010]. Therefore, the ice supersaturation condition is called a metastable state in contrast to the unstable state. In an unstable state, processes, e.g. condensation, evaporation and sublimation, start immediately to revert back to the equilibrium state. In-cloud subsaturation, where the partial vapor pressure is smaller than the saturation vapor pressure, is unstable because this state induces the evaporation of water droplets or sublimation of ice crystals immediately.

2.3.2 Ice supersaturated regions observations

Regular in situ measurements of water vapor started in the late 1990s in Europe under the Measurement of Ozone and Water Vapor by Airbus In-Service Aircraft (MOZAIC) and the successor In-Service Aircraft for Global Observing System (IAGOS) programs, in which atmospheric water vapor was regularly measured from research quality hygrometers installed on commercial aircraft. The MOZAIC and IAGOS database showed that ISSRs often occur in the UTLS [Gierens and Spichtinger, 2000]. The vertical thickness of ice supersaturated layers is on average shallower than 500 m, but in very rare situations the ice supersaturated layers can be thicker, up to 3000 m [Dickson et al., 2010]. The horizontal extension of ISSRs is difficult to estimate. However, Gierens and Spichtinger [2000] estimated the mean path length of ice supersaturated layers to be 150 km long with a standard deviation of 250 km. ISSRs may contain optically thin cirrus clouds, with small ice surface areas that cannot deplete to ambient humidity to reach ice saturation. Also atmospheric temperature variations strongly influence ISSRs leading to warming or cooling processes.

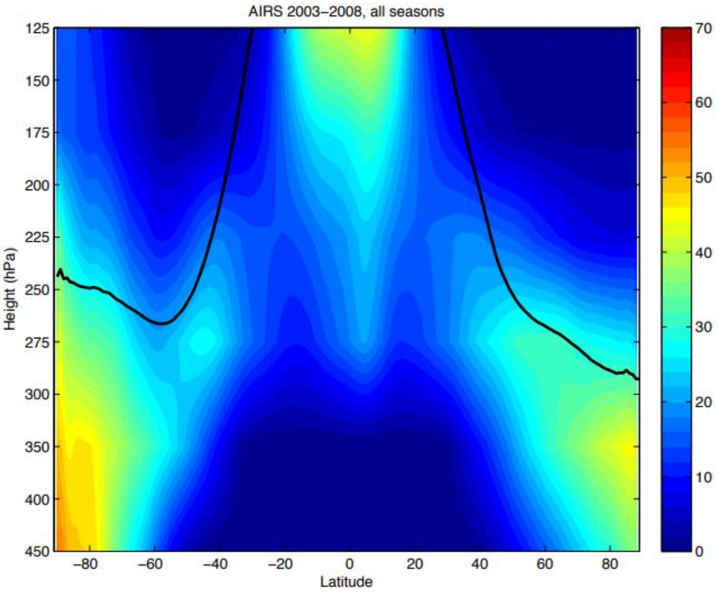

Figure 2.5: Zonal means of ice supersaturation occurrence frequencies (%) from the Atmospheric InfRared Sounder (AIRS) using RHi > 100%. Plain line: zonal-mean tropopause (all seasons). Only good quality data used for 7 year statistics in 2003–2009. From Lamquin et al. [2012].

ISSRs were further observed in different ways, including radiosondes, airborne measurement campaigns and satellite observations, showing the existence of ISSRs. The global distribution of ISSRs can be obtained from satellite data. Lamquin et al. [2012] provided a complete picture of the distribution of ISSRs globally and in the vertical dimension (see Figure 2.5). For the analysis, the water vapor was observed from AIRS on NASA polar orbiting AQUA satellite and calibrated using MOZAIC data. The measurements reveal that a high frequency of ISSRs in the tropics at around 150 hPa pressure level within the tropical tropopause layer (TTL). Ice supersaturation occurs at lower altitudes (increase in pressure) in the extratropics. Ice supersaturation frequency is most significant in the UT and decreases strongly in the stratosphere, due to water vapor and temperature gradients. Since the tropopause slopes downwards when moving towards the poles, high frequencies of ice supersaturation above 200 hPa are confined to the tropics. ISSRs in the atmospheric pressure layer between 200 hPa to 250 hPa are found along the storm tracks in the midlatitudes, and below 250 hPa, ISSRs are located in the polar regions.

2.3.3 Ice supersaturated regions parameterizations in NWP

A state of ice supersaturation is observed quite often in the UT, both in clear air [e.g., Petzold et al., 2020] and within cirrus clouds [Dekoutsidis et al., 2023, Ovarlez et al., 2002, Spichtinger et al., 2004]. Although this state has been first reported at the beginning of the last century, it was ignored in numerical weather prediction (NWP) until the end of the 20th century, when it was first introduced into the U.K. Meteorological Office Unified Model [Wilson and Ballard, 1999] and later into the integrated forecast system (IFS) of ECMWF [Tompkins et al., 2007]. However, NWP models that incorporate ice supersaturation in their cirrus parameterizations, often assume (at least, one-moment parameterizations with cloud fraction) that supersaturation relaxes to saturation in the cloudy part of a grid box as soon as cloud formation occurs. Hence, this procedure that is termed *saturation adjustment* [McDonald, 1963], ignores ice supersaturation within cirrus clouds. Subsequently, it leads to underestimation of the occurrence frequency and the degree of ice supersaturation in upper-tropospheric layers [Gierens et al., 2020] and this turns out to be a problem for the forecasting of persistent contrails, which form and persist in ice supersaturated air.

Reutter et al. [2020] use IAGOS in situ water vapor measurements over the North Atlantic Region to validate 10-year ERA-Interim reanalysis (see Figure 2.6). The agreement of ISSRs between reanalysis and measurements is decreasing with increasing height, and an underestimation of ISSRs from ERA-Interim is exhibited. One reason might be the data assimilation of measurements into the reanalysis data set. The operational radiosondes using capacity sensors show large deviations for temperatures below -40 °C or very low absolute humidity [Spichtinger et al., 2003]. Therefore, the response time is increasing in the UT to the tropopause layer due to the decreasing temperature. Further up in the stratosphere, temperatures are increasing again. However, the absolute humidity is decreasing with height, leading to an increased response time.

Sperber and Gierens [2023] concluded two reasons for underestimation of supersaturation in the current NWP parameterisations with saturation adjustment including decrease of supersaturation right at cloud initiation and ignorance of the equilibrium supersaturation later. Thus, the in-cloud humidity as a new prognostic variable is introduced and the humidity distribution in newly generated cloud parts from a stochastic box model is derived. The new ice cloud scheme overcomes saturation adjustment by explicitly modelling the decay of the in-cloud humidity after nucleation and even in aged cirrus if temperature keeps decreasing, thereby allowing for both in-cloud super and subsaturation.

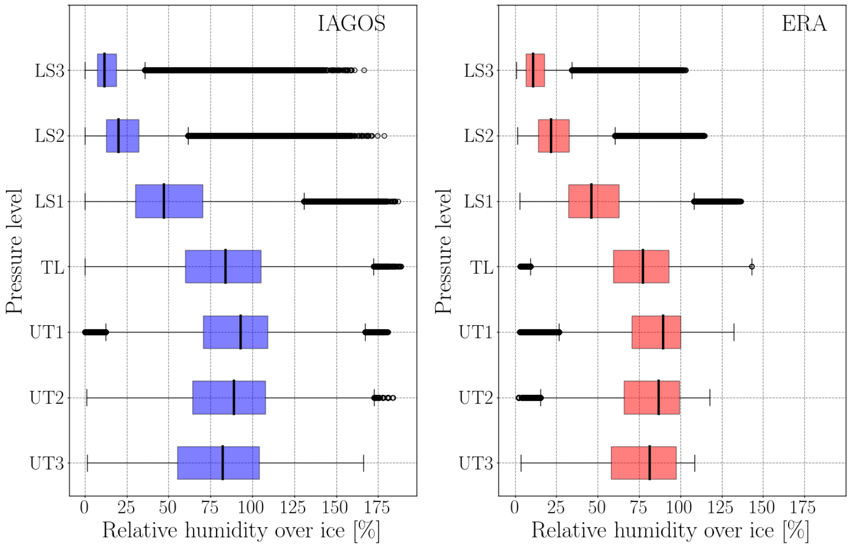

Figure 2.6: Vertical profiles of RHi (%) for IAGOS (blue) and ERA (red) during 1 January 2000 to 31 December 2009 over the NAR. Figure from Reutter et al. [2020].

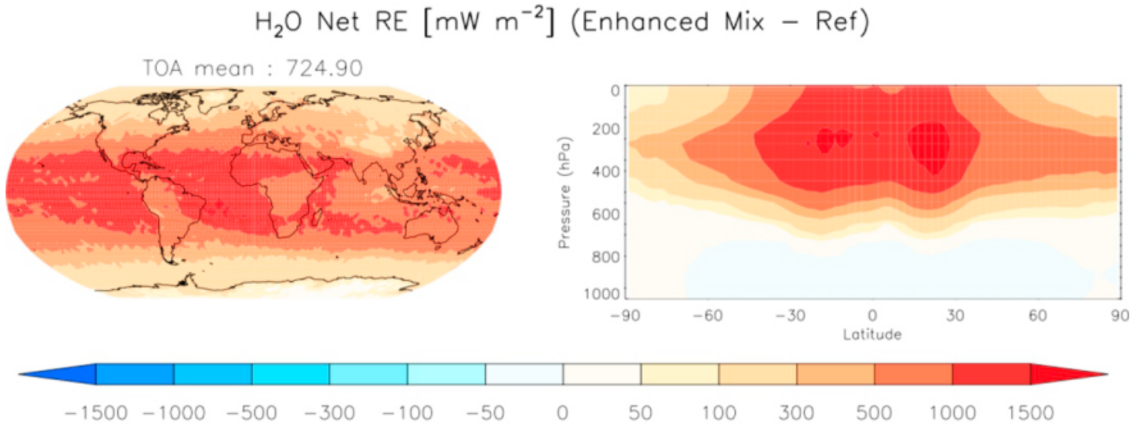
H$_2$O Net RE [mW m^{-2}] (Enhanced Mix – Ref)
TOA mean : 724.90
0
200
400
600
800
1000
Pressure (hPa)
−90
−60
−30
0
30
60
90
Latitude
−1500
−1000
−500
−300
−100
−50
0
50
100
300
500
1000
1500

Figure 2.7: Radiative effects of the enhanced mixing simulation (compared to the reference simulation) for water vapor (left) at the TOA and (right) zonally averaged. The numerical values in the left panel are TOA annual global means for 2003. From Riese et al. [2012].

To determine the sensitivity of water vapor radiative effects to the uncertainties of water vapor amount and distribution, Riese et al. [2012] made two simulations that only differ in the value of the atmospheric mixing parameter λ_C (critical Lyapunov exponent), a reference simulation with a value of $\lambda_C = 1.5$ day^{-1} and an enhanced mixing simulation with a value of $\lambda_C = 1.2$ day^{-1}. As a result of enhanced mixing, an increase of water vapor concentrations in the extra-tropical lowermost stratosphere (LMS) of 10 to 15% is found. This increase can mainly be attributed to differences in the transport of air masses from the upper tropical troposphere into the extra-tropical LMS. Figure 2.7 illustrates that the radiative effects of water vapor with steep gradients in the UTLS are very sensitive to uncertainties in the water vapor concentrations. For water vapor, the largest increase of radiative effect is found at equatorial latitudes with values reaching about 1.5 Wm^{-2}. The globally averaged effect from the change of water vapor at TOA is 0.72 Wm^{-2}.

2.3.4 Influential meteorological conditions

The physical processes behind the formation of ice supersaturation are illustrated here, as their careful treatment is the prerequisite of a realistic description of the ice supersaturation in the UTLS region inside NWP models [Reutter et al., 2020].

Large scale ISSRs often form when water vapor is carried to upper altitudes through a large-scale rising motion of the air and the accompanying adiabatic cooling; this increases the saturation ratio with respect to ice [Gierens and Brinkop, 2012]. Water is transported into the upper troposphere also through high reaching convective events in the tropics. Gravity waves connected with convection and the slowly rising air in the TTL are responsible for the formation of ISSRs in high altitudes. In the extratropics, water vapor reaches the upper troposphere often through vertical transport connected with the synoptic-scale baroclinic instability where optically thick natural cirrus are often observed [Carlson, 1993]. These ISSRs are suitable for persistent contrails. Then contrail cirrus outbreaks are often seen in these regions when air-traffic density is high [Bier et al., 2017, Carleton et al., 2008]. ISSRs are found along the storm track zones where extratropical cyclones form in mid-latitudes. Also, ISSRs are formed in anti-cyclonic flow patterns.

ISSRs can form in cloud-free air as well as within cirrus clouds. High ice supersaturation, below the homogeneous freezing threshold, can exist in the cirrus if the ice crystal number concentration is low [Dekoutsidis et al., 2023]. Ice supersaturation within cirrus decreases with an increase of the ice number concentration and the ice crystal radius [Korolev and Mazin, 2003]. Cirrus with low ice number concentration consumes available water vapor slowly. Therefore, high ice supersaturation can exist for an extended period of time, specifically in cold cirrus below a temperature of 205 K, since at this temperature, diffusion of water vapor is relatively slow [Krämer et al., 2009]. Recent measurements by Li et al. [2023b] suggest that a significant fraction of clouds may also be subsaturated with respect to ice.

Small scale dynamics and turbulence influence the water vapor and RHi distribution in clouds or contrails [Kaufmann et al., 2016, 2018, Li et al., 2023b]. It is not possible to forecast ISSRs using dynamical states alone [Gierens and Brinkop, 2012], even with the combination of dynamical fields including divergence, relative vorticity, and vertical velocity. The history of an air parcel especially in thermodynamic states for example humidity and temperature has to be known as well.

2.4 Artificial neural networks

Artificial neural networks (ANN) are a branch of machine learning models. An ANN consists of a number of neurons that exchange information with each other, in a similar manner as biological neural networks in human brains. By assigning each neuron-neuron connection a tunable weight, the ANN has the ability to learn patterns and approximate functions. The goal of an ANN is to derive a vector of unknown output variables according to a vector of known input data. ANNs can be used for classification as well as function approximation. ANNs are applied in a variety of fields, and used frequently in the context of atmospheric sciences [Gardner and Dorling, 1998, Hsieh and Tang, 1998], Earth system sciences [Reichstein et al., 2019] and remote sensing [Mayer et al., 2023, Piontek et al., 2021b,a, Strandgren et al., 2017a]. This tool is applied in Chapter 5 to the novel prediction of humidity and is thus introduced in the following.

2.4.1 Multilayer perceptron

In this study a multilayer perceptron (MLP), a feed-forward ANN, is used. An MLP consists of at least three layers; (1) one input layer, (2) one output layer and (3) one or more *hidden* layers. The input layer holds as many neurons as input data and the output layer as many neurons as desired output quantities. The hidden layer(s) hold an arbitrary number of additional neurons distributed over an arbitrary number of hidden layers. Neurons receive the weighted sum of the results of the previous layer's neurons and use it as the argument of an *activation function*; the result is forwarded to the following layer (see Figure 2.8). All connections between the neurons within the MLP are in the forward direction. Linear functions might be applied by single neurons (e.g., in the output layer for the approximation of a continuous function). The non-linear activation functions allow the ANN to solve complex problems with a limited number of neurons. The rectifier or the rectified linear unit (ReLU) activation function [Agarap, 2018], the most widely used non-linear activation function, is give as

$$
\begin{aligned}
f(x) &= x^{+} \\
&= max(0, x) \\
&= \frac{x + |x|}{2} \\
&= \begin{cases} x & if\ x > 0 \\ 0 & otherwise \end{cases}
\end{aligned}
\tag{2.34}
$$

This function shows a high computational efficiency and is exploited in the input and hidden layers for building the humidity prediction model in Chapter 5.

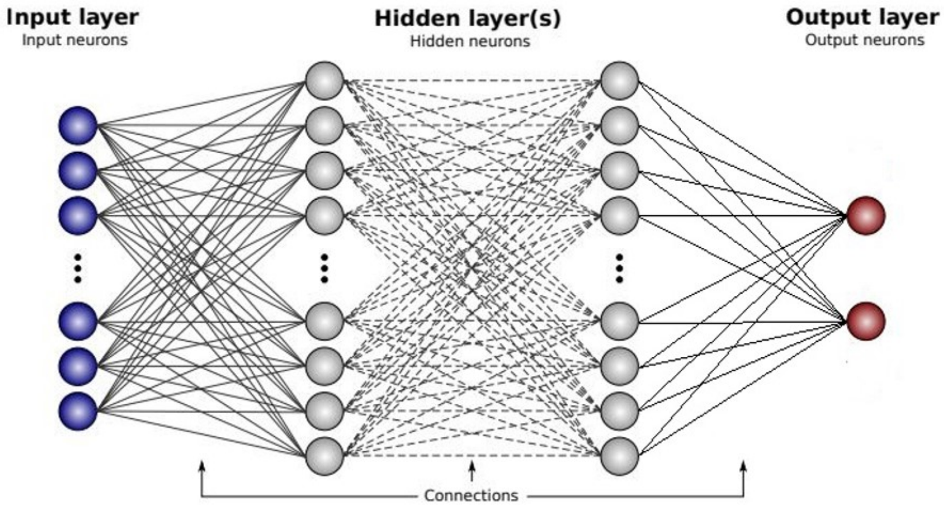

Figure 2.8: The structure of a multilayer perceptron (MLP) with a form of a feed-forward artificial neural network (ANN) used in this study. Figure updated from Strandgren et al. [2017a].

2.4.2 Training

The use of non-linear activation functions recommends the transformation of the original data for the normalization of the input. That is, for a data set with multiple inputs, it generally has different scales for each of the features. The same considerations can be made for data sets with multiple targets. This situation could give rise to greater influence in the final results for some of the inputs, with an imbalance not due to the intrinsic nature of the data but simply to their original measurement scales. Normalizing all features in the same range avoids this type of problem. Another reason for input normalization is related to the gradient problem which will be introduced in the next paragraphs. The re-scaling of the input within small ranges gives rise to even small weight values in general, and this makes the output of the units of the network near the saturation regions of the activation functions less likely. Furthermore, it allows to set the initial range of variability of the weights in very narrow intervals, typically [-1:1].

The central step in the creation of an ANN is the iterative training. After setting up the ANN's architecture, the weights are randomly initialized. Then one uses a training data set consisting of samples of input data and the corresponding true output values for *supervised learning*. The ANN is applied to the input data and the resulting outputs are compared to the target output to calculate the difference in form of a *loss function* E. All weights are now modified in order to reduce the loss function. The resulting ANN is again applied to the training input data and this procedure is repeated until the loss function is sufficiently small, i.e, a point close to the global minimum is reached [Gardner and Dorling, 1998]. In practice, this procedure is complicated, and can be trapped in local minima, at saddle points, on plateaus, or distracted by exploding gradients. The loss function E can be an arbitrary error function, e.g., the *mean squared error*. A gradient descent algorithm is applied to adjust all weights such that the loss function is reduced.

$$\omega_t = \omega_{t-1} - \eta \frac{\delta E}{\delta \omega_{t-1}} \tag{2.35}$$

where ω_t and ω_{t-1} are the old and new values for a weight connecting the two neurons. $\eta \frac{\delta E}{\delta \omega_{t-1}}$ describes how much a change in ω_{t-1} affects the total error. To adjust how aggressive the weight updates should be, a *learning rate* η is multiplied with $\frac{\delta E}{\delta \omega_{t-1}}$ before the weight update. A larger learning rate means larger changes in the weights and thus a faster training. However, it may prohibit convergence of the loss function. With a small learning rate, the total error will not oscillate around a minimum solution, but the training is slow and the risk of getting stuck in local minima is higher. The training speed can also be increased by using more elaborate updating rules. *Momentum* denotes a weighted sum of the current and previous error gradients. By adding the *momentum* to the last update of ω_{t-1}, possible oscillations in the iterative search for the minimum error are reduced and a larger learning rate can be considered.

To find the minimum total error between the estimated and expected output vectors for a complex problem and tune the weights accordingly, a large training data set is required. Training a MLP is an iterative process, where each training example is transmitted to the ANN multiple times until a satisfying result has been achieved. In a common ANN, after one *epoch* when all examples contained in the training data set have been transmitted to the ANN, the training completes and the weights are updated every time in one *iteration*. The amount of iterations required for one epoch therefore depends on the amount of training examples the ANN is given for every update of the weights, i.e. the batch size. With mini-batch gradient descent an intermediate number of training examples is used for each weight update ($1 <$ batch size $<$ N, where N is the total number of training examples).

A common phenomenon during training is the occurrence of overfitting, i.e. the ANN starts to learn the inherent noise of the training data set and, as a result, performs worse for new samples. Thus, the available data is usually split into a training, a validation and a test data set. The training data is used for the adjustment of the ANN, whereas the validation data set is regularly evaluated during the training. After an initial phase of decreasing loss functions for both training and validation data, overfitting might lead to a further decay of training loss with a simultaneous increase in validation loss. Early stopping describes a strategy to stop training as soon as this point is reached. However, as the loss function is usually not monotonically decreasing but might exhibit numerous local minima, the definition of a stopping criterion is not straightforward. Since the validation data set is now part of this extended training algorithm, the final performance of the ANN is evaluated on the independent test data set.

2.4.3 Model interpretation

Interpretation of the trained ANNs is commonly the quantification of the importance of single weights. First, the absolute value of a weight can be assumed to relate to its relevance for the model. Second, the impact on the loss function can be considered when removing a weight, which corresponds to setting a weight to zero. Third, the change of the loss function can be investigated when slightly varying the weight. In principle, these methods can also be used to investigate the importance of individual input features of an ANN. For example, Strandgren et al. [2017b], Piontek et al. [2021a] evaluated the weights connected to an input neuron to deduce its relevance, whereas Li et al. [2022, 2023a] applied the pruning method to find the relative importance and marginal contributions of multiple factors to observed global trends. These methods have also been applied for pruning, i.e. the significance of the weights of a large, trained ANN is calculated and the least important connections are removed to obtain a smaller structure with similar performance. Alternatively, complete neurons can be removed based on the impact of their presence on the loss function [Bishop., 1995]. ANN will be used in Chapter 5 to improve the humidity forecast.

Chapter 3

Instrumentation, data and methods

The text in Sects. 3.1, 3.2.1, and 3.4 in this chapter have been published in Wang et al. [2023].

In this chapter the remote sensing and airborne instruments, data, and methods or models developed by other used to investigate the microphysical properties and radiative effects of the contrail cirrus outbreak (Chapter 4) and to improve the relative humidity prediction for the contrail cirrus climate impact assessment (Chapter 5 and 6) are introduced.

3.1 Satellite remote sensing from MSG/SEVIRI

SEVIRI is a passive imaging radiometer operating aboard the geostationary Meteosat Second Generation MSG satellites since 2004. SEVIRI is the main source of input data for CiPS and RRUMS for the investigation in Chapter 4.

The MSG spacecraft is spinning around an axis in north-south direction, thereby measuring radiation coming from the Earth along lines in the east-west direction. SEVIRI measures the up-welling radiation within 12 channels. Three bands are in the visible and near-infrared spectrum and are centered at 0.6 µm, 0.8 µm and 1.6 µm. Eight bands are in the thermal infrared and are centered at 3.9 µm, 6.2 µm, 7.3 µm, 8.7 µm, 9.7 µm, 10.8 µm, 12 µm and 13.4 µm. One channel is a high resolution visible (HRV) broadband, covering roughly 0.4 to 1.1 µm and half of the SEVIRI disk at each revolution. The operational MSG satellite is positioned ca. 35800 km above the Earth's Equator at 0°E giving SEVIRI an excellent view of the Earth from its remote location, with a spatial coverage from approx. 80°W to 80°E and 80° S to 80° N. As shown in Figure 3.1, the HRV channel has a limited coverage and includes the European and most of the African continent. The spatial sampling of SEVIRI is $3\times3\,\text{km}^2$ at nadir ($1\times1\,\text{km}^2$ for the HRV channel) which increases to approx. $3.5\times5\,\text{km}^2$ on average over Europe [Schmetz et al., 2002]. The MSG satellites provide observations of the Earth disk every 15 min, and the temporal resolution can be increased to 5 min using the rapid-scan mode.

Four MSG satellites have been launched, named Meteosat-8 to -11 or alternatively

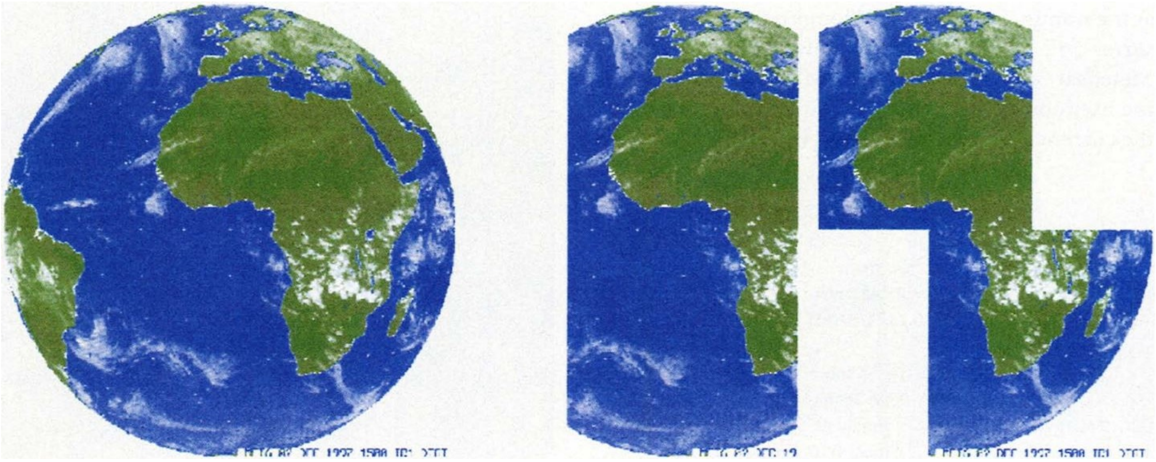

Figure 3.1: Left: coverage with SEVIRI on MSG, in its nominal position at 0° lon, for a repeat cycle of 15 min for channels except from the HRV. The full disk image has 3712×3712 pixels. Right: the HRV covers only half of the earth in the E-W direction with 11136×5568 pixels; however, the area of imaging can be selected. Figure adapted from Schmetz et al. [2002].

MSG1 to 4. The current main operational satellite MSG4 is located at 0°E with a backup MSG2 at 3.5°E. MSG3 operates at 9.5°E in rapid-scan mode, covering only the upper third of the SEVIRI disk (including Northern Africa and Europe). MSG1 was moved to 41.5°E to cover the Indian Ocean. MSG-3/4 / Meteosat-10/11 observations are used for this study.

3.1.1 CiPS

CiPS (Cirrus Properties from SEVIRI) detects cirrus with their transparency information and retrieves the corresponding CTH, IOT, and ice water path [Strandgren et al., 2017a]. It consists of four ANNs trained using SEVIRI thermal observations, CALIPSO (Cloud-Aerosol Lidar and Infrared Pathfinder Satellite Observations) cloud products, and ECMWF ERA5 surface temperature and auxiliary data. CiPS has been especially developed for thin cirrus and validated against CALIPSO. CiPS detects 20%, 70% and 85% of the ice clouds with an IOT of 0.01, 0.1 and 0.2 respectively. For IOT between 0.35 and 1.8 CiPS has a mean absolute deviation smaller than 50%. This value increases for IOT between 0.07 and 0.35. For CTHs larger than approx. 8 km, CTH has an absolute percentage error of 10%, with underestimation for CTH $>$ 10 km at 50°N and overestimation for CTH $<$ 10 km at the same latitude. An example is shown in Figure 4.1.

3.1.2 GERB and RRUMS

The GERB (Geostationary Earth Radiation Budget) instrument measures broadband solar and thermal components which are subsequently converted to outgoing and reflected fluxes considering the cloud properties and surface type detected by SEVIRI [Harries et al., 2005]. GERB's sampling distance is larger than that of SEVIRI with a spatial resolution of 44.6 km×39.3 km but the same image repeat cycle of 15 min. During the processing, the finer spatial resolution of the SEVIRI data is used to improve the original GERB resolution and results in GERB products for 3×3 SEVIRI pixels. In general, the GERB SW and LW fluxes are found to be 7.5% higher and 1.3% lower respectively, compared to products from the Clouds and the Earth's Radiant Energy System (CERES), whose data records are from polar orbiting satellites [Wielicki et al., 1996]. The bias of CERES is estimated to be 1% and 0.5% for OLR and RSR, respectively.

Based on a linear regression and a neural network, an algorithm named RRUMS (Rapid Retrieval of Upwelling Irradiances from MSG/SEVIRI) was also developed, which estimates OLR and RSR at TOA from SEVIRI at pixel level. RRUMS shows excellent agreement with OLR from CERES within 1% and a systematic overestimation of RSR from CERES or GERB of 5% to 10% in the worst cases under high viewing angles [Vázquez-Navarro et al., 2013].

3.2 Airborne measurements

3.2.1 In situ and lidar instruments aboard HALO

The in situ cirrus measurements used in this study have been performed by Tina Jurkat-Witschas, the RHi data were evaluated by Stefan Kaufmann, the NO_y data by Helmut Ziereis and the lidar data were measured by Silke Groß and Martin Wirth.

During ML-CIRRUS, the German research aircraft HALO was equipped with a comprehensive suite of novel particle measurement sondes, and obtained a broad data set of microphysical properties of contrail cirrus and natural cirrus for process studies and climatological analyses. Ice number concentrations N, R_{eff}, size distributions, IWC or liquid water content (LWC) and extinction are derived from measurements of CAS-DPOL (Cloud and Aerosol Spectrometer with Detector for Polarization) for particles from 3 to 50 µm and CIP (Cloud Imaging Probe) for the size range of 15 to 960 µm (diameter as the maximum dimension). CAS-DPOL measures the forward scattered light of particles when they pass through a laser beam [Baumgardner et al., 2011]. The uncertainty of the particle size measurements is ±16% [Kleine et al., 2018] for the lower size range and can be up to ±50% for R_{eff}, if the shape of the particles is not known. This translates into an error of up to ±100% for the IWC derived from scattering cloud probes [Baumgardner et al., 2017]. Using 64-element linear photodiode arrays, the CIP acquires two-dimensional shadow images of particles [de Reus et al., 2009]. The size resolution is 15 µm with the uncertainty decreasing considerably with diameter, reaching ±15 µm when particles are larger than 50 µm. N from CAS-DPOL, denoted by N_{CAS} in the following, and from CIP (N_{CIP}) are also combined to an overall N between 10^{-4} and $10^{2}\,\mathrm{cm}^{-3}$. Validation of the measurements has been performed taking atmospheric and cloud chamber measurements into account [Braga et al., 2017a,b].

As for ambient conditions, the AIMS (Atmospheric Ionization Mass Spectrometer, Jurkat et al. 2011, Kaufmann et al. 2016) was applied to measure water vapor concentration in ambient air using a backward heated inlet. The range of detection is between 1 and 500 ppm with an overall accuracy from 7% to 10%. Static pressure and temperature, measured by the BAHAMAS (Basis HALO Measurement and Sensor System, Krautstrunk and Giez 2012) with an accuracy of 0.3 hPa and 0.5 K, were used to convert water vapor concentration to RHi with an uncertainty of 10% to 20% [Kaufmann et al., 2018]. During the mission, NO and the sum of all reactive nitrogen species (NO_y) were measured using the AENEAS (AtmosphEric Nitrogen oxides mEAsuring System) instrument. This dual channel instrument is based on the well-established chemiluminescence technique combined with catalytic conversion of the NO_y components. It has been regularly operated on HALO during several missions (e.g., Ziereis et al. 2022). A detector identical in construction has also been operated on a commercial aircraft as part of IAGOS-CARIBIC [Stratmann et al., 2016]. The statistical detection limit is about 7 pmol/mol for NO. The overall uncertainty depends on the ambient concentration of NO and ranges from about 8 to 6% for volume mixing ratios between about 1 and 0.5 nmol/mol. The time constant of the instrument for measurements in the upper troposphere is of the order of 1 s. The time offsets of NO have been shifted about 2-3 seconds based on ice number.

Backscatter profiles of clouds and aerosols were acquired by the lidar system WALES (Water vapor Lidar Experiment in Space, Wirth et al. 2009) at the wavelengths of 532 and 1064 nm. In this study backscatter is used to extract information about the cirrus cloud structures, such as CTH, geometrical depth and others. WALES also provides two-dimensional measurements of the water vapor mixing ratio and aerosol particle linear depolarization ratio. The backscatter ratio and aerosol depolarization (perpendicular to parallel) are used to create a cloud mask, which helps to discriminate for ice clouds. For these clouds the RHi is calculated from the measured water vapor mixing ratio and collocated model temperatures from ECMWF ERA5 reanalysis data. This instrument and method have also been applied by Groß et al. [2014] and Urbanek et al. [2018], who found that the lidar measurements were accurate when compared with in situ data. The statistical error in the retrieval of water vapor by WALES is estimated to be about 5% [Kiemle et al., 2008] and the ECMWF temperatures induce an error of around 10-15% in the final RHi values [Groß et al., 2014].

3.2.2 Water vapor measurements from IAGOS

The European Research Infrastructure IAGOS provides long-term in-situ measurements in the UTLS region. The IAGOS core component, successor of the MOZAIC part [Petzold et al., 2015], comprises the implementation and the operation of autonomous instruments installed on long-range aircraft of internationally operating airlines for continuous, global-scale and daily measurements of reactive gases and long-lived greenhouse gases (e.g. CO, CO_2, CH_4 and water vapor), important chemically active trace gases (e.g. O_3), as well as aerosol, dust and cloud particles [Filges et al., 2015]. Especially in the UTLS region, these measurements are very valuable as most flight tracks are situated in heights between 9 to

13 km, depending on the actual weather conditions, seasons and geographic regions.

Starting from August 1994 more than 60,000 flights have been performed, including data from the IAGOS predecessor MOZAIC (August 1994 to December 2014) and data from the IAGOS project starting in July 2011 until 2020. It is obvious that the global data distribution is not uniform in every region. The subset covering the NAR shows the highest coverage of flights. Thus, the 10-year RHi measurements from 2000 to 2009 over the NAR in Figure 3.2 in Reutter et al. [2020] are used as an example to illustrate the water vapor measurements from IAGOS. RHi depends on both temperature and available water vapor. Hence, RHi is a convolution of both variables. In the troposphere, up to the tropopause layer, the statistics cover the whole range of saturation values until 200%. Overall, 50% of the data in the upper troposphere are situated between 50% and 100% RHi. The highest median values are found in the highest troposphere. In the tropopause layer, still a significant amount of data is exceeding values of RHi > 100%. In the stratospheric layers, the median of the RHi values is decreasing strongly. However, ice supersaturation is still possible, especially in the lowest stratospheric layer [Kaufmann et al., 2018, Müller et al., 2015].

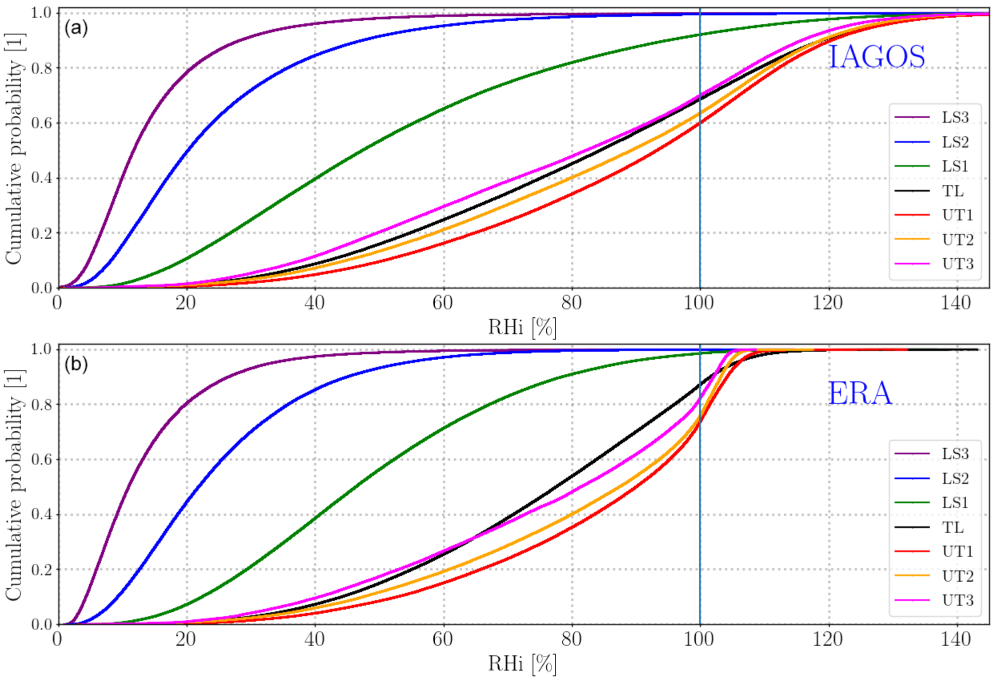

Figure 3.2: Cumulative distribution of RHi for every height level in the IAGOS (a) and ERA (b) data sets. The vertical blue line denotes saturation with respect to ice. From Reutter et al. [2020].

In contrast to the combination of a frost point hygrometer and a photoacoustic hygrometer used for Civil Aircraft for the Regular Investigation of the atmosphere Based on an Instrument Container (CARIBIC), IAGOS uses a capacitive sensor, which shows a worse precision and uncertainty for very low water vapor volume mixing ratios. Therefore, the uncertainties in volume mixing ratios of water vapor are large in the lower stratosphere and may explain the more wet stratospheric values compared to CARIBIC [Petzold et al., 2020].

In my study the NAR area is also focused on. For the establishment of humidity prediction models based on ANN, this study profits from the high-resolution IAGOS measured values than ERA5 data. The geographic position of the airplane, the time, data quality flags, ambient pressure and temperature [Berkes et al., 2017], water vapor volume mixing ratio and RHi data set from IAGOS in the year 2020 are collected as the output of the ANN model training, and collocated with ECMWF ERA5 (see Chapter 6), which works as the input, accordingly.

3.3 Thermodynamic conditions and dynamical states from ERA5

ERA5, the evolution of the ERA-Interim reanalysis [Dee et al., 2011], is the fifth generation ECMWF reanalysis for the global climate and weather [Hersbach et al., 2020]. The data assimilation combines a previous forecast (12 hours before the given time at ECMWF) with newly available observations in an optimal way to produce a new best estimate of the state of the atmosphere. Then the analysis data is issued as an updated and improved forecast. Reanalysis works in the same way, but at reduced resolution to allow for the provision of a data set spanning back several decades. ERA5 is updated daily with a latency of about 5 days.

ERA5 provides hourly estimates for a large number of atmospheric, ocean-wave and land-surface quantities. Data is available from 1940 onwards. These quantities have been regridded to a regular lat-lon grid of 0.25 degrees for the reanalysis (0.5 degree for ocean waves). Four main subsets refer to hourly and monthly products, both on pressure levels (upper air fields) and model levels. In this study, the hourly atmospheric parameters on pressure levels but not dense model levels are used to reduce the size of the data set used and minimize the computation time. Notably, this might already introduce an uncertainty as the pressure level values are interpolated from the model levels.

Temperature in the atmosphere can be used to convert water vapor mixing ratio to specific humidity. **Specific cloud ice water content** (in kg/kg) is the mass of cloud ice particles per kilogram of the total mass of moist air. The total mass of moist air is the sum of the dry air, water vapor, cloud liquid, cloud ice, rain and falling snow. This parameter is used to distinguish between the cirrus and the cirrus-free regions during the validation of the humidity prediction model. **Relative humidity with respect to ice** (in %) is the water vapor pressure as a percentage of the value at which the air becomes ice saturated (the value at which the water partial pressure over the ice surface in equilibrium with the air with respect to evaporation). **Specific humidity** (in kg/kg) is the mass of water vapor per kilogram of moist air.

Geopotential (in $\mathrm{m^2\,s^{-2}}$) is the potential energy per unit mass of the Earth's gravity field. The geopotential height is calculated through dividing the geopotential by the Earth's gravitational acceleration. The geopotential height plays an important role in synoptic meteorology, in which field it can be used to identify weather systems such as cyclones, anticyclones, troughs and ridges. **Vertical velocity** (in Pa/s in the pressure based vertical co-ordinate system used by ECMWF) is the speed of air motion in the upward or downward direction. Here, negative values of vertical velocity indicate upward motion. Vertical velocity can be useful to understand the large-scale dynamics of the atmosphere, including areas of upward/downward motion and ascent/subsidence. **Divergence** (in $\mathrm{s^{-1}}$) represents the horizontal divergence of velocity, indicating the rate at which air spreads out horizontally from a point per square metre. This parameter is positive when air is spreading out, or diverging. **U/V-component of wind** (in m/s) correspond to the eastward/northward component of the wind, denoting the horizontal speed of air moving towards the east/north. A negative sign indicates air moving towards the west/south. Combining these parameters provides the speed and direction of the horizontal wind. **Relative vorticity** (in $\mathrm{s^{-1}}$) is a measure of the rotation of air in the horizontal plane around a vertical axis relative to a fixed point on the Earth's surface. In weather systems, troughs are associated with anticlockwise rotation (in the northern hemisphere), and ridges are associated with clockwise rotation. **Potential vorticity** in $\mathrm{km^2\,kg^{-1}\,s^{-1}}$ measures the ability of air to rotate in the atmosphere. Its significant increase above the tropopause makes it valuable for studies related to the stratosphere and stratosphere-troposphere exchanges. This parameter is used to distinguish the UT or LS during the validation of the humidity prediction model.

3.4 The libRadtran radiative transfer model

To calculate broadband solar and thermal irradiances at TOA for ice particles, the sophisticated radiative transfer package libRadtran is used [Mayer and Kylling, 2005, Emde et al., 2016]. Water and ice clouds are represented in this model in detail and realistically. Optical properties of water droplets are computed using Mie scattering theory and tabulated as a function of wavelength and R_{eff}. Ice crystals are not spherical in shape and habit [Letu et al., 2016], and for this simulation the parameterization of Baum et al. [2014] for ice crystal habits has been employed to define the conversion from optical to microphysical properties. In analogy to the MODIS products [Yang et al., 2018], rough aggregates are selected for ice crystal shape (see Chapter 4.2.1 for a discussion about this choice). The selected one-dimensional radiative transfer solver is DISORT (Discrete Ordinate Radiative Transfer) 2.0 with 16 streams [Stamnes et al., 2000]. LibRadtran incorporates Kato et al. [1999] and Fu and Liou [1992] parameterizations for integrated broadband irradiance calculations and recommends the REPTRAN band parameterization with a spectral resolution of $15\,\mathrm{cm^{-1}}$ for spectral calculations [Buehler et al., 2010, Gasteiger et al., 2014].

3.5 CoCiP contrail cirrus prediction model

The Contrail Cirrus Prediction Model (CoCiP) is used to predict the contrail cirrus cover and analysis of contrail climate impact produced from individual flights [Schumann, 2012, Schumann et al., 2012, 2017, 2021b, Teoh et al., 2020, Voigt et al., 2017]. The contrail model uses traffic data from EUROCONTROL's model 3 for a large part of Europe and from the North Atlantic Tracks (NATS) for the Shanwick Oceanic Control Area. Performance parameters, including fuel consumption and overall propulsion efficiency, are estimated using the Base of Aircraft Data (BADA) 3 from EUROCONTROL [Nuic et al., 2010] and a recently developed performance model for a set of subsonic turbofan-powered transport aircraft at cruise [Poll and Schumann, 2021]. If two consecutive flight waypoints satisfy the SAC, a contrail segment is formed. Contrail initial water content, width and depth are determined by aircraft properties (fuel flow, mass, span, speed etc). Plume dispersion is a function of turbulence, shear, and induced heating. RHi inside contrail plumes is at saturation, and IWC of contrails grows or decreases according to uptake of ambient water. A Runge-Kutta integration simulates the contrail evolution until its end of life by ambient drying or particle losses due to aggregation and sedimentation. The end of contrail life is defined as the point when the ice number concentration is lower than the background ice nuclei ($< 10^3\,\mathrm{m}^{-3}$), $\tau_{contrail}$ is less than 10^{-6} or the maximum contrail lifetime of 24 h is reached.

Soot number emissions are computed with the fractal aggregate model developed in Teoh et al. [2019, 2020]. The initial contrail properties are dependent on the non-volatile particulate matter (nvPM) [Kärcher, 2018]. The nvPM for different aircraft–engine types is calculated and a lower bound of $10^{-13}\,\mathrm{kg}^{-1}$ is set for the activation of organic volatile particles and ambient natural aerosols. The model has also used the latest indication from in situ measurements of contrails that the activation of nvPM particles to form contrail ice particles is not complete when ambient temperatures are near the SAC threshold temperature [Bräuer et al., 2021].

CoCiP simulates the unique properties of individual contrail segments over time, and it accounts for overlapping of contrails above or below clouds present in the meteorological data [Schumann et al., 2021a]. The model uses meteorology from NWP forecast data from ECMWF [Bauer et al., 2015]. The model is set up in Schumann et al. [2021b] with humidity exchange between contrails and the background air and with radiative effects caused by contrail-contrail overlapping. The lack of atmospheric interaction and feedback is a limitation of CoCiP relative to general circulation models [Bickel et al., 2020, Burkhardt et al., 2018, Chen et al., 2012]. The approximation of the contrail-atmosphere humidity exchange in CoCiP induced a 10%–20% reduction in $\tau_{contrail}$ and contrail net RF [Schumann et al., 2015, 2021b], and a parametric analysis suggested that the influences of contrail-contrail overlapping on the net RF is small ($0.3\,\mathrm{mW\,m}^{-2}$) in regions such as the North Atlantic [Sanz-Morère et al., 2021].

The contrail outputs are saved at flight, hourly, waypoint and gridded levels. Contrail cirrus and natural cirrus cover in a grid cell are assumed when their respective optical depth values are above a threshold of 0.1 as shown in Figure 3.3, which corresponds to the satellite

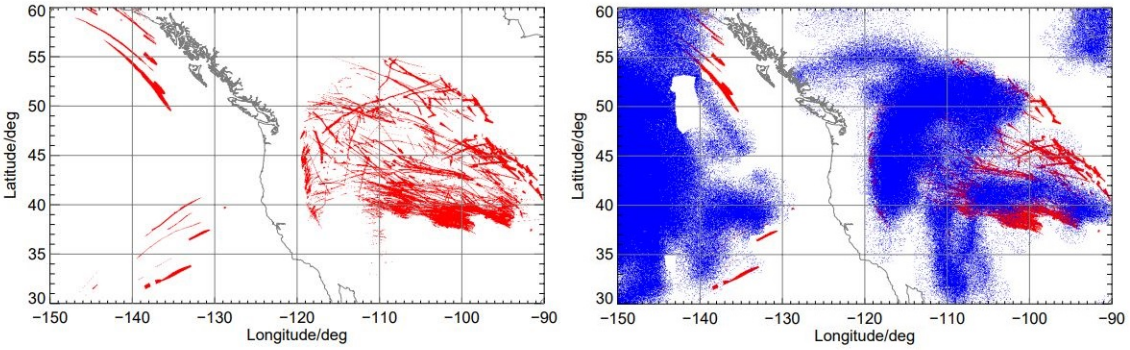
60
55
50
45
40
35
30
Latitude/deg
−150
−140
−130
−120
−110
−100
−90
Longitude/deg
60
55
50
45
40
35
30
Latitude/deg
−150
−140
−130
−120
−110
−100
−90
Longitude/deg

Figure 3.3: Distribution of total cirrus cover composed of natural cirrus and contrail cirrus for a North American region, with a contrail outbreak. Left: contrail cirrus pixels (red); right: natural cirrus pixels (blue) and contrail cirrus pixels (red). Figure adapted from Schumann [2012]

detectability threshold [Mannstein et al., 2010]. Contrail cirrus coverage as a percentage of sky area in a region is defined as the total cirrus cover minus the natural cirrus cover. The local contrail RF of each waypoint is parameterized using the ECMWF modeled radiation data and CoCiP simulated cirrus microphysical properties, and also assuming a contrail habit mixture. The final contrail RF is aggregated to obtain the contrail RF in the domain.

Chapter 4

Observations of a contrail cirrus outbreak over the North Atlantic

This Chapter is adapted from Wang et al. [2023].

Through reflecting incident solar radiation and trapping upwelling radiation within the Earth's atmosphere, the cirrus result in an imbalance of radiation budget in both the shortwave (SW) solar and longwave (LW) terrestrial spectrum [Stuber et al., 2006]. The net radiative forcing (RF) is positive [Rädel and Shine, 2008, Burkhardt et al., 2018, Gettelman et al., 2021] and RF due to contrail cirrus greatly exceeds that from linear contrails [Burkhardt and Kärcher, 2011, Burkhardt et al., 2018]. Knowledge gaps still exist regarding the large variability in the contrail life cycles [Bier et al., 2017], and optical properties which then determine their radiative response to the climate system [Grewe et al., 2017]. It further limits projections of aviation climate impact and formulations of mitigation options other than carbon dioxide (CO_2) emissions [Voigt et al., 2021]. This research background motivates the observations of a contrail cirrus outbreak over the North Atlantic in this Chapter.

In this Chapter, I use in situ data measured during the ML-CIRRUS experiment [Voigt et al., 2017] from the HALO aircraft and simultaneous remote sensing observations [Bugliaro et al., 2011, Vázquez-Navarro et al., 2013, Strandgren et al., 2017a] with high temporal resolution from the SEVIRI imager aboard the geostationary MSG satellite. In particular, this study concentrates on one flight on 26 March 2014 over the NAR just off the coast of Ireland where most of the air traffic from Europe to the US and vice versa takes place. This situation enables to investigate properties and radiative effects of contrail cirrus and ambient natural cirrus in an ideal contrail cirrus outbreak. In particular, a new method is developed to classify cirrus along the HALO flight track from in situ measurements based on enhanced NO aircraft gas emissions and ice number concentrations N into three representative classes: (1) contrails, (2) contrail cirrus and (3) natural cirrus. Satellite observations from MSG/SEVIRI are referred to characterise the general cloud situation and confirm the presence of various contrails, in line with in situ measurements. In a new approach, the ice cloud RF is determined combining in situ and satellite observations with RTM. To this end, reanalysis data from ERA5 [Hersbach et al., 2020] are used. Since

ERA5 does not simulate the effect of air traffic on clouds, I collect atmospheric profiles of water vapor, liquid and ice clouds from this reanalysis and combine them with the in situ and spaceborne observations to provide inputs to the RTM to compute RSR and OLR. After checking the consistency of my radiative transfer calculations with the corresponding RSR and OLR measured with the GERB instrumentation, this study is in the position to compute instantaneous RF of this special combination of clouds in the SW and LW spectral range by excluding the ice cloud layer from the radiative transfer calculations, thus yielding a consistent ice-cloud-free irradiance. To be specific, these calculations are operated to an area encompassing the HALO flight path to compute the diurnal cycle of RF in that region, thus exploiting the information from high resolution airborne measurements as well as geostationary satellite observations with the high repetition rate for a holistic view on the radiation budget from this ideal case in the NAR.

4.1 Microphysical properties of contrail cirrus and natural cirrus

This section describes how airborne data from HALO and images from satellite remote sensing are combined to understand microphysical properties of contrail cirrus and natural cirrus, and the corresponding variation when contrails transit into contrail cirrus within the contrail life cycle.

4.1.1 General situation

In the night and the very early hours of 26 March 2014 a ridge cirrus cloud band built up North of Ireland down to the Southern tip of Portugal (Figure 4.1). Close to Iceland as well as to the South-West of Ireland this cirrus cloud thickened (optical thickness larger than 1 at 10:45 UTC, Figure 4.1d). While exactly off the coast of Ireland, in coincidence with the eastbound morning and westbound afternoon air traffic to and from the US, many linear structures can be seen in SEVIRI observations (Figure 4.1, especially Figure 4.1b where BTD between the SEVIRI channels at 10.8 and 12.0 µm are shown) and the ice cloud is thinner (optical thickness around 0.3 at 10:45 UTC). Please notice that Figure 4.1 is enlarged in Figure 4.2. Considering that the peak of eastbound morning air traffic is approx. at 3 UTC [Graf et al., 2012], under favourable conditions with low temperature and high humidity contrails induced from these aircraft are expected to form and live for hours such that they can be identified in MSG observations in the morning of the same day. This cloud band evolves with time towards the South, and in correspondence of the Ireland coast the ice clouds dissipate around noon. In addition, this thin bluish/violet ice cloud band partly overlaps with a liquid water cloud field below (yellowish clouds in the false colour composite in Figure 4.1a).

Due to its approx. 3.5 km×4.5 km spatial resolution, SEVIRI can only observe contrails that have already grown larger (and thicker) while young contrails cannot be detected [Mannstein et al., 2010]. Nevertheless, the satellite observations indicate that because of

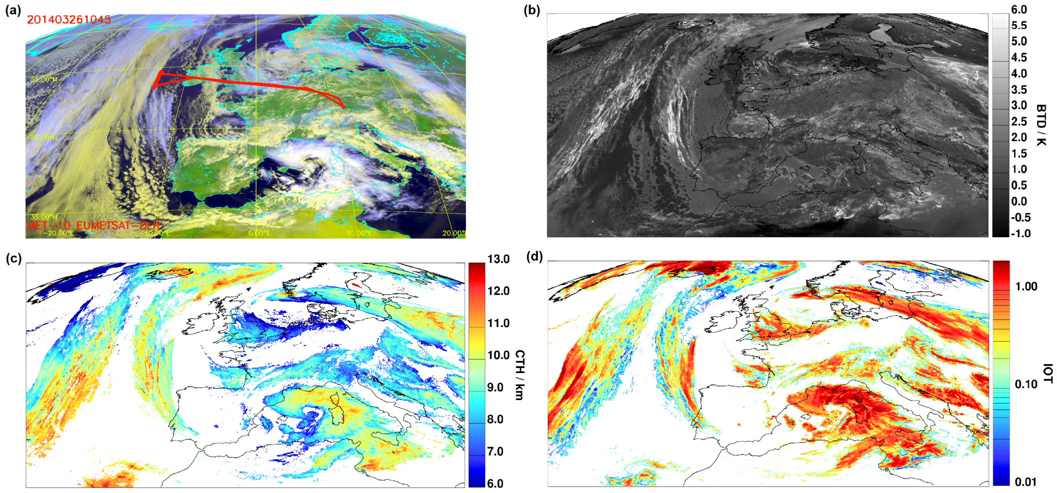

Figure 4.1: (a) The false color RGB image from MSG/SEVIRI overlapped with the HALO flight track on 26 March 2014 at 10:45 UTC showing Europe and the Eastern part of the North Atlantic Ocean, (b) corresponding 10.8 µm and 12.0 µm BTD (K) with overlaid ice clouds, (c) CTH and (d) IOT from CiPS.

these favourable meteorological conditions and the relatively high air traffic density in this region, contrails from various aircraft could form over a long time period (12 h) that overlap with “the remnants” of previous contrails. Thus, air traffic in this area has a strong impact on cloudiness on 26 March 2014.

On 26 March 2014 the HALO aircraft started from Oberpfaffenhofen in Germany at approximately 05:30 UTC and probed the cirrus over NAR from around 08:00 to 11:30 UTC with a race track pattern between approx. 51.5°N and 54°N at a longitude of ca. -14°E (-13.6 to -14.4°E), see the flight track in Figure 4.1a and also [Voigt et al., 2017, Figure 4]. In this area, HALO flew 3 lidar legs almost perpendicular to the NAR tracks (07:57 UTC - 08:35 UTC, south to north, 09:17 UTC - 09:30 UTC, north to south, and 10:21 UTC - 10:52 UTC, south to north), each followed by in situ legs at different altitudes.

Figure 4.2 presents the temporal variation of contrails and surrounding clouds with one HALO in situ/lidar leg at close time and air traffic data 2 to 3 hours before, from 08:30 (the first in situ leg) to 10:30 UTC (the third lidar leg). In addition, the area around the flight path is investigated in Chapter 4.2.2 in more detail but that serves here as orientation to easily capture the temporal evolution of the ice clouds. The wind speed in the east-west direction fluctuates around 0 while winds in the north-south orientation drive the ridge cloud to move southwards (blue arrows in Figure 4.2 indicate wind direction at 225 hPa from ERA5). The aircraft flight to and from Europe. In the BTD images – where SEVIRI brightness temperatures at 10.8 µm and 12.0 µm are subtracted from each other - the black areas are caused by the low-level clouds, while the bright pixels correspond to thin cirrus. Small ice crystals, for instance in contrails, correspond to the largest BTDs. From 08:30 UTC, many thin lines (contrails) are seen in the false colour RGBs in the first column

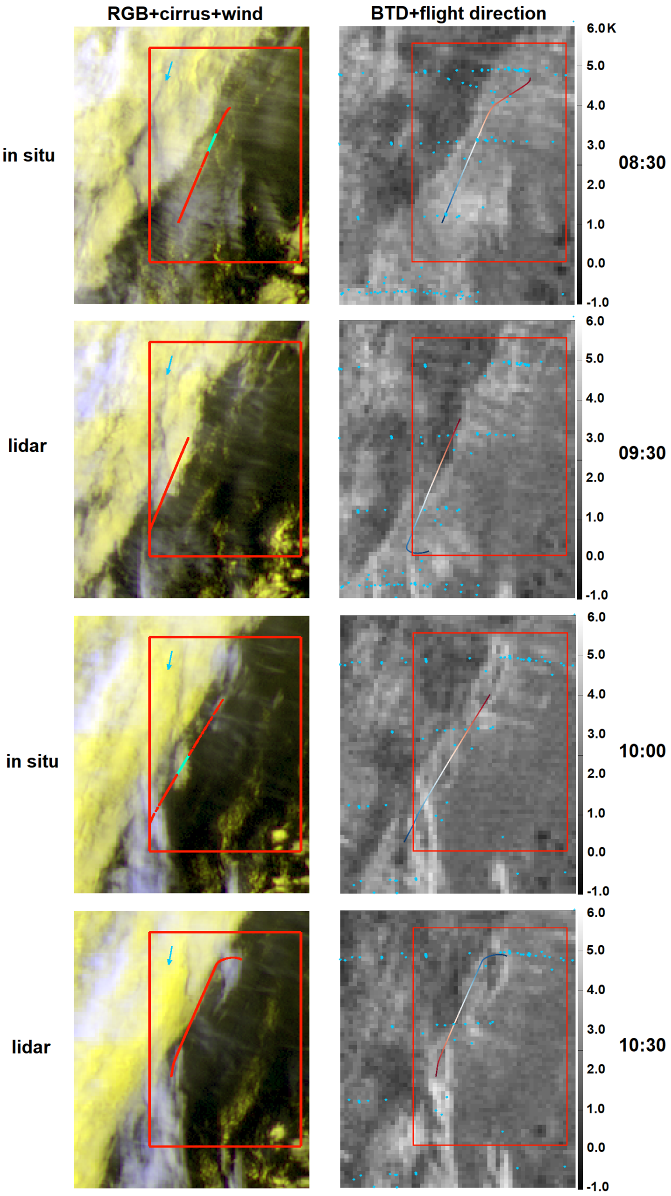
RGB+cirrus+wind
BTD+flight direction
in situ
lidar
in situ
lidar
08:30
09:30
10:00
10:30
6.0K
5.0
4.0
3.0
2.0
1.0
0.0
-1.0

Figure 4.2: Time series of contrail cirrus and surrounding clouds from MSG/SEVIRI observations over the NAR corridor on 26 March 2014. The first column: RGB-composite with overlaid cirrus, low-level liquid clouds pixels and in situ/lidar HALO leg at close time. The red and green line of the HALO flight track represent contrail cirrus and natural cirrus, respectively. The blue arrow indicates the wind direction almost perpendicular to the line shaped structures of the contrail cirrus. The second column: 10.8 µm and 12.0 µm BTD (K) with overlaid cirrus pixels. Blue points show air traffic data set interpolated to MSG grid from M3 and NATS. The color of the HALO flight track indicates the flight direction. HALO flies from red to blue part. Top to bottom: 08:30, 09:30, 10:00 and 10:30 UTC. The red area is investigated in Chapter 4.2.2.

in Figure 4.2, where also the HRV channel was used. They run parallel to most air traffic routes (blue diamonds in the second column) and are intersected perpendicularly by the HALO route. Some of the contrails are also visible in the BTD pictures (the second column in Figure 4.2), that have a lower spatial resolution than the HRV channel, thus indicating the presence of small ice crystals. These contrails form a thin cirrus layer, potentially of anthropogenic origin but also with natural ice clouds (see discussion of Figure 4.3 below). In the South, the ridge cirrus is thicker and no contrails can be observed. At 09:30 UTC, the flight area is dominated by contrails. With time, from 08:30 to 10:30 UTC the typical contrail lines become always fainter and less in number. Thus, contrails begin either to dissipate or to lose completely their linear shape due to wind shear such that they turn out to be indistinguishable. However, contrails can be still observed in the north-eastern part of the satellite images at later times.

Figure 4.3 presents the backscatter ratio at 532 and 1064 nm from the WALES lidar measurements in that sequences. The lidar data show that the geometrical thickness of high-level clouds reduces from 2.0 km at 08:30 UTC to 1.5 km at around 11:00 UTC. The temporal evolution of CTH from WALES shows that the cloud first reached up to approximately 12 km and slowly descended to slightly above 11.5 km, with backscatter values becoming smaller with time, in line with the passive observations that indicate dissipation of the cloud during the day. For the investigation of contrails from in situ measurements this study concentrates on the time period between 08:30 and 11:30 UTC, but this time is extended to cover the period from 6:00 UTC to 14:00 UTC in Chapter 4.2.2.

Considering the three WALES legs in more detail (Figure 4.3), in leg 1 between 08:10 and 08:25 UTC there is a series of connected fall streaks with high backscatter at a height of 11 km below a thin ice cloud layer top at 12 km. These structures resemble those in the large eddy simulations by Unterstrasser et al. [2017a,b] where they considered contrails within natural cirrus. Thus, these bright spots with their fall streaks can probably be identified as contrails, with many small ice particles causing high backscatter and with larger ice crystals sedimenting down. For leg 1, these contrails make up the majority of the cloud in this temporal interval. The presence of developed fall streaks is a hint that these contrails are aged (> 30 min). Unfortunately, the high WALES backscatter inhibits the determination of RHi (Figure 4.4) for these bright spots, but the upper level of the clouds, just below the potential contrails, show occasional ice supersaturation, with RHi above 100%.

Lidar leg 2, much shorter than the other two, also shows the presence of some spots with elevated backscatter ratios, although less numerous, at an altitude of 11 km at 09:26 UTC. Unlike leg 1, many high backscatter spots do not show extended fall streaks, suggesting the presence of younger contrails in addition to older ones. Furthermore, the top ice layer above 11.5 km also contains some very high backscatter areas. Finally, also above 9 km some clouds are visible that resemble contrails (or a dissipating cirrus). Thus, in this leg the contrail-like structures do not fill the entire cloud as in leg 1, but there are indications of young and older contrails, in addition to natural cirrus. The last lidar leg 3 took place 1 h later and also shows various bright spots at different levels, from 10 to almost 12 km, and elongated vertical structures that remind of those in leg 1. The cloud as a whole is

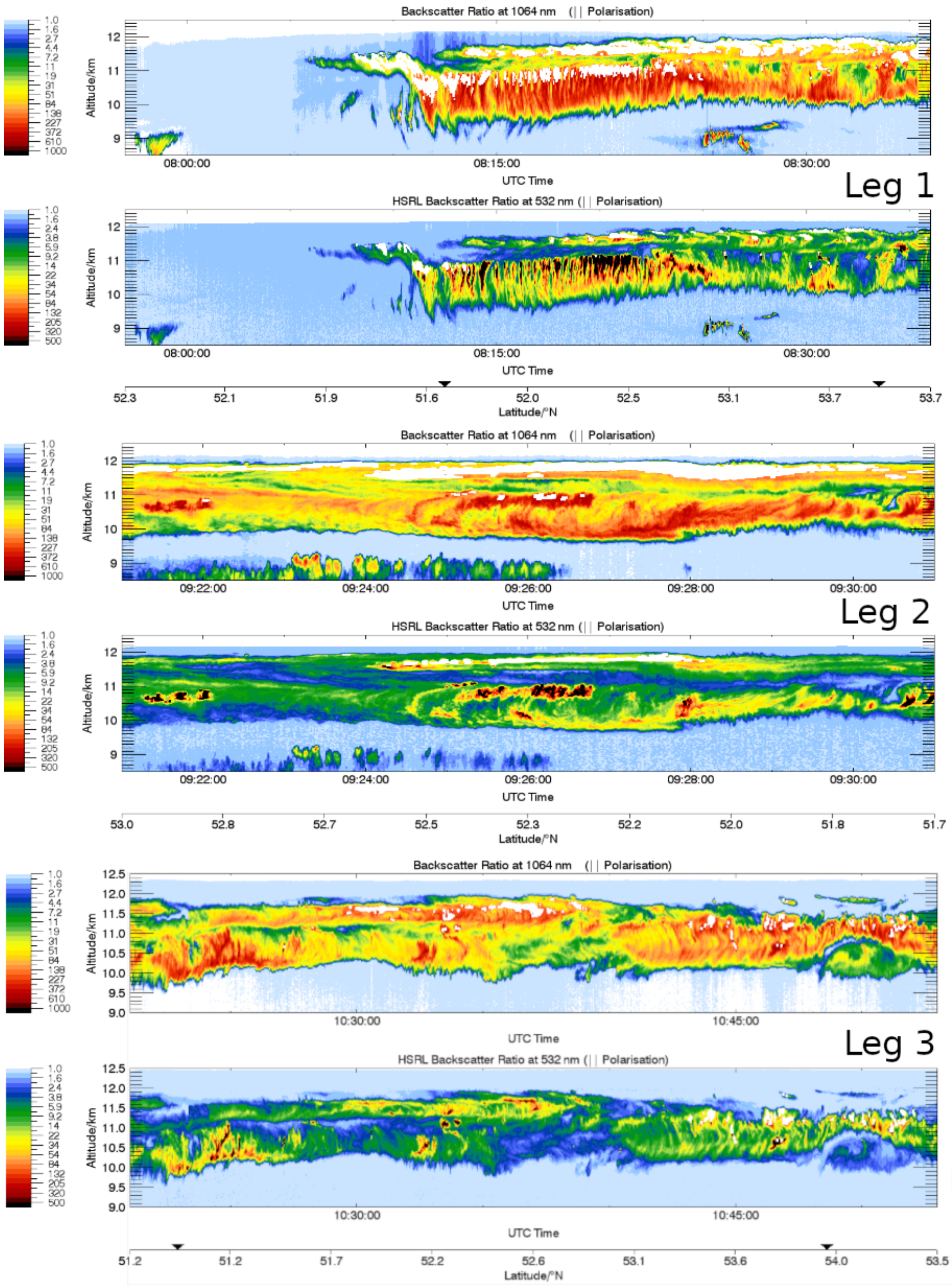

Figure 4.3: The three panels show the three lidar legs with backscatter ratios at 1064 nm and 532 nm.

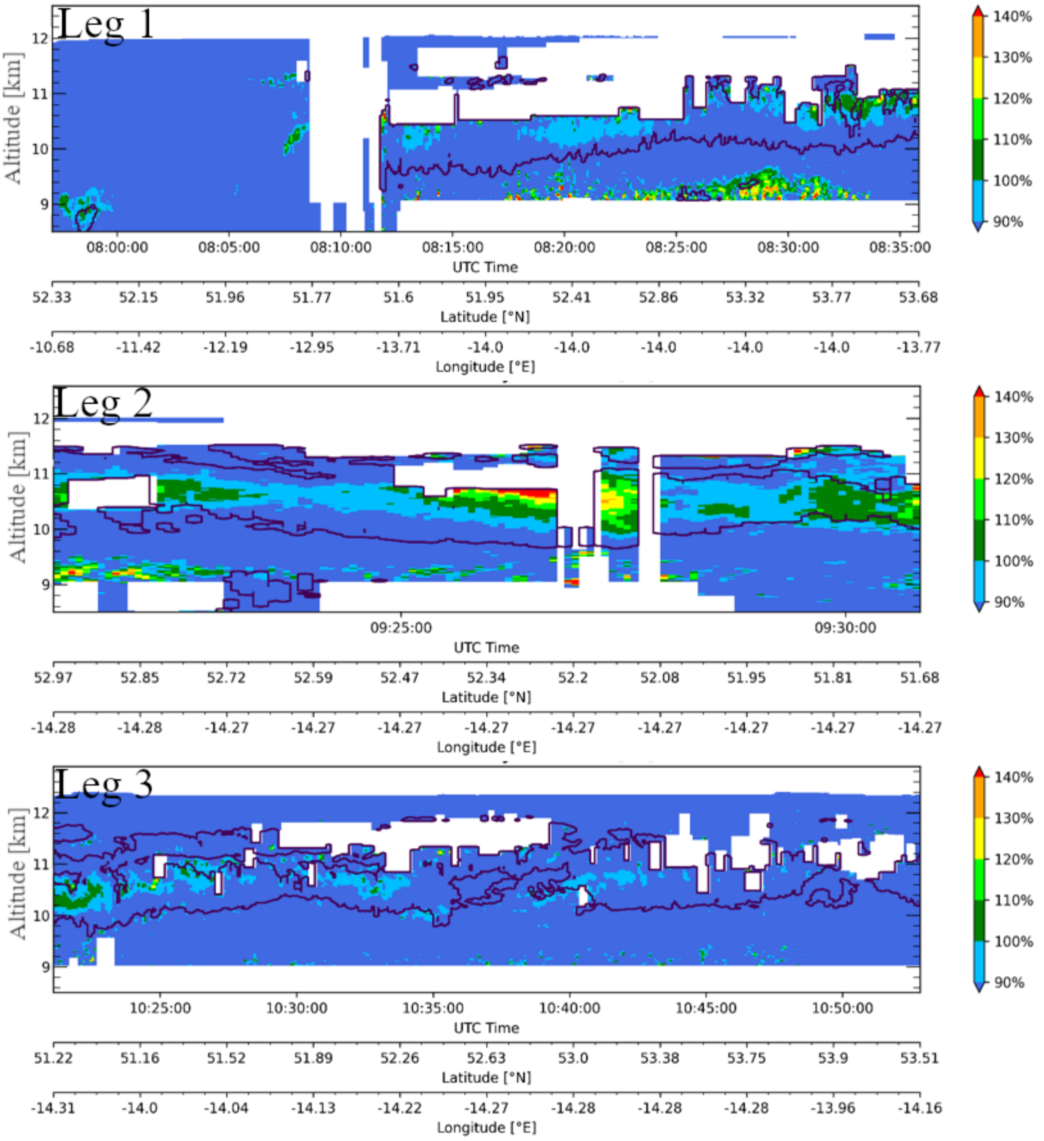

Figure 4.4: The three panels show the RHi from Figure 4.3 in more detail. The black contour represents the cloud edge. White areas are due to lack of measurements in these regions, because of detector saturation.

slightly lower than that in leg 1 with ragged edges especially at its lower border, suggesting that the cloud is sublimating and thinning out. This is confirmed by the RHi observations of WALES for leg 3 in Figure 4.4, where subsaturation is indicated especially at the lower and upper edges, while around 10.5 km at selected locations RHi reaches saturation. These WALES measurements are indicative for the cloud probed between 08:00 and 11:30 UTC but cannot directly be compared to in situ observations taken at different times in between.

4.1.2 Identification of contrails, contrail cirrus and natural cirrus

In this Chapter, a method already used in Voigt et al. [2010] was improved to identify where aircraft emissions are fresh, older or not detectable by using in situ measurements. These three situations are assigned to contrails, contrail cirrus and unperturbed cirrus, also called natural cirrus. The goal is to investigate microphysical and optical properties of these clouds. Figure 4.5 shows the full sequence of the airborne in situ measurements of N (N_{CAS}, N_{CIP}), R_{eff}, NO, cirrus (identified using the method in this Chapter), RHi, latitude and altitude as a function of time between 08:30 and 11:30 UTC. N for both instruments, CAS and CIP (N_{CAS} and N_{CIP}) and R_{eff} (Figure 4.5a, b) indicate the occurrence of cirrus at the flight levels between 10 km and 13 km (Figure 4.5g). According to the dilution equation by Schumann et al. [2017] and assuming 1000 particles/cm^3 for 1 s-old contrail, many contrails probed here are more than 1 h old. Furthermore, some contrails are also visible in the low-resolution MSG/SEVIRI satellite images (BTDs in Figure 4.2) and therefore at least 1-2 h old [Vázquez-Navarro et al., 2015]. Figure 4.5c thus shows variable NO concentrations and various peaks. Since other sources of NO are unlikely in this situation (no thunderstorms in the previous 12 h, no wildfires), it is assumed that the NO concentration increases correspond to aviation exhausts, with different peak heights caused by various factors such as contrail age, dilution and aircraft type [Voigt et al., 2010, Jurkat et al., 2011, Jeßberger et al., 2013, Schumann et al., 2013]. In fact, after the emission, NO is mixed with the surrounding air and dilutes with increasing plume age such that its measured mixing ratio can be used as a rough indication for contrail age. Also, for contrails initial ice particle concentrations N are high due to the high number of soot particles emitted by the engine [Schlager et al., 1997, Kleine et al., 2018, Bräuer et al., 2021] and N decreases due to dilution [Schumann et al., 1998] and further processes [Bier et al., 2017, Unterstrasser et al., 2017a]. High NO emissions without coincident ice crystal observations correspond to situations where the SAC is not satisfied and no contrail is formed. This study, similarly to Voigt et al. [2010], uses N and NO to evaluate contrail evolution. Since the contrails detected during this flight are older, the lower threshold for the particle size was chosen to be 3 µm to neglect any influence from aerosol particles in the size range below 3 µm. This is consistent with other cirrus and contrail cirrus studies [Voigt et al., 2017, Righi et al., 2020].

First, the NO background concentration $NO_b(t)$ at a given time t was determined dynamically by taking the minimum NO value in a 60-second sliding window around this time (Figure 4.5c)

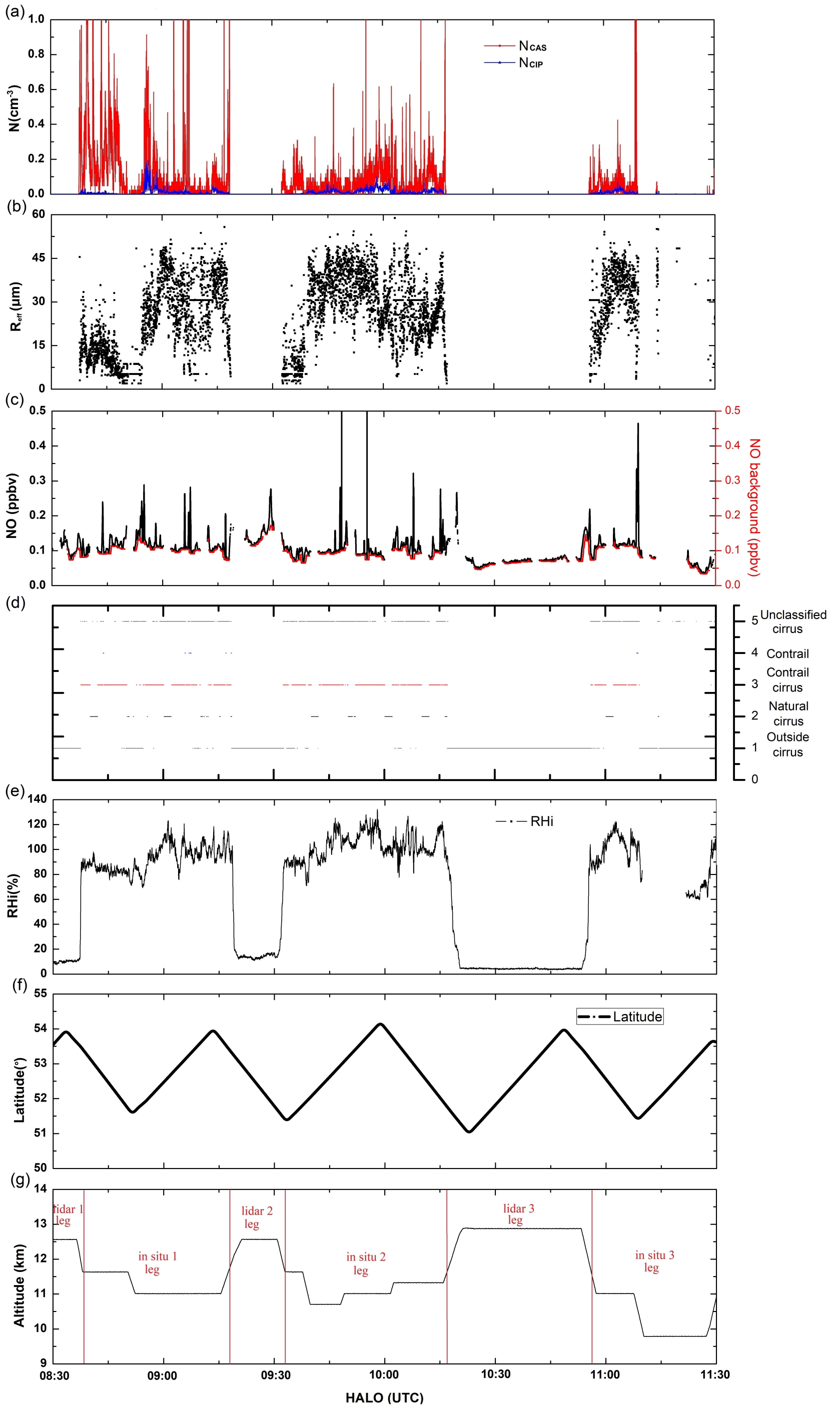

Figure 4.5: In situ measurements of HALO on 26 March 2014 over the North Atlantic region, including (a) ice number concentration N, (b) $R_{eff} > 1.5\,\mu m$, (c) NO and NO background, (d) cirrus classification, (e) RHi, (f) flight latitude, and (g) altitude.

$$NO_b(t) = min_{-30s\leq \Delta t \leq -30s} NO(t + \Delta t) \tag{4.1}$$

$NO_b(t)$ takes care of the natural variability of NO in this situation. Notably, the RANSAC algorithm [Fischler and Bolles, 1981] is used to interpret NO outliers and confirm that they haven't hit the NO background but the peaks of NO values. The difference between $NO_b(t)$ and $NO(t)$ at each time t is termed $\Delta NO(t)$.

$$\Delta NO(t) = NO(t) - NO_b(t) \tag{4.2}$$

In a further step ice number concentration N is considered to classify contrails. In accordance with Table 4.1, I first distinguish measurements in cirrus from "1. outside cirrus" when N_{CAS} and N_{CIP} are zero in step 1, and then separate "3. contrail cirrus" and "4. contrails" from "2. natural cirrus" when NO is higher than the background and N_{CAS} or N_{CIP} is larger than 0.03 cm^{-3} in step 2, reflecting the impact of air traffic. The rest is labelled as "5. unclassified cirrus" in step 3. This class contains on one side those clouds that cannot be classified and likely consists mainly of natural cirrus. On the other side, ice cloud measurements with high ΔNO ($>$ 0.14 ppbv) but moderate N ($N_{CAS} \leq 0.4 cm^{-3}$) do also fall in this category and should represent observations in younger plumes where few ice crystals could form (maybe because temperature is close to the Schmidt-Appleman criterion) or because ambient air is subsaturated leading to the evaporation of a considerable fraction of newly formed (small) ice crystals. Summarised, natural cirrus is identified when ice crystals are present with either N_{CAS} or N_{CIP} larger than 0.03 cm^{-3} and NO close to the background value, i.e. $\Delta NO \leq 0.02$ ppbv; contrail cirrus is characterised by moderate values of NO, i.e. 0.02 ppbv $< \Delta NO \leq 0.14$ ppbv, and N_{CAS} or $N_{CIP} > 0.03\,cm^{-3}$; contrails are assumed to consist of many small ice crystals, $N_{CAS} > 0.4\ cm^{-3}$, and high NO peaks, i.e. $\Delta NO > 0.14$ ppbv. The remaining cirrus is denoted as "unclassified cirrus".

Table 4.1: Cirrus classification according to microphysical properties (N), and tracer measurements (NO) measured by instruments aboard HALO.

Designation	N / cm^{-3}	ΔNO / ppbv	Note
1. Outside cirrus	$N_{CAS} = 0$ and $N_{CIP} = 0$	Any value	Step 1
2. Natural cirrus	N_{CAS} >0.03 or N_{CIP} >0.03	$\Delta NO \leq 0.02$	Step 2
3. Contrail cirrus	N_{CAS} >0.03 or N_{CIP} >0.03	0.02 <$\Delta NO \leq 0.14$	
4. Contrails	N_{CAS} >0.4	ΔNO >0.14	
5. Unclassified cirrus	The rest		Step 3

The determination of ΔNO and N thresholds are explained in Figure 4.6. The threshold values for ΔNO (0.02 ppbv and 0.14 ppbv) have been determined from the ΔNO distribution. ΔNO distribution decreases from 0.0 to 0.48 ppbv, with the largest bins being the first and the second one ($0 \leq \Delta NO < 0.02$ ppbv). Thus, I consider NO to be close to the background value when $\Delta NO \leq 0.02$ ppbv and to contain additional NO when $\Delta NO >$ 0.02 ppbv. The NO occurrences sink by two order of magnitude (from 10^3 to 10^1) until ΔNO equals 0.25-0.30 ppbv. After these values, a tail of relatively seldom high ΔNO values (occurrences $\sim 10^1$) is observed. In order to distinguish old emissions from younger ones, the threshold of $\Delta NO = 0.14$ ppbv is selected, in the middle of the range mentioned above. Thus, ΔNO between 0.02 and 0.14 ppbv are assumed to capture only older emissions, leaving high NO peaks as well as moderate ones in the range $\Delta NO > 0.14$ ppbv (representing the highest 5% ΔNO). For the determination of N thresholds for contrails I proceed similarly. In particular, $N_{CAS} < 0.03\,cm^{-3}$ contains an order of magnitude more observations than the next one. Again, a value in the middle ($0.4\,cm^{-3}$) is taken as separation between high N_{CAS} peaks attributable to contrails and moderate values of N_{CAS} $< 0.4\,cm^{-3}$ that are assigned to older contrails/contrail cirrus. Please notice that N and NO are selected independently. Notably, these values are just valid for this flight sequence over the NAR on 26 March 2014 during the ML-CIRRUS campaign.

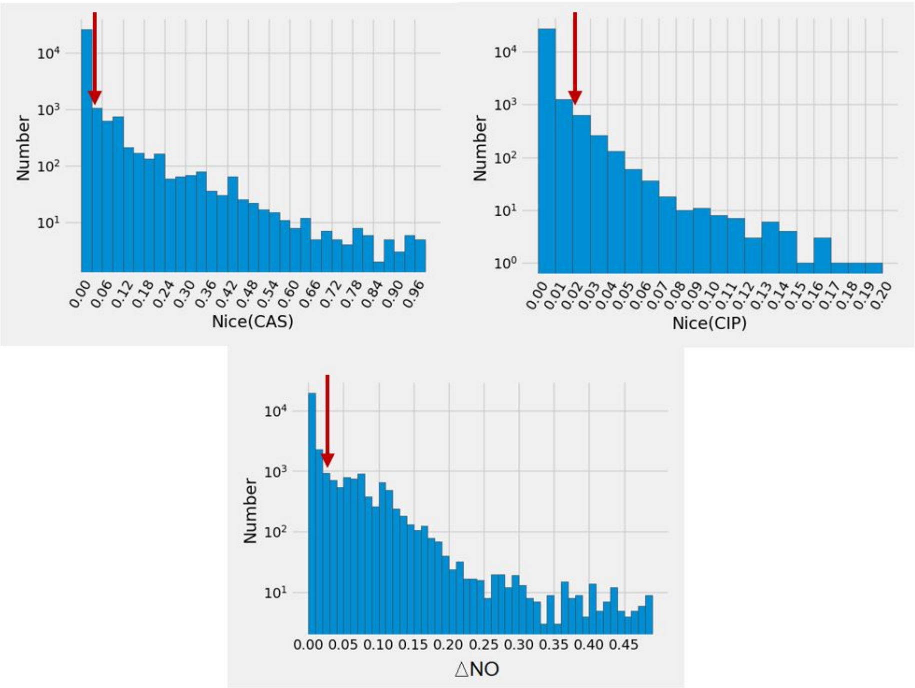

Figure 4.6: Histograms of in situ measured N from CAS and CIP and ΔNO on 26 March 2014 over NAR.

In total, from 08:30 to 11:30 UTC for each aircraft measurement with a frequency of 1 Hz this method has classified 49 contrail observations, 1018 contrail cirrus observations and 2342 natural cirrus observations in Figure 4.5d from in situ measurements. Unclassified cirrus encompasses 2472 cases, with 94 of them having $\Delta NO > 0.14$ ppbv. At least 31% of all classified cirrus was in contrails or contrail cirrus, confirming the indications gained from MSG and WALES in Chapter 4.1.1 about the large number of contrails.

4.1.3 Effective radii

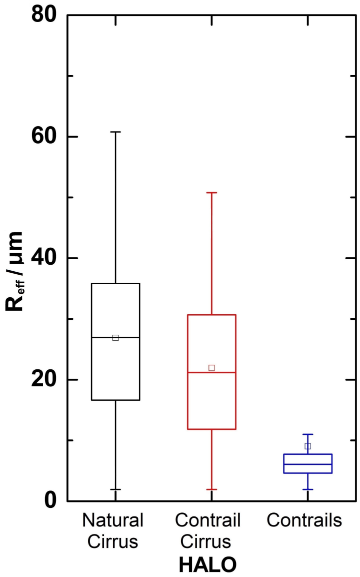

Figure 4.7: R_{eff} of natural cirrus, contrail cirrus and contrails from HALO in situ measurements. Each bar contains the information of the maximum, minimum, interquartile range (25% percentile to 75% percentile), median (horizontal line) and mean (square) R_{eff}.

Considering the entire flight and separating R_{eff} measurements according to our classification enables us to study the statistical properties of the ice crystal sizes. From Figure 4.7, contrail cirrus R_{eff} probed from airborne instruments are smaller than those of natural cirrus, with an average R_{eff} of about 22 µm. The natural cirrus has an average R_{eff} of 27 µm, which is at the lower end of the particle size distributions observed in natural cirrus [Schröder et al., 2000]. The mean radii of contrails or contrail cirrus from in situ measurements is 18% smaller than that of natural cirrus. From contrails to contrail cirrus, the mean and medium R_{eff} mainly show an increasing tendency by an average difference of 13 µm (144%) for this situation. Despite the uncertainty of probed particle sizes, the radii of natural cirrus reached up to 60 µm, while the majority of maximal R_{eff} of contrail cirrus topped at 51 µm, in agreement with findings of Voigt et al. [2017]. This is consistent with the physical picture that contrails form initially as small particles and increase in size by water vapor uptake in ice supersaturated air. If no supersaturation is present, contrails dissipate. Still, contrail cirrus as well as natural cirrus can consist of sublimating particles when air becomes subsaturated [Kübbeler et al., 2011].

In sum, satellite, lidar and in situ measurements give combined evidence for an ideal case of a contrail cirrus outbreak with a high fraction of contrails and contrail cirrus embedded in natural cirrus. In the following, its radiative impact is investigated.

4.2 Radiative effects of contrail cirrus and natural cirrus

Here, a new estimation method is developed for TOA net instantaneous cirrus RF that relies on satellite and in situ observations. TOA irradiance of the contrail cirrus outbreak can be observed, but the comparable situation without ice clouds has to be obtained from another source, e.g. from the surroundings (like e.g. in Vázquez-Navarro et al. [2015] for contrails) or from model simulations (Haywood et al. [2009] for contrail cirrus). The instantaneous net RF at TOA is the change of the total irradiation under a situation with cirrus minus the irradiances in the same situation without cirrus. The equations to compute the RF at TOA are shown in Eqs. 2.31 to 2.33.

However, the two values (TOA irradiance with cirrus and without cirrus) are similar in size since contrail cirrus represent a small perturbation. In fact, both in Vázquez-Navarro et al. [2015] and Haywood et al. [2009] taking the difference between the cirrus contaminated and the cirrus-free irradiances leads also to negative values of RF in the thermal range (OLR with ice clouds is larger than OLR without ice clouds) or to positive RF in the solar range (RSR with ice clouds is smaller than RSR without ice clouds). This is unphysical and we would like to avoid it. To this end, in Chapter 4.2.1 I developed a new method based on RTM calculations exploiting airborne measurements, satellite observations and ERA5 model atmospheric data that produces TOA irradiance fully consistent for both cirrus and cirrus-free regions. Finally, to ensure that TOA irradiance calculated this way is realistic, I compare our RTM simulations of RSR and OLR for the cirrus contaminated case with satellite observations of RSR and OLR from RRUMS at pixel level. An additional comparison on a 3×3 pixel scale with the more accurate GERB products is performed to assess the RRUMS accuracy on this particular day in Figure 4.8.

GERB products (RSR_{G} and OLR_{G}), comprising 3×3 pixels of SEVIRI, are compared with RRUMS results along the HALO flight trajectory. Notably, different cirrus classifications have the same TOA value from GERB products and RRUMS results since the spatio-temporal resolution of the in situ data is much higher than that of SEVIRI. I first remove the 7.5% bright bias and 1.3% cold bias of the GERB irradiances in the solar and thermal range [Clerbaux et al., 2009] to build new revised-GERB data sets. I then calculate the 3×3 pixel mean values of RRUMs results. The corresponding RSR_{R} correlates well with RSR from GERB (RSR_{G}: CC = 0.72), but RRUMS tends to overestimate GERB. In terms of OLR, the agreement is good, with a MAE around 6 Wm^{-2} and a CC of 0.80 for OLR_{R} and OLR_{G}.

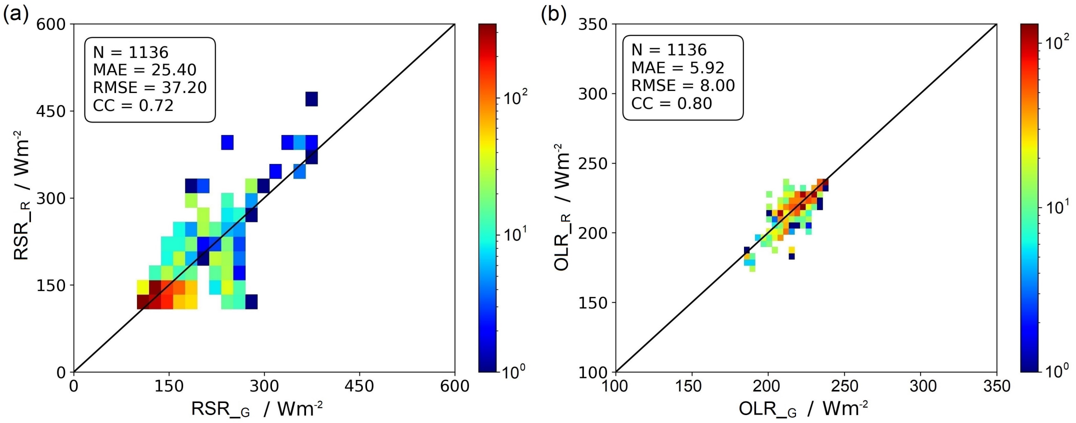

Figure 4.8: Comparison of TOA (a) RSR and (b) OLR from RRUMS algorithm results (RSR_{R}, OLR_{R}) and revised-GERB data sets (RSR_{G}, OLR_{G}) (3 × 3 SEVIRI pixels along the HALO flight on 26 March 2014. The mean absolute error (MAE), root mean square error (RMSE) and correlation coefficient (CC) are used as metrics.

4.2.1 RTM simulations of TOA irradiance

I illustrate the new method used to derive instantaneous cirrus RF and show that it compares well to observations of RSR and OLR by RRUMS. In particular, a 2-step method is explained to compute both cirrus-free and cirrus influenced TOA irradiances. First, an atmosphere is set up as input to the RTM that contains a realistic representation of the situation observed including in particular all clouds. Then in a second step the ice clouds are removed, for which the RF is to be computed. This provides the cirrus-free reference TOA irradiance for the calculation of cirrus RF. The basic setup of the RTM is described in Chapter 3.4. As is shown in Figure 4.9, every RTM calculation needs an atmospheric state as input. This is the part obtained from ECMWF ERA5 reanalysis data [Hersbach et al., 2020]. All 137 model levels are used. The horizontal and temporal resolution are 0.25°×0.25° and 1 h. The temperature profiles, logarithm of surface pressure, specific humidity, ozone mass mixing ratio, and land or sea mask are derived. Densities of gaseous water (H_2O) and ozone (O_3) are derived from specific humidity and O_3 mass mixing ratio. CO_2 is set to a volume mixing ratio of 400 ppm. Vertical profiles of liquid clouds are also extracted from ERA5 data. I choose vertical profiles close to the HALO flight time, i.e. with a time difference of 30 min at most between model and in situ measurements. This relies on the fact that reanalysis data should provide a realistic description of cloud properties and cloud positions, but I accept that this procedure might cause small temporal shifts such that observations close to cloud edges might not be represented in an optimal way through the model data. However, I refrain from interpolating cloud properties in time since also this procedure would create artificial clouds that do not exist in reality, especially in locations where no cloud is present at a given time but it is there at the next time. For liquid clouds, the parameterization by Bugliaro et al. [2011, 2022] is applied for creating R_{eff} profiles using IWC and temperature from ERA5. The solar zenith angle corresponds to synchronous SEVIRI observations. Besides, the albedo of ocean is parameterized following Cox and Munk [1954a,b] and Nakajima and Tanaka [1983], especially involving the wind speed from ERA5. For ice clouds, another procedure is applied. Since SEVIRI observations with CiPS are able to account for the entire cirrus cloud layers but are only dependent on thermal channels and not affected by low lying clouds [Strandgren et al., 2017b], SEVIRI provides accurate ice cloud properties (IOT) that can be used in the RTM.

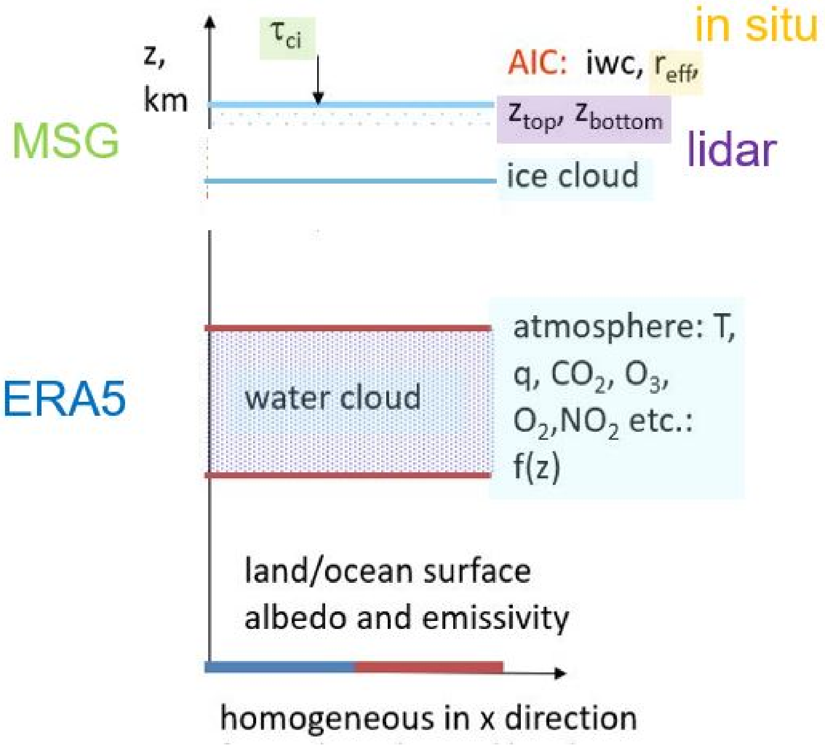
in situ
τ_{ci}
z, km
AIC: iwc, r_{eff},
z_{top}, z_{bottom}
MSG
lidar
ice cloud
atmosphere: T, q, CO_2, O_3, O_2,NO_2 etc.: f(z)
ERA5
water cloud
land/ocean surface albedo and emissivity
homogeneous in x direction

Figure 4.9: Structure of input data in the forward RTM simulations using LibRadtran.

Positions of ice clouds from ML-CIRRUS measurements and CTHs estimated from WALES observations are exploited to collocate the clouds probed by HALO with the SEVIRI observed contrail cirrus and natural cirrus. Satellite observations are functions of both time and space. Since the temporal frequency of in situ observations is 1 Hz, various HALO measurements are located inside each SEVIRI pixel. In general, time series of observations are produced with the original temporal resolution of the given instrument.

Then the representation of cirrus at the flight level is complemented by adding their R_{eff} from in situ measurements, CTH and cirrus bottom height (CBH) from lidar legs, as well as CiPS IOT into libRadtran in the way described in the next lines. This way I simulated a vertically homogeneous ice cloud with the correct IOT obtained by CiPS. It is assumed that IOT is to be constant over an entire SEVIRI pixel while R_{eff} changes according to in situ information (at the altitude levels probed by HALO). Since the RTM needs IWC as input, I determine it from IOT. First, Extinction Ext for IWC = 1 gm^{-3} (i.e. extinction in km^{-1}) for each measurement is interpolated to the given in situ R_{eff} with the parameterisation of optical properties of Baum et al. [2014] for rough aggregates. The selection of this shape for all cloud types is motivated by the fact that each cloud column, even those containing contrails, encompass ice crystals with various temporal evolution, e.g. young small – probably round, ice particles in contrail cores together with larger sedimenting ice crystals in the fall streaks with different shapes or with evaporating ice crystals – in part still large in size, in subsaturated air that are starting to lose asphericity or maybe even natural ice crystals with unknown shape. To avoid an additional arbitrary choice with respect to ice particle shape I decided to keep the method as simple as possible and selected this shape (rough aggregates) as e.g. for the MODIS optical property products Collection 6. A sensitivity study with respect to ice particle shape is conducted in Chapter 4.2.3. Note that the parameterization of this shape only covers R_{eff} from 5 to 60 µm, which results in the inexecutable RTM calculations for larger or smaller ice crystals. 20 cases in total are removed but have a negligible effect on the estimation of radiative effects as R_{eff} of contrail cirrus and natural cirrus always fall in the range where RTM could simulate as indicated in Figure 4.7. The IWC for each measurement of R_{eff} corresponding to a vertically homogeneous ice cloud with given IOT is derived using the following equation:

$$IWC = \frac{IOT}{Ext \times (CTH - CBH)} \tag{4.3}$$

For IWC=1 gm^{-3}, the cloud exhibits an extinction. Subsequently, the theoretical optical thickness OT is expected to be the multiplication of the extinction and the geometrical thickness. To align with the observed IOT, IWC should be scaled down with the ratio of IOT to OT, yielding the real IWC. CTH and CBH are obtained from the lidar legs since they seem to vary only slowly with time and space. Thus, this IWC is used to simulate a homogeneous ice cloud layer between CBH and CTH and corresponds to the IOT observed by CiPS.

Finally, in situ measurements of R_{eff} are assigned to a collocated IOT from CiPS as well as the ERA5 properties listed above for temperature, gas and liquid water clouds. With this atmospheric setup, TOA irradiances are computed and represent the cirrus contaminated RSR and OLR. Then, the ice clouds only are removed from the input of the RTM and other calculations are performed to compute cirrus-free irradiances. Both together are then inserted in Eqs. 2.31-2.33 to compute the instantaneous net RF of the cirrus cloud under consideration.

The RSR and OLR values influenced by cirrus as obtained from libRadtran simulations (RSR_{L} and OLR_{L}) and compared with RRUMS algorithm outputs (RSR_{R} and OLR_{R}) along the flight path of HALO are presented in Figure 4.10. The two methods agree quite well, but the RTM calculations tend to underestimate large RSR values, probably due to too thin, missing or even mismatched liquid water clouds that are taken from ERA5. Uncertainties in ice cloud properties cannot have such a large effect on RSR since their optical thickness is very low around 0.2. Furthermore, a smaller overestimation of

RSR by the RTM compared to RRUMS is also observed for the smallest RSR values below $150\,Wm^{-2}$, related to the bias of estimated ocean albedo but improved by the application of wind speed. For OLR, the agreement between the two data sets is good, with both slight ($< 10\,Wm^{-2}$) overestimations and underestimations.

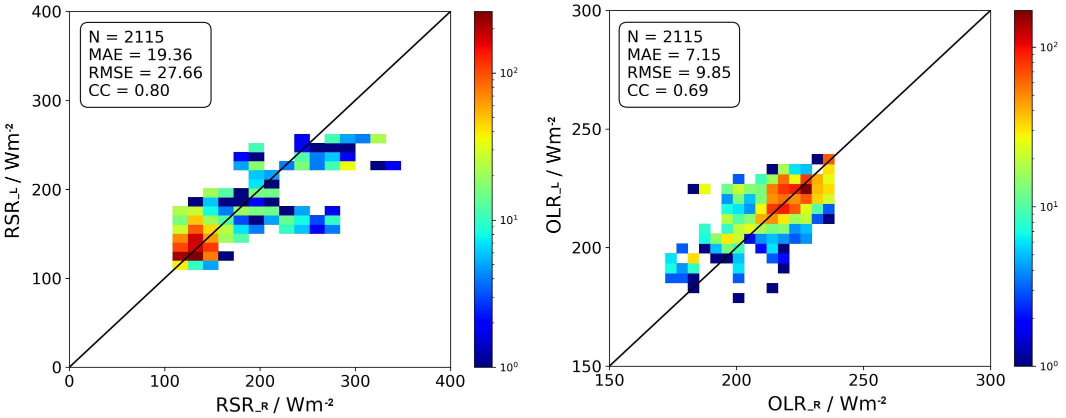

Figure 4.10: Comparison of TOA (a) RSR and (b) OLR from RTM simulations ($RSR_{\_L}$, $OLR_{\_L}$) for probed ice particles and RRUMS algorithm results ($RSR_{\_R}$, $OLR_{\_R}$) for single SEVIRI pixel along the HALO flight on 26 March 2014. The MAE, RMSE and CC are used as metrics.

The RTM based TOA radiation estimation method provides a good representation of the real atmosphere and will be used to determine RF of the ice clouds in the following section.

4.2.2 Diurnal cycle of TOA RF of the contrail cirrus outbreak

In Chapter 4.2.1 TOA RF for each waypoint of the probed cirrus was presented. In order to examine microphysical properties and radiative effects of the contrail cirrus outbreak detected in this area and to analyse the corresponding temporal variation, I present the regional cirrus cover (CC), average cirrus IOT and CTH (all three quantities from CiPS), as well as mean TOA SW, LW and net RF in an area of 36×51 pixels ($16500\,km^2$, the red area in Figure 4.2) near the HALO flight track, characteristic for contrail cirrus and cirrus as shown in Chapter 4.1. This area extends mostly east of the HALO flight and thus contains the contrails or contrail cirrus formed directly east of the ridge cloud. I consider here all ice clouds in the region with high aviation impact.

RF in this section is at the SEVIRI resolution, and calculated using CTH, IOT from CiPS, R_{eff} from in situ mean values of all cirrus (called $R_{eff,mean}$ in the following), and cloud thickness from WALES assuming the latter doesn't change in the area with the same procedure presented in Chapter 4.2.1 based on the RTM libRadtran.

In Figure 4.11a, it is observed that CC gradually decreases from 0.77 at 06 UTC to 0.25 at 14 UTC. The positive vertical velocity from ERA5 around that region implies the local

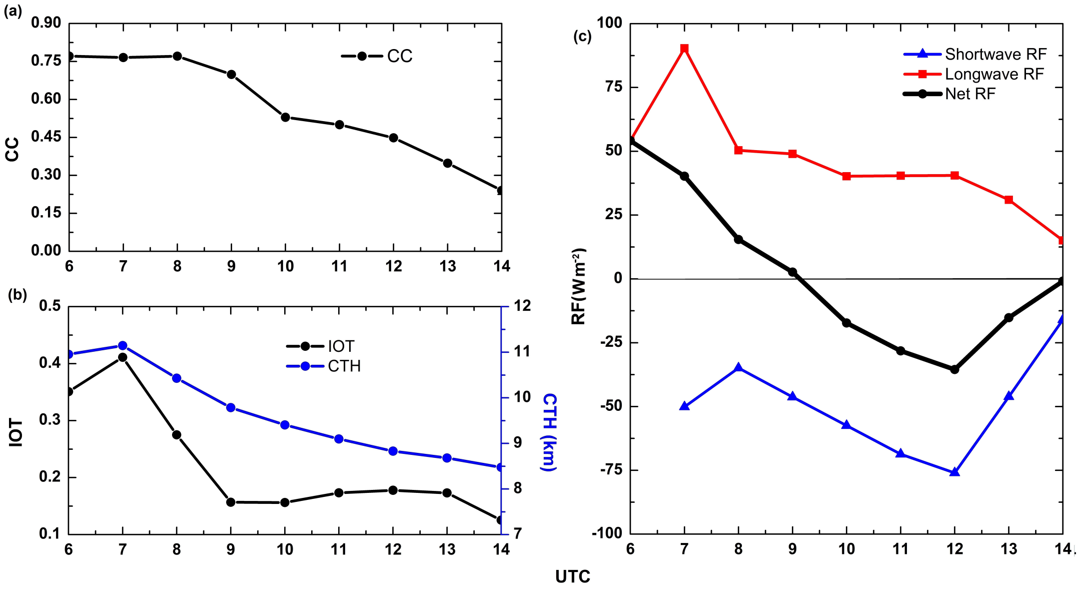

Figure 4.11: The variations of (a) CC, (b) mean IOT and mean CTH, and (d) SW, LW and net RF within the area indicated by a red box in Figure 4.2.

downward motion of airmass to warmer temperature layers and the CTH also decreases. IOT in Figure 4.11b decreases between 07:00 (0.41) and 10:00 UTC (0.15), then slowly increases until 12 UTC (0.17), then falls to 0.12. CTH decreases during the day and is thus consistent with both the observations of HALO and the downward motion. Since an underestimation of CTH by CiPS with respect to WALES (Figure 4.3) is observed there, it is assumed that CTH is also underestimated by CiPS in this area.

Mean net RF over this area in this synoptic situation is positive in the early morning until 9 UTC with the maximum of net RF is at 7 UTC when the sun has risen. Hence the contrail cirrus outbreak is warming during night and early morning hours. After 9 UTC, the forcing becomes negative. More explicitly, from around 9 to 14 UTC the net RF is negative and thus this contrail cirrus outbreak tends to cool during daytime. The strongest cooling is observed at 12 UTC. Notice however that the possible underestimation of CTH by CiPS in this area would result in the general underestimation of the LW RF results since a lower CTH reduces the contrast to the cirrus-free OLR. In turn, this would further shift cirrus net RF towards cooling.

4.2.3 Uncertainty of effective radii and ice crystal shape

To quantify how the estimated uncertainties in R_{eff} (and resulting IWC) as well as assumed crystal shapes influence the radiative forcing, I compute radiative forcing for aggregates (agg) with $R_{eff} = R_{eff,mean} \pm 50\%$ and perform a sensitivity study about ice crystal shape using the general habit mixture (ghm) also available from Baum et al. [2014]. The simulated values are recorded in Table 4.2. The uncertainty of RF due to R_{eff} has an average of $0.2\,Wm^{-2}$ in SW and $0.1\,Wm^{-2}$ in LW. In total the effect on the net RF is approx. $0.1\,Wm^{-2}$. Compared with aggregates, the ghm model has induced a larger net RF of $1.7\,Wm^{-2}$, with the shift in SW and LW of $1.2\,Wm^{-2}$ and $0.5\,Wm^{-2}$, respectively.

Table 4.2: The sensitivity study on how changing the uncertainty of R_{eff} (± 50%) and assumed crystal shapes (aggregates agg and general habit mixture ghm according to Baum et al. [2014]) impact the resulting radiative forcing in Figure 4.7.

UTC/h	SW RF/Wm^{-2}				LW RF/Wm^{-2}				Net RF/Wm^{-2}			
	agg	-50%	+50%	ghm	agg	-50%	+50%	ghm	agg	-50%	+50%	ghm
6					54.1	53.9	54.0	55.1	54.1	53.9	54.0	55.1
7	-50.2	-50.7	-49.8	-47.5	90.4	90.0	90.2	91.3	40.2	39.3	40.4	43.8
8	-34.9	-35.3	-34.7	-33.7	50.4	50.2	50.3	50.8	15.5	14.8	15.6	17.0
9	-46.3	-46.6	-46.1	-44.8	49.0	48.9	48.9	49.5	2.7	2.3	2.8	4.7
10	-57.5	-57.7	-57.3	-56.1	40.2	40.2	40.1	40.6	-17.2	-17.5	-17.2	-15.5
11	-68.7	-68.9	-68.5	-67.6	40.4	40.5	40.3	40.8	-28.2	-28.4	-28.1	-26.8
12	-76.0	-76.2	-75.9	-74.5	40.5	40.6	40.4	40.9	-35.5	-35.6	-35.5	-33.7
13	-46.2	-46.2	-46.0	-45.1	31.0	31.0	30.9	31.2	-15.2	-15.2	-15.1	-13.8
14	-16.0	-16.0	-15.9	-15.4	15.0	15.1	15.0	15.1	-0.9	-0.9	-0.9	-0.3

Chapter 5

Machine learning based improvements of ERA5 humidity predictions

A novel prediction method leveraging dynamic states and machine learning techniques has been developed to enhance atmospheric humidity prediction in current models, with a particular focus on mitigating the wet bias in the lower stratosphere (LS) and dry bias in the upper troposphere (UT). Employing artificial neural networks (ANN), an artificial intelligence approach recognized as a universal approximator for unknown functions (meteorological conditions) and truth values (measured humidity) [Hornik et al., 1989], the objective is to extend this methodology to weather forecast datasets, including those from the European Centre for Medium-Range Weather Forecasts (ECMWF) Integrated Forecast System (IFS) and the German Weather Service. The investigation aims to elaborate how atmospheric states influence the future evolution of humidity, potentially provide corrected humidity and ice supersaturation distributions, and contribute to assessments of contrail cirrus climate impact.

This study aims to advance atmospheric humidity prediction by integrating thermodynamic conditions and dynamical states, aligning with the trajectory of comprehensive, long-term, and accurate airborne water vapor measurements. This approach help to identify and assess parameters with the most significant impact on enhancing forecasts of relative humidity with respect to ice (RHi). In Figure 5.1, a schematic framework illustrates the process of meteorological parameter selection, model training, and model interpretation and evaluation. The initial step involves selecting parameters for model training, which includes collocating ERA5 reanalysis and In-Service Aircraft for Global Observing System (IAGOS) measured atmospheric humidity data. Detailed data descriptions are provided in Chapter 3.2.2 and 3.3. The Spearman correlation coefficient is computed to choose the most suitable parameters, time and pressure levels, considering the temporal and vertical dependence of humidity on thermodynamic conditions and dynamical states. After preparing the training, validation, and test data sets, the second step involves transforming IAGOS RHi to specific humidity using temperature and pressure measurements from IA-

GOS, as IAGOS measures water vapor mixing ratio rather than specific humidity directly. Subsequently, the ANN technique is applied to the training dataset. For the final step, which encompasses model interpretation and evaluation, the study discusses the relative contributions of input variables to the model. The model is validated in both cloud-free and cloudy conditions, spanning the LS and UT regions. A comparison is made with water vapor measurements from the Cirrus in High Latitudes (CIRRUS-HL) research campaign in 2021, and the equitable threat score (ETS), commonly used in weather forecast verification [Wang, 2014], is computed to assess ice supersaturation prediction. The improved humidity is further utilized as input for the radiative transfer model (RTM) to investigate the corrected atmospheric water vapor radiation budget.

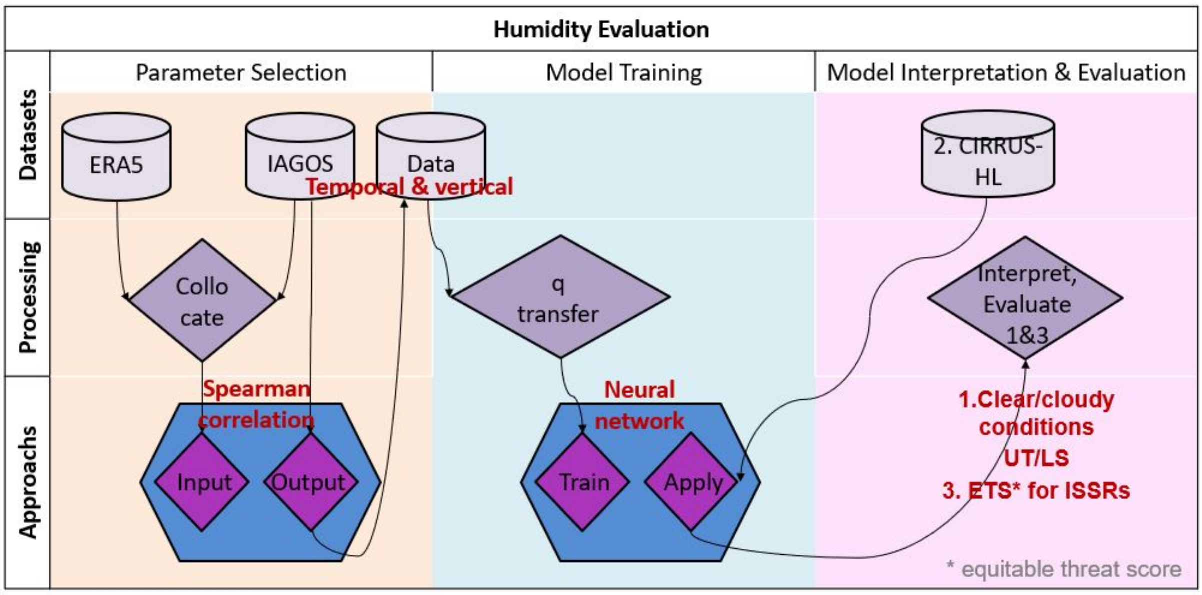
Humidity Evaluation
Parameter Selection
Model Training
Model Interpretation & Evaluation
Datasets
Processing
Approachs
ERA5
IAGOS
Data
Temporal & vertical
2. CIRRUS-HL
Collo cate
q transfer
Interpret, Evaluate 1&3
Spearman correlation
Input
Output
Neural network
Train
Apply
1.Clear/cloudy conditions
UT/LS
3. ETS* for ISSRs
* equitable threat score

Figure 5.1: Schematic framework of meteorological variables selection, humidity prediction model building, and model interpretation and evaluation.

5.1 Preparation for the neural network models

5.1.1 Input and output data collocation

For the training of the ANN model, the accurate humidity measurements provided by IAGOS [Petzold et al., 2015, 2020] are used as the training target. Given that the spatial distribution of humidity is influenced by thermodynamic, dynamical, and cloud microphysical processes, I incorporate thermodynamic conditions and dynamical states with the effects from clouds in ERA5 (Table 5.1). Data measured in 2020 is collected over the Atlantic Ocean on all pressure levels from 400 hPa to 200 hPa and have a vertical resolution of 25 hPa (200 hPa-250 hPa) and 50 hPa (250 hPa-400 hPa). The latitude and longitude span from 80°N to 0 and from 30°W to 50°E. The ERA5 data offer a temporal resolution of 1 h and a spatial resolution of 0.05°.

ERA5 time and layers that best match the IAGOS measurements were determined, and ERA5 variables between 400 hPa and 200 hPa were preprocessed to align with the IAGOS humidity and temperature data sets. In addition, RHi in the UTLS is subject to vertical air motions such as stratospheric intrusions or uplift of tropospheric air masses in convection or frontal systems as well as horizontal airmass transport. Therefore, thermodynamic conditions and dynamical states from ERA5 are linked to RHi at the IAGOS data acquisition time and location by considering a time span of 24 hours prior, with one-hour intervals, and examining two pressure levels above and two pressure levels below the IAGOS data acquisition location. The ERA5 variables are subjected to linear interpolation to align with the vertical position of the IAGOS data acquisition location, specifically adapting to pressure levels. The ERA5 data maintains its original temporal and spatial resolution, whereas the water vapor values and atmospheric conditions measured by IAGOS with four second temporal resolution, spanning a range of 10 to 400 data points within a single ERA5 grid box, are subjected to averaging. This collocation between model meteorological variables and measured humidity values in the year 2020 contains 1.25 million samples, which is used to train the ANNs. This copes with enormous variability and sharp gradients in the humidity fields, and can help to estimate a realistic full pattern for humidity measurements comparison and model application.

Table 5.1: Overview of the variables used in this study. Spatial resolution of ERA5: 0.05°. Vertical resolution of ERA5 on pressure levels: 25 or 50 hPa. Temporal resolution of ERA5 and IAGOS: 1 h and 4 s. Study region: Atlantic Ocean.

source	variable	description	unit
ERA5 on pressure levels	T	air temperature	K
	ciwc	specific cloud ice water content	kg/kg
	RHi	relative humidity (ice)	%
	q	specific humidity	kg/kg
	z	geopotential	m^2/s^2
	w	vertical velocity	Pa/s
	d	divergency of wind	s^{-1}
	u	U component of wind	m/s
	v	V component of wind	m/s
	vo	relative vorticity	s^{-1}
	pv	potential vorticity	$Km^2kg^{-1}s^{-1}$
	time	hour	1
	level	pressure	hPa
IAGOS	RHI_P1	relative humidity (ice)	1
	air_temp_P1	air temperature	K
	air_press	air pressure	Pa

5.1.2 Evaluation of temperature and RHi from ERA5 in the UTLS

The aim of this section is to firstly compare and quantify the difference of RHi between the ERA5 reanalysis data and the in situ measurements provided by IAGOS. According to the physical definitions of ISSRs in Chapter 2.3.1, RHi depends on temperature and available water vapor. Simmons et al. [2014] pointed out the temperature bias of ERA-Interim reanalysis, the precursor of ERA5 data, near the tropopause in the tropics. In a first step, IAGOS observations are used to evaluate the ERA5 temperature data sets. Given the frequently neglected ice supersaturation within cirrus clouds due to the application of saturation adjustment in cirrus parameterizations within numerical weather prediction (NWP) [McDonald, 1963], this evaluation is performed not only within the UTLS region but also over the cloud-free and cloudy conditions. Cloud-free and cloudy scenarios are discerned based on the presence of the ciwc greater than zero, while distinguishing between the LS and the UT is upon the threshold of potential vorticity pv exceeding 2 PVU.

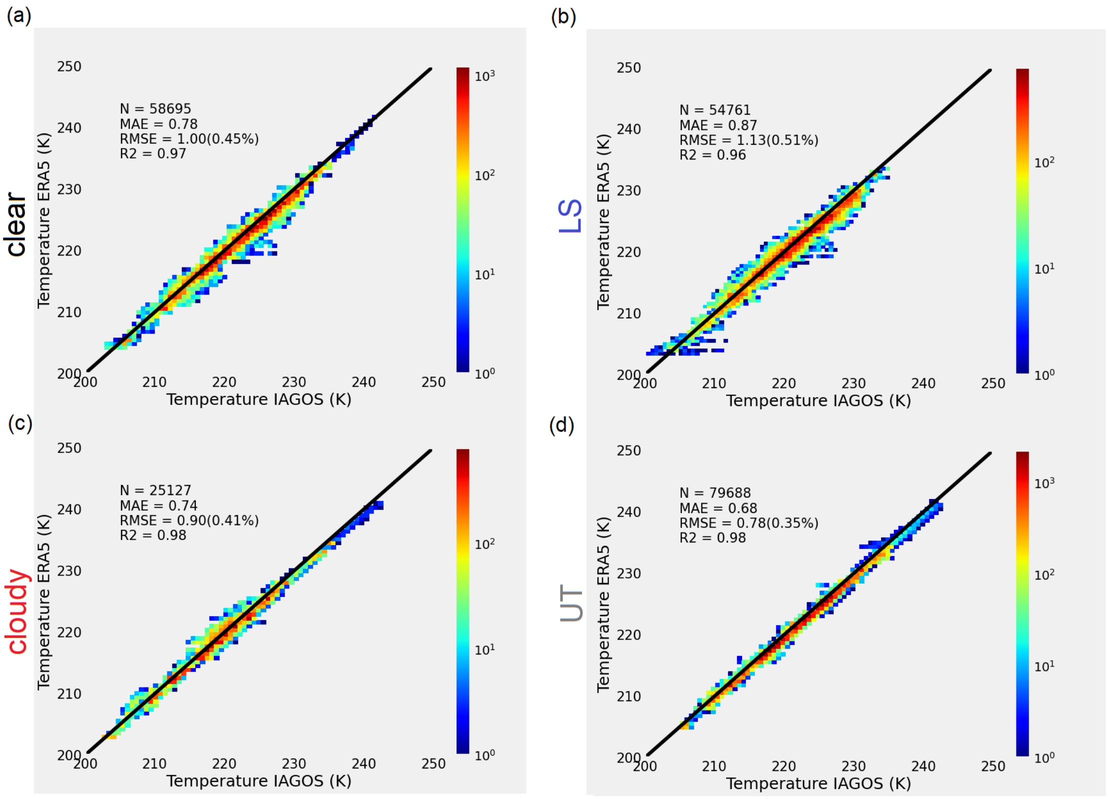

Figure 5.2: Comparisons of temperature in (a) clear, (b) LS, (c) cloudy, and (d) UT from ERA5 and IAGOS.

Figure 5.2 shows the comparison between the temperature of the IAGOS observations and the ERA5 data for all collected IAGOS waypoints in Chapter 5.1.1 around the cruise altitudes (200 hPa-400 hPa) over the North Atlantic region (NAR) in 2020. The good agreement between both temperatures is reflected in all tested cloud-free, cloudy, LS and UT scenarios by the high correlation coefficient (R2 of 0.96 - 0.98). The spread of the correlation corresponds to a larger variability in the IAGOS temperature measurements when the aircraft flew through clouds, or from the interpolation of the gridded ERA5 temperature to the vertical position of aircraft. The MAE between the temperature of the IAGOS measurements and ERA5 varies between 0.68 K and 0.87 K, with the RMSE of 0.78 K (0.35%) - 1.13 K (0.51%) over the entire data sets. The ERA5 temperature has a relatively more obvious cold bias in the cloud-free and LS region in Figure 5.2, with the largest MAE and RMSE values among these four scenarios.

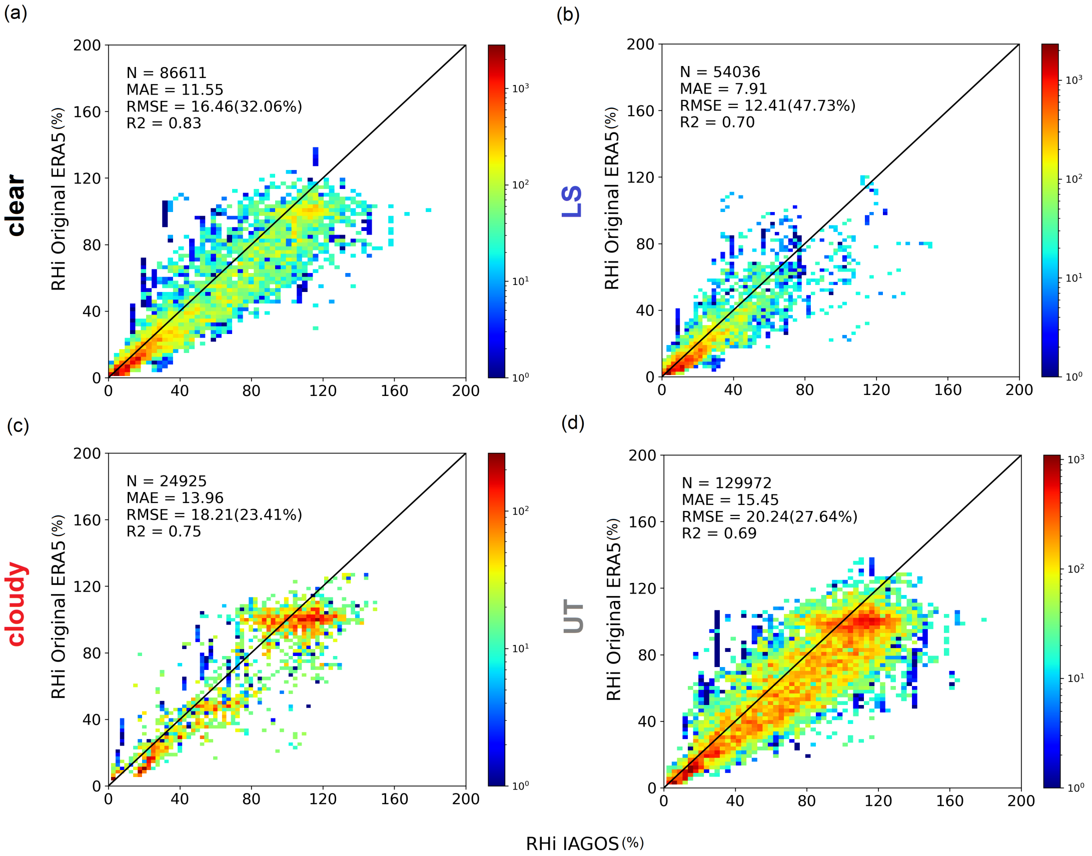

Figure 5.3: Comparisons of RHi from ERA5 data against IAGOS measurements in (a) clear, (b) LS, (c) cloudy, and (d) UT between 200hPa and 400 hPa over the Atlantic for the year 2020.

In Figure 5.3, the comparison of RHi from ERA5 data and IAGOS measurements is depicted. The ERA5 RHi shows a trend to be underestimated if compared with IAGOS RHi. In the clear and LS regions, the RMSE are 16.46% and 12.41%, respectively. The dry bias in RHi is more significant in cloudy and UT regions, with respective RMSE of

18.21% and 20.24%. This discrepancy is likely attributed to water absorption during the ice particle growth processes within cloudy regimes. As mentioned in the beginning of this section, RHi depends on both temperature and available water vapor. ERA5 typically underestimates specific humidity, and the cold bias in cloud-free and LS regions offsets the dry bias of RHi, as demonstrated in the study by Kaufmann et al. [2018]. In contrast, a dry bias persists in cirrus and the UT. This evaluation serves as the motivation behind this thesis, aiming to enhance humidity prediction for weather forecasts.

5.1.3 Correlating model meteorological variables with measured water vapor

What meteorological conditions and at which time and pressure level should be chosen for training the specific humidity and RHi prediction model using ANN? To answer this question, the dependence of measured RHi at the time and location of IAGOS data acquisition on ERA5 meteorological variables at the preceding time and pressure levels nearby is determined through the calculation of the Spearman's correlation coefficient r_s:

$$r_s = \frac{cov(u, v)}{\sigma_u \sigma_v} \tag{5.1}$$

where $cov(u, v)$ is the covariance of the variables u and v, and σ_u and σ_v are their standard deviations. The correlation is shown in Figure 5.4 between IAGOS RHi and different ERA5 variables sampled at the time of IAGOS measurements (time lag = 0) or at previous times (time lag between -24 and -1 h). This correlation combines not only RHi larger than 80% to investigate ISSRs but also the full range of RHi to provide sufficient data for model building in the Chapter 5.2.

In Figure 5.4, significant correlations are observed among various thermodynamic factors, specifically RHi (blue), and temperature (T, green), obtained from ERA5 data before the time of IAGOS data acquisition, and the corresponding IAGOS RHi values. Notably, ERA5 RHi and T demonstrate the positive and negative correlations in predicting IAGOS RHi, respectively. These observed relationships can be explained by established physical laws in Chapter 2.3.1. That is, RHi is the ratio of the partial vapor pressure of water vapor and the saturation vapor pressure with respect to ice, and according to the Clausius-Clapeyron equation, the latter vapor pressure is positively associated with T. Furthermore, as the time lag decreases, the correlation of RHi increases from 0.3 to 0.5, indicating that humidity values closer in time exert the most significant influence on the current humidity state. For T, it is approximately 0.5, which is statistically most significant and somewhat expected. The shadow surrounding the solid line represents the uncertainty associated with these correlations. ciwc is not represented in this plot due to the absence of data for cloud-free regions.

However, the correlations between ERA5 dynamical states and IAGOS RHi, with varying time lags, exhibit temporal fluctuations. The positive relationship between ERA5 geopotential (z) and IAGOS RHi is in accordance with the findings of Wilhelm et al.

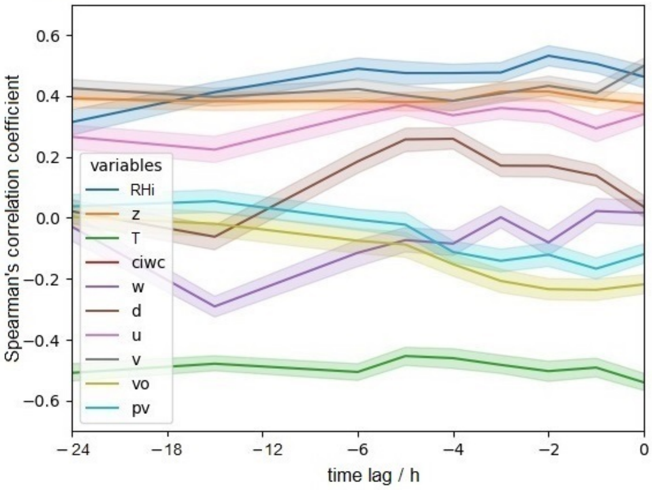

Figure 5.4: Temporal dependence of the target RHi from IAGOS on the selected thermodynamic and dynamical variables from ERA5 pressure level data between 200hPa and 400 hPa over the Atlantic for the year 2020. x axis: time lag between ERA5 and IAGOS/h; y axis: Spearman's correlation coefficient.

[2022], which highlight that persistent contrails with high RF tend to occur at elevated z values, in other words, higher altitudes. The correlation for z stands at approximately 0.4. In addition, parameters such as vertical velocity (w), divergence (d), horizontal wind speed components (u and v), relative vorticity (vo), and potential vorticity (pv) all interact with IAGOS RHi differently over time. w consistently demonstrates negative correlations, with absolute values increasing between the 24-hour and 16-hour time lags before gradually declining. The correlation for u tends to increment slightly, ranging from 0.2 to 0.3, while that for v shows a tendency to decrease, fluctuating between 0.4 and 0.3. d generally exhibits positive correlations, with the highest value occurring around the 4-hour to 5-hour time lag. In contrast, vo persists in negative correlations, with a correlation coefficient tending to -0.2 in relation to ERA5 values for IAGOS RHi. pv maintains an oscillating pattern around zero, shifting from positive to negative values. In general, z, v, w, d, and u exert the most significant influences on the current humidity state.

Regarding the vertical dimension, the effects of thermodynamic and dynamical conditions from ERA5 on the IAGOS RHi as a function of vertical pressure layer differences are also calculated. While RHi remains influential, the impacts of T and z almost diminish. Conversely, the influences of w and d remain prominent, while the influences of horizontal wind speed component u and v, and pv approach zero.

These findings suggest the potential to improve atmospheric humidity prediction by considering not only traditional thermodynamic variables but also dynamical proxies and their evolution. To keep a balance between information richness and modeling efficiency, combining ERA5 data with IAGOS humidity fields involves a 6-hour time lag and a 2-

pressure layer difference.

Fisher Z-transformation is calculated here to approximately find the confidence intervals for the Spearman correlation coefficient r_s to understand if the empirically found r_s is significant. Three steps are included in the significance test. Firstly, the Fisher transformation is performed with Eq. 5.2.

$$z_r = \frac{1}{2} \ln \frac{1 + r_s}{1 - r_s} \tag{5.2}$$

It turns out that the sampling distribution of z_r follows a normal distribution. In the second step, log upper and lower bounds of the 95% confidence interval for meteorological conditions are found using Eqs. 5.3 - 5.4.

$$L = z_r - \frac{z_{1-\alpha/2}}{\sqrt{n-3}} \tag{5.3}$$

$$U = z_r + \frac{z_{1-\alpha/2}}{\sqrt{n-3}} \tag{5.4}$$

Thirdly, the confidence interval is found with Eq. 5.5.

$$confidence\ interval = \left[\frac{e^{2L}-1}{e^{2L}+1}, \frac{e^{2U}-1}{e^{2U}+1}\right] \tag{5.5}$$

The relationship between w and RHi at 5 h before and that between pv and RHi at 1 h and 3 h before are not significant as zero is within the confidence interval. Hence pv is typically insignificant and subsequently excluded from the input data sets during the further training of the ANN model. Other meteorological conditions are significant for their relationships with measured humidity at the IAGOS data acquisition time and location.

5.1.4 Training and validation data

Considering the confidence interval calculations in the previous section and accounting for the typical lifespans of water vapor transport mechanisms, including deep convection, warm conveyor belt uplift regimes, and slow ascending flows, the criteria for data combination involve a 2-hour and 6-hour time lag prior to IAGOS data acquisition, ±2 pressure layers from ERA5, and the current humidity measurements from IAGOS. Following this, a dataset comprising 8928571 samples is compiled for training, validation and testing , including the temporal evolution of meteorological quantities.

To ensure model robustness, 10% of the samples are randomly excluded from the training set to construct an independent test data set. The remaining training sets of the ANN model, with RHi and specific humidity q as two outputs, are further subdivided into an 80% training subset and a 10% test subset, respectively. While the primary focus is on improving predictions of higher RHi values and ISSRs, the complete range of RHi values is supplied to the neural networks to enhance the model's overall accuracy.

Distributions of the input and target values in the training data sets are sketched in Figure 5.5. Notably, they are not uniformly distributed due to the performed selections as

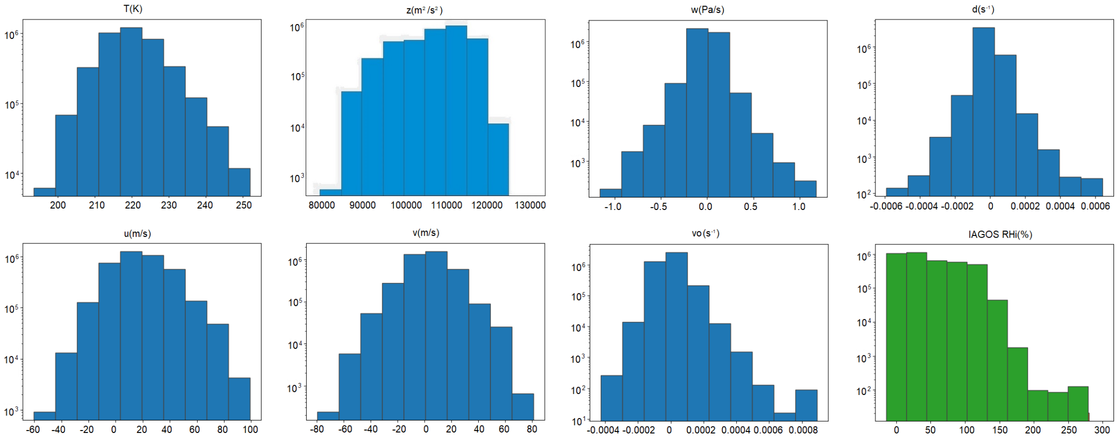

Figure 5.5: Distributions of input variables including T (K), z (m^2/s^2), w (Pa/s), d (s^{-1}), u (m/s), v (m/s), vo (s^{-1}) from ERA5 and target RHi (%) from IAGOS in the ANN model.

well as the usage of different weather conditions. The temperature spans a range from approximately 193 K to 252 K, while the geopotential z encompasses values between roughly 8000 m^2/s^2 and 12500 m^2/s^2. RHi values vary across the entire spectrum, ranging from 0 % to 275 %.

For the derivation of specific humidity (q), the saturation water vapor pressure over ice, p_{ice}, was first calculated using the equation in Murphy and Koop [2005]:

$$p_{ice} = \exp(9.550426 - 5723.265/T + 3.53968 \ln T - 0.00728332\, T) \tag{5.6}$$

T is the air temperature from IAGOS measurements. An earlier comparison between difference parameterizations of p_{ice} showed that the differences in p_{ice} is less than 0.5% for temperatures greater than 173.15 K [Schumann, 2012]. In the next step, q is calculated from RHi according to

$$q = \frac{RHi \times p_{ice} \times R_0}{p \times R_1} \tag{5.7}$$

where p is the pressure altitude (Pa), R_0 (287.05 $Jkg^{-1}K^{-1}$) and R_1 (461.51 $Jkg^{-1}K^{-1}$) are the real gas constants for air and water vapor respectively.

5.2 Model training

Hence, the ANN model is trained with a large set of atmospheric states , including both current and historical states, obtained from reanalysis, as well as humidity measured from instruments aboard aircraft. The former data sets are derived by solving the primitive equations of motion in numerical models. The latter data sets are built by combining the large scale and long term aircraft measurements. An ANN learns to reproduce the statistical relationships between a series of weather conditions , incorporating their temporal evolution, and humidity fields. It iteratively adjusts its parameters until it achieves accurate predictions for the training targets.

The goal is to propose a model capable of learning relationships between current and historical weather conditions and current measured humidity. The aim is to ensure the model performs effectively under normal conditions and produce accurate humidity predictions, thereby mitigating existing bias in the UTLS (see Chapter 5.1.2). A main advantage of the technique is that it involves dynamic processes of water vapor vertical and horizontal transport, and takes advantages of numerous measurements (as references). Our implementation is based on the open-source platform TensorFlow downloaded from TensorFlow 2. The required software packages are Python3.7, Keras, and Scikit-learn.

The software is adapted as follows:

1. Read, normalize, and apply a Gaussian noise with a standard deviation of 0.1 to the input layer. The input variables, which include humidity, temperature (T), geopotential (z in m^2/s^2), vertical velocity (w in Pa/s), divergence (d in s^{-1}), eastward wind speed (u in m/s), northward wind speed (v in m/s), and relative vorticity (vo in s^{-1}) from ERA5, are collected at the time of IAGOS data acquisition, as well as at 2 hours and 6 hours prior, incorporating the temporal evolution of the quantities. Additionally, variables from ±2 ERA5 pressure layers and the target humidity from IAGOS are included, as detailed in Chapter 5.1.4.

2. Establish an ANN with 56 inputs, 100 hidden neurons for 2 hidden layers and 2 outputs. For details about the ANN different layers please refer to Chapter 2.4.1. Set relu as an activation function for hidden layers, while using a linear function for the output layer.

3. Utilize MSE as a loss function. Compile the ANN model with learning rate = 0.001, decay = 10^{-5} and momentum = 0.99.

4. Fit (Train) the ANN model with batch sizes of 1024 and 2000 iterations (epochs) at approximately 17 bits/s.

5. Disable the normalization of humidity predictions.

6. Convert the output data to the NetCDF4 format using NetCDF operators.

The ANN is described in Chapter 2.4 in detail. The trained model is validated against the extra test data sets of ERA5 and IAGOS which were not part of the initial training in Chapter 5.4. Finally, the model is applied to dynamically correct the humidity bias in the UTLS region.

5.3 Interpretation of the humidity prediction model

The network output is remapped back for the model interpretation and the investigation of the relative contributions of input variables to the predicted RHi and q. K_x is the relative change in loss when one feature of ERA5 is set to zero for the complete input data set but the rest of the input features is kept unchanged:

$$K_x = \frac{L_x - L_0}{L_0} \tag{5.8}$$

where L_x is the accuracy of the model with the ratio of relative change of MSE (when the ERA5 feature is adjusted) to the original MSE of the ANN model, and L_0 is the basic accuracy of the model. Low values of K_x indicate a small impact of the change on the input quantities, or vice versa.

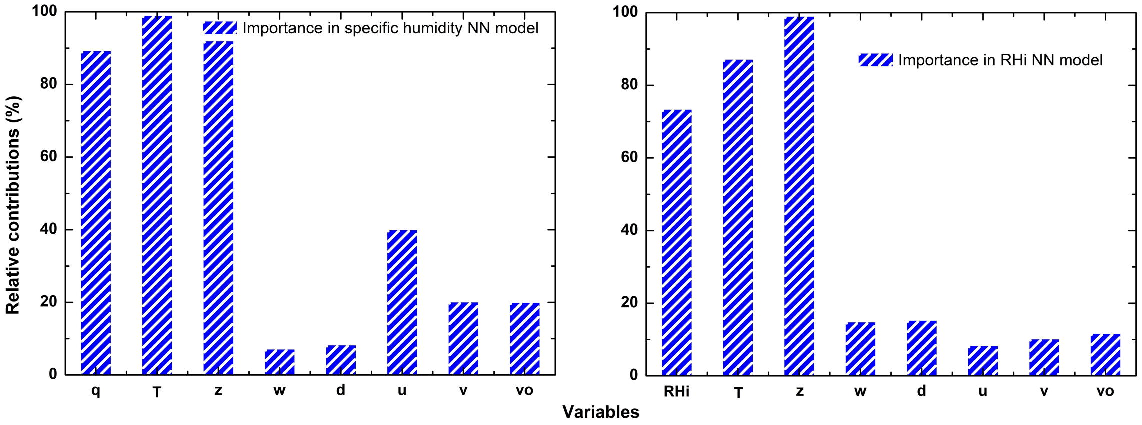

Figure 5.6: Relative contributions of multiple variables to the ANN model for predicting specific humidity and RHi.

Figure 5.6 shows K_x of the input variables for the ANN-based specific humidity and RHi prediction models. Qualitatively, importances of meteorological conditions for both humidity predictions show similar patterns. For example, both plots indicate temperature T and geopotential z to be the most important parameters, and furthermore either q or RHi has a large weight. For the prediction of specific humidity, horizontal wind speed u and v and relative vorticity vo are most prominent among all dynamical states. For the prediction of RHi, K_x however highlights vertical velocity w and divergency d. In general, for the RHi ANN model, the contrast in contributions is not markedly large among the variables of dynamical states.

The significant importances attributed to thermodynamic conditions are explained by the inherent relationship wherein humidity typically rises with temperature, and ice formation increases in regions where water vapor can effectively deposit. The geopotential z seems be best suited for an improved prediction of humidity. Higher humidity density is more concentrated to the high values of z than that in general; they are specifically found on the upper pressure levels. The physical explanation of the relation between ISSRs and high geopotential height can be seen in Wilhelm et al. [2022].

From the aspects of other dynamical states (see Chapter 2.3.4), the importance of vertical motion can be explained by the formation mechanism of ISSRs, which are typically formed when air masses move upwards, adiabatic cooling leads to an increase of humidity [Gierens et al., 2020]. A relatively strong divergence with high horizontal wind speed, and large negative values of vorticity in anticyclonic systems are typical for ISSRs [Wilhelm et al., 2022].

Notably, some variables, such as vertical velocity and divergency, yield strong correlation with RHi in Figure 5.4, their importance in model interpretation is not considerable. This could be attributed to the network configuration. The developed ANN model comprises two hidden layers, with the primary influence stemming from the input variables on the first hidden layer. While w and d demonstrate a robust correlation with RHi, the ANN model might already capture the RHi measured by IAGOS effectively using ERA5 RHi, temperature and geopotential. Consequently, the contribution of other variables to the ANN model interpretation appears reduced.

5.4 Evaluation of the humidity prediction model

5.4.1 Validation in cloud-free and cloudy, lower stratosphere and upper troposphere

The study aims to assess the capability of an ANN model to resolve biases inherent in NWP parameterizations evaluated in Chapter 5.1.2 and elucidate the underlying meteorological conditions in UTLS governing ISSRs. Furthermore, considering the predominant presence of ice supersaturation in the UT as opposed to the LS, this study seeks to investigate whether the improved humidity data set exhibits reasonable patterns of ice supersaturation distribution. To quantify the accuracy of the ANN model, RHi and q are predicted for test data set and evaluated under four conditions: cloud-free (clear), cloudy, LS and UT (Figure 5.7, Figure 5.8 and Figure 5.9).

Compared with humidity data from ERA5, the q and RHi predicted from the ANN model are better comparable with measurements from IAGOS. The outputs of the ANN model achieve higher correlations with IAGOS humidity fields ($R2 \geq 0.75$ w.r.t. q; $R2 \geq 0.94$ w.r.t. RHi) and exhibit decreased biases ($RMSE \leq 0.09\,\mathrm{g/kg}$ w.r.t. q; $RMSE \leq 8.92\%$ w.r.t. RHi) for all scenarios when evaluated on their test data set (see Figure 5.7 and Figure 5.8). Having been trained on an independent dataset, the ANN model successfully learns physical patterns and interconnections within the data, evident in its accurate humidity predictions. Notably, the humidity estimates in both cloud-free and LS regions exhibit a closer alignment with the IAGOS dataset, resembling the pattern observed in ERA5. However, discernible biases persist in cloudy and UT regions. In the LS and UT area, the bias is largely reduced for q, with an increase of correlation by 0.21/0.12 and a decrease of MAE by 0.01 g/kg / 0.03 g/kg (see Figure 5.7). The corresponding improvements of RHi prediction are proved with the increase of correlation by 0.24/0.25, and the decrease of MAE by 4.08% / 9.01% (see Figure 5.8). The observed dry bias compared to IAGOS data at the tropopause where the ISSRs are evident can be attributed to the stratosphere-troposphere exchange during which process dry air from the stratosphere is transited to the troposphere. Introducing dynamical states, the prediction accuracy at the tropopause was significantly improved. In the cloudy (cloud-free) regimes, the increase of correlation is relatively small, with the values of 0.08 (0.11) and 0.19 (0.14) for specific humidity and RHi, respectively, and the decrease of MAE is 0.03 g/kg (0.02 g/kg) and 7.6% (6.62%).

The assessment of q compared to IAGOS measurements reveals a noticeably higher dispersion concerning the results with respect to RHi in both ERA5 and the ANN model predictions. This increased uncertainty can be probably attributed to biases arising from the transition process between RHi and q. The presence of 'vertical points' in each plot, deviating from the regression line, signifies limited data points and infrequent measurements under extreme conditions. This, in turn, contributes to the abnormal values in these instances.

In Figure 5.9a, the mean bias percentage error (MBPE) of ERA5 q compared with IAGOS measurements is always negative. In general, as the q values reach 1 g/kg, the underestimation of the MBPE decreases from 25% to 10%. However, beyond this point, the bias exhibits an upward trend, reaching up to 20% when q reaches 2 g/kg, except for the statistics in LS (represented by the blue line). The accuracy of ERA5 q exhibits a notable decline in less humid regions (i.e., $q < 1$ g/kg), particularly in the LS when compared to the UT (as indicated by the grey line). In Figure 5.9b, the ANN model enhances the accuracy of q predictions, primarily exhibiting a minor overestimation for lower water vapor concentration. However, notable exceptions to this trend include a significant underestimation in LS and a dry bias when humidity levels exceed 1 g/kg. Regarding the evaluation of RHi data sets, an increasingly dry bias of ERA5 RHi is found in Figure 5.9c. In contrast in Figure 5.9d, the RHi prediction from the ANN model shows a better agreement with IAGOS measured values, which is similar with that from the q prediction. The dry bias becomes smaller in the UT compared to that in the LS in larger ice supersaturation (RHi > 120%), where the impact of troposphere-stratosphere exchange is exhibited. This humidity evaluation using predicted q and RHi and corresponding ERA5 values shows a distinct improvement from the predicted values from the ANN model compared to ERA5 data set, especially in the ISSRs. This also provides evidence that the improvements in humidity and ISSRs predictions are crucial, with the aim of advancing further simulations of contrail cirrus life cycles and accessing their climate impact.

5.4.2 Validation against CIRRUS-HL measurements

The AIMS (Atmospheric Ionization Mass Spectrometer) water vapor measurement instrument has been evaluated and shown a good agreement with other high quality water vapor instruments [Kaufmann et al., 2018]. Therefore, in addition to the IAGOS measurements, this study uses the independent humidity data records from the AIMS instrument [Kauf-

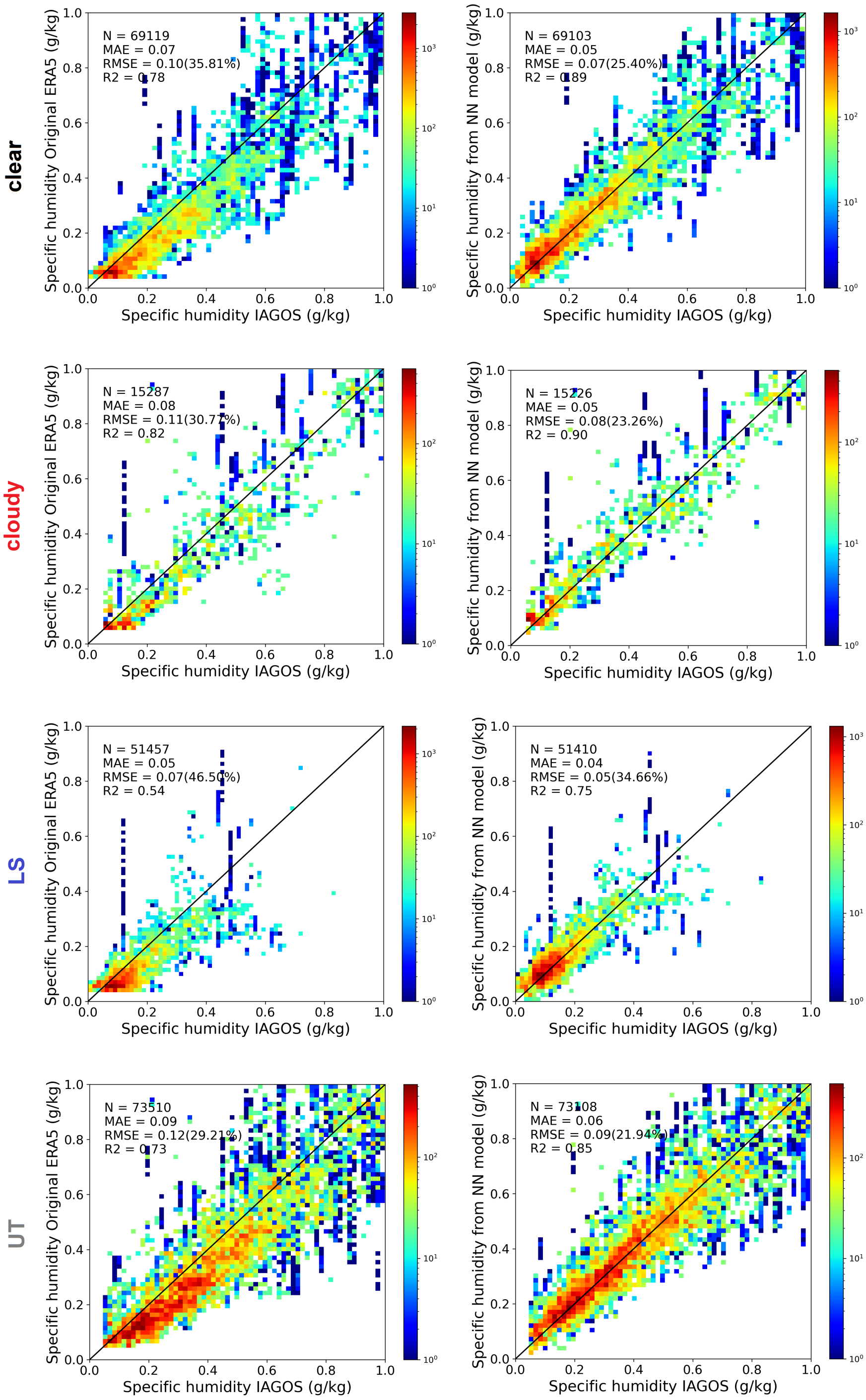

Figure 5.7: Overall test of specific humidity in clear, cloudy, LS and UT from ERA5 and the ANN model.

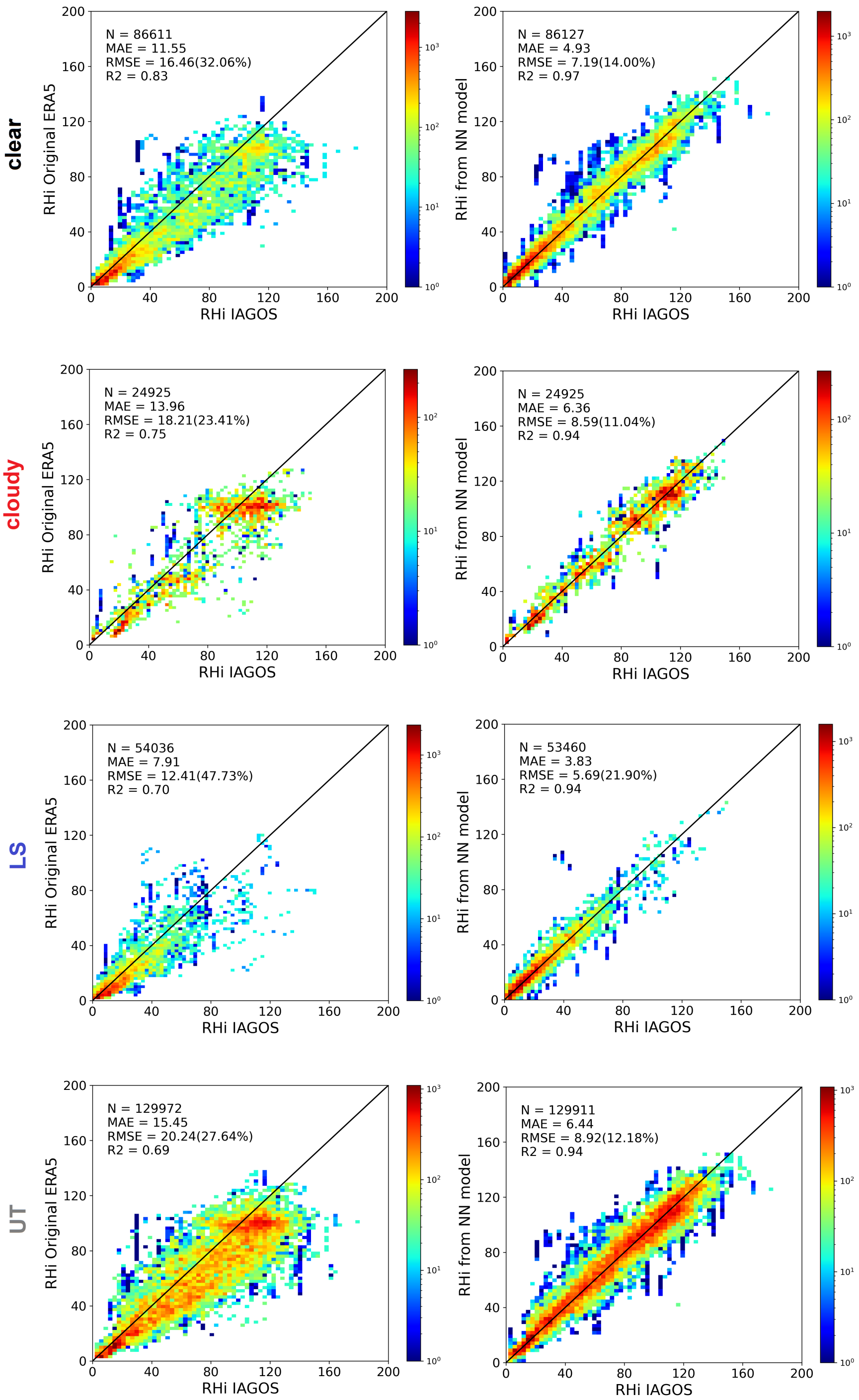

Figure 5.8: Overall test of RHi in clear, cloudy, LS and UT from ERA5 and the ANN model.

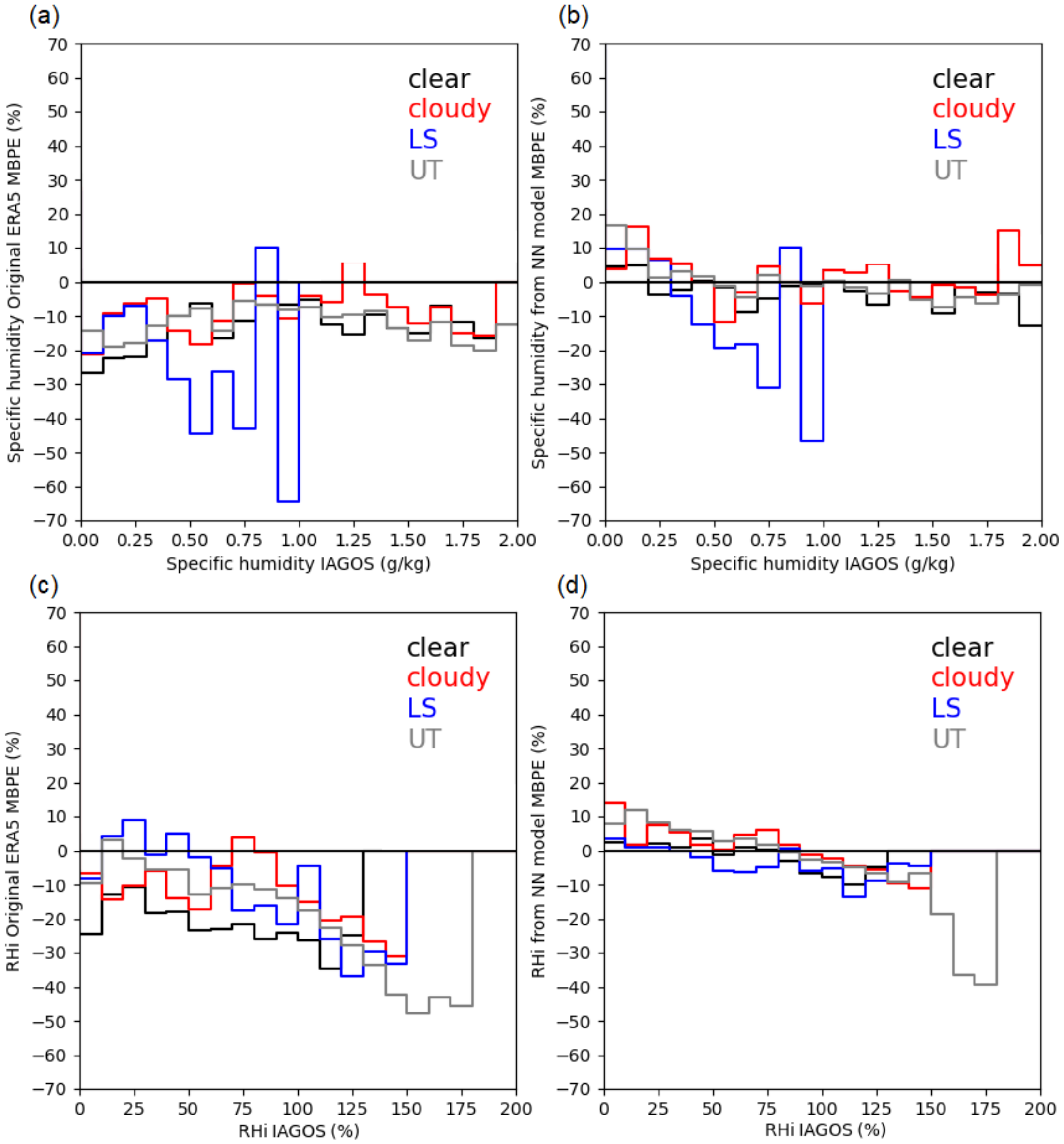

Figure 5.9: Overall accuracy of specific humidity and RHi against IAGOS measurements in clear, cloudy, LS and UT from ERA5 and the ANN model.

mann et al., 2016] aboard the HALO aircraft in special weather situations during the CIRRUS-HL campaign to validate the accuracy of RHi prediction from the ANN model.

On 21 July 2021, HALO departed from Germany in the early morning and detected one strong contrail case over the Iberian Peninsula at cruise level. Figure 5.10a and c present RHi from ERA5 and from the ANN model along the HALO flight track from 07:49 UTC to 08:17 UTC within the pressure levels from 161 to 262 hPa. Compared with AIMS measured RHi, the wet bias of ERA5 data can reach up to 40% (reddish points) in Figure 5.10b. In contrast, the ANN model can reduce the RHi overestimation in the UTLS region within the range of ± 10% (cyan or green points in Figure 5.10d).

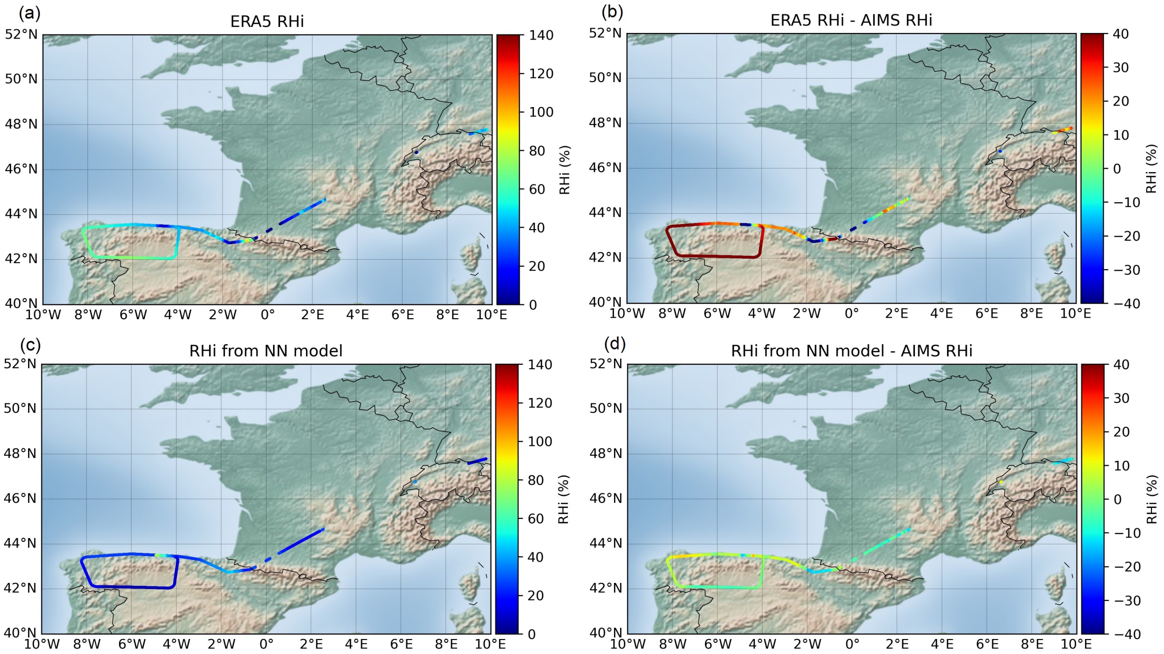

Figure 5.10: RHi derived from (a) ERA5 or (c) the ANN model and the differences relative to AIMS measurements in (b) and (d) obtained from the HALO aircraft on 21 July 2021 during the CIRRUS-HL campaign.

5.4.3 Skill of ISSR prediction against IAGOS data

The ISSRs ($RHi \geq 100\%$) prediction is also evaluated based on the 2×2 contingency table shown in Figure 5.11 and the equitable threat score (ETS) calculated with Eqs. 5.9 - 5.10. The ETS values measure the forecasting skill relative to chance and is often used in the verification of weather forecasts [Wang, 2014].

The table and the variables are defined here. Hits (a): occasions where both prediction and observation show supersaturation. False negative (b): occasions where the RHi observation is larger than 100% and prediction is smaller than 100%. False alarms (c): occasions where RHi prediction is above 100% whereas observation is below this threshold. No forecasts (d): occasions where both prediction and observation show subsaturation. The auxiliary quantity r is the expected number of correct predictions in the random predictions where prediction occurrence/non-occurrence is independent from observation/non-observation:

$$r = \frac{(a+b)(a+c)}{(a+b+c+d)} \; . \tag{5.9}$$

The ETS value is then computed as

$$ETS = \frac{a-r}{(a+b+c-r)} \; . \tag{5.10}$$

The ETS should get larger when the ISSRs prediction is improved. An ETS = 1 indicates all the in-situ IAGOS measurements match up with the ERA5. ETS = 0 means a completely random relation between IAGOS and ERA5 while ETS = -1 implies the reverse relation.

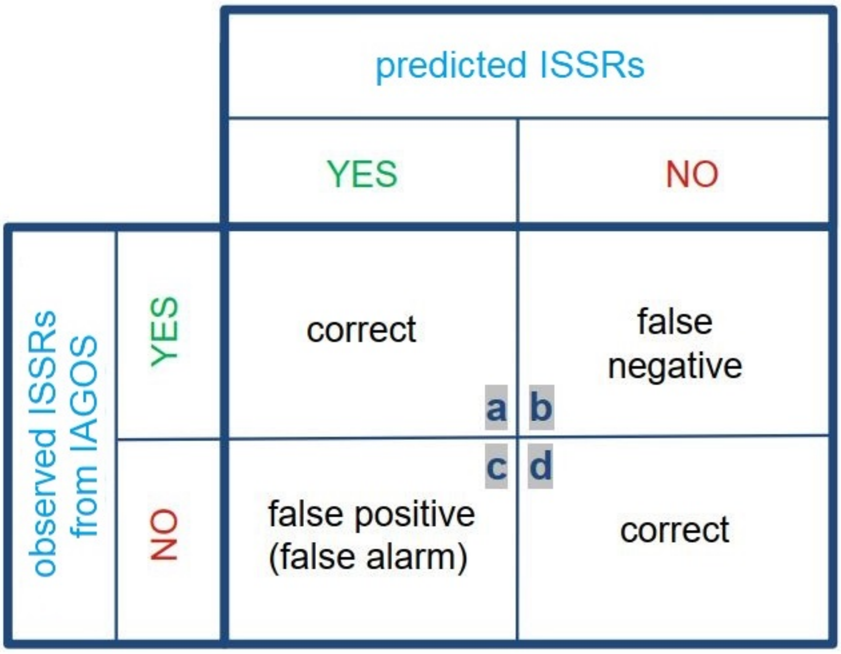

Figure 5.11: The contingency table used for the evaluation of ISSRs prediction.

Table 5.2 records ETS values for both ERA5 ISSRs and the ISSRs predicted by the ANN model. The scores for ERA5 ISSRs in cloud-free, cloudy, LS and UT regions are 0.05, 0.25, 0.14 and 0.22, respectively. The ability for ERA5 to predict ISSRs is limited, particularly in the clear and LS area. The ANN model improves the prediction of ISSRs to reach up to 0.65, with the increase of the score about 0.4.

Table 5.2: Recorded ETS values for the prediction of ISSRs from ERA5 and the ANN model between 200hPa and 400 hPa over the Atlantic in 2020.

Scenarios	ERA5 ISSRs	ANN ISSRs
Cloud-free	0.05	0.45
Cloudy	0.25	0.65
LS	0.14	0.65
UT	0.22	0.64

5.5 Investigation of the corrected atmospheric radiation budget

Atmospheric water vapor, an important climate data record [Hegglin et al., 2014], plays an important role in the radiation budget at TOA [Riese et al., 2012] and also exerts a strong RF affecting temperatures both locally [Forster and Shine, 1999] and at Earth's surface [Manabe and Strickler, 1964]. Figure 2.7 illustrates that the radiative effects of water vapor in the UTLS are very sensitive to uncertainties in the water vapor concentrations. This study aims to determine the sensitivity of the TOA RF and profiles of the heating rates to water vapor either derived from ECMWF ERA5 or predicted from the ANN model in the UTLS, and the uncertainty is computed with LibRadtran.

To this end, meteorological conditions described in Chapter 5.1.4 from ECMWF model level data between 100.66 hPa (level 60) and 1031.25 hPa (level 137) are used as input to the ANN model. The resulting q profiles are used to update the original ERA5 humidity profiles and serve as input for libRadtran. The case selected for LibRadtran RTM simulations is 14 April 2021 and the area of interests is over the Atlantic Ocean (Please refer to details about the latitude, longitude, spatial and temporal resolution in Table 5.1 in Chapter 5.1.1). The cloud liquid water content and ciwc are kept consistent and derived directly from ERA5 in these two RTM experiments to avoid the potential effects from cloud RF. The surface properties are also obtained from ERA5.

The differences in the vertical humidity profiles from modelled dataset or from the ANN model are first investigated. The H2O gas density (in number of molecules) from the original ERA5 in Figure 5.12a is compared with that from the ANN model in Figure 5.12b for the case in 14 April 2021. Figure 5.12c suggests that the ANN model reduces the water vapor around 8 km (in blue), while increases the humidity density in the higher levels (in red).

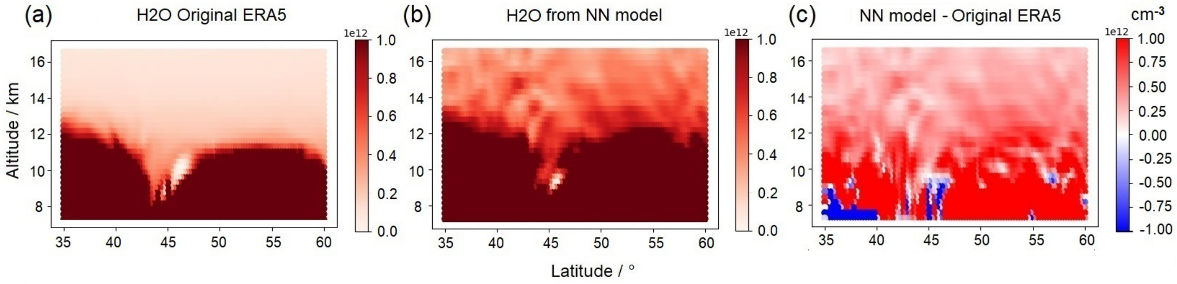

Figure 5.12: Water vapor number density from (a) ERA5 or (b) the ANN model and (c) the differences at 10:00 UTC on 14 April 2021.

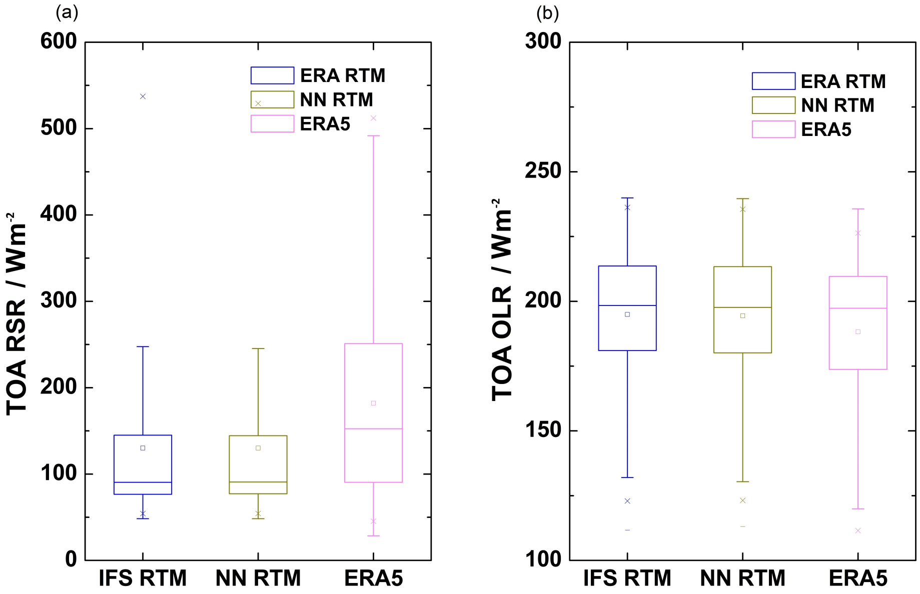

Figure 5.13: TOA (a) RSR and (b) OLR from RTM simulations using the humidity from ERA5 or the ANN model and the comparison with ERA5 radiation products at 10:00 UTC on 14 April 2021. Each bar contains the information of the maximum, minimum, inter-quartile range (25th percentile to 75th percentile), median (horizontal line) and mean (square) radiation.

Figure 5.13 shows the comparison of the SW and the LW radiation at the TOA (i.e. RSR and OLR) between RTM simulations with original humidity data set from ERA5 or improved humidity from our ANN model, and ERA5 radiation products. ERA5 provides a mean RSR of about 150 Wm^{-2} and a mean OLR of around 195 Wm^{-2} over the Atlantic Ocean. RTM simulations are generally smaller than ERA5 data in RSR but larger than that in OLR. The discrepancy observed in RSR is not attributable to the absorption of water vapor, as this solely affects thermal spectral irradiances. Instead, this variation in RSR can be attributed to the different cloud overlap assumptions [Morcrette and Jakob, 2000] and surface information derived from ECMWF model simulations. Compared with original humidity, my corrected humidity values lead to a similar TOA RSR in Figure 5.13a but a slight smaller OLR of 2 Wm^{-2} in Figure 5.13b, which are more comparable to ERA5 data.

The humidity profiles in Figure 5.12a and b are incorporated into the LibRadtran RTM and the simulated heating rate profiles are shown in Figure 5.14a and b. Comparing with the ERA5 humidity, the increased humidity from the ANN model contributes to the local temperature decrease - smaller warming effect as shown in Figure 5.14c with the heating rate of 0.1 K/day in the UTLS, but the temperature increase - stronger warming effect of 0.1 K/day above the surface, even if lower tropospheric humidity is unchanged. It can be explained by the additional thermal radiation of water vapor from the upper levels. The RTM simulations are in agreement with the findings from Forster and Shine [1999]. When water vapor is changed, the variation in temperature in the UTLS depends on the balance between increased absorption of upwelling infrared radiation from the troposphere and the emission of more infrared radiation by the stratosphere. This study has the potential to improve humidity forecasts for the UTLS region, and thus to improve radiation budget calculations for climate research applications.

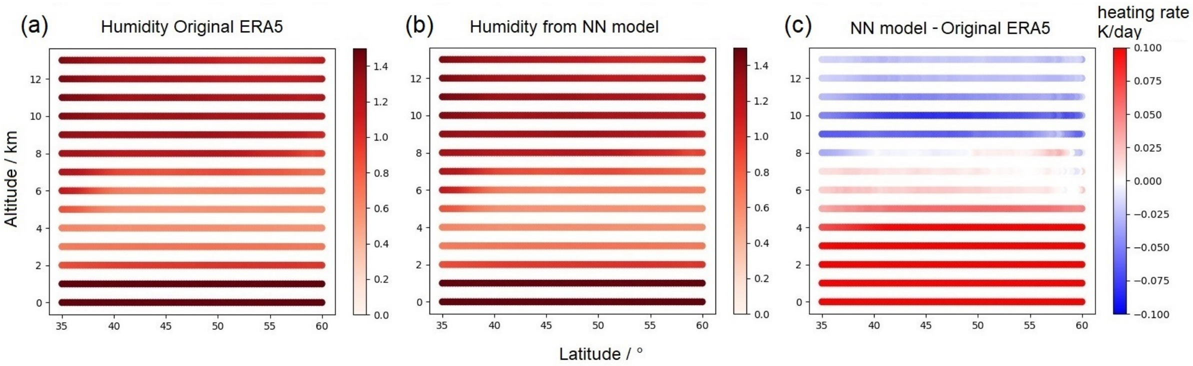

Figure 5.14: Atmospheric heating rate profiles influenced by the humidity from (a) ERA5 or (b) the ANN model and (c) the variations at 10:00 UTC on 14 April 2021.

5.6 Application to other geographic regions and comparisons with the existing method

The ANN humidity prediction model is built upon ERA5 meteorological conditions and IAGOS water vapor measurements in 2020 over the North Atlantic Ocean. Here I intend to test the feasibility of the model applied to other regions apart from NAR for the preparation of further contrail cirrus simulations, and to compare the accuracy of humidity prediction with the metrics from the existing method, for instance, Teoh et al. [2022a].

The model was exploited for the prediction of q in Asia and Australia, and US, separately. In Figure 5.15, the comparisons between q either from ERA5 or from the ANN model and IAGOS measurements in these two regions are shown. ERA5 data show an underestimation of q in Asia and Australia and US in Figure 5.15a and c, which is similar with the findings in Figure 5.7. Considering the IAGOS measurements as the reference, in contrast to ERA5 q, the ANN predicted q in Figure 5.15b shows an increase of R2 from 0.41 to 0.61, reducing the MAE from 0.12 g/Kg to 0.09 g/Kg and the RMSE from 0.16(58.17%) to 0.13(47.24%). However, the predicted q is a little overestimated in US.

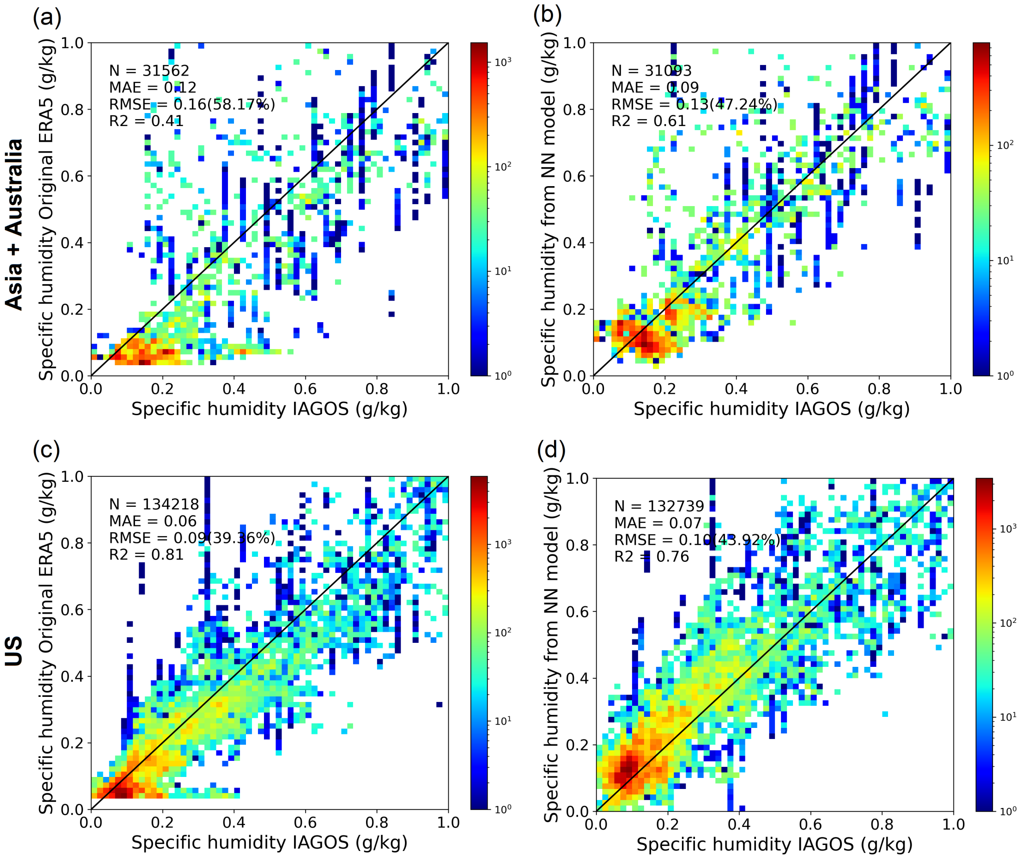

Figure 5.15: Overall accuracy of specific humidity from ERA5 and the ANN model against IAGOS measurements in Asia and Australia, and US. (a) ERA5 in Asia and Australia. (b) q predicted from the ANN model in Asia and Australia. (c) ERA5 in US. (d) q predicted from the ANN model in US.

Teoh et al. [2022a] developed a new statistical approach to correct the ERA5 humidity fields in particularly ISSRs, with the aim to resemble the probability density function (PDF) of the ERA5-derived RHi and the IAGOS in situ measurements inside ISSRs.

Through a comparison of ISSR occurrences measured from the IAGOS campaign in 2019 and those derived from the ERA5 high-resolution realization and 10-member ensemble with the humidity correction, the ETS can reach up to 0.424 and 0.395 for the high-resolution and ensemble data sets, respectively. This existing statistical method acknowledges its inherent limitation that the errors could be introduced at an individual waypoint level because the optimisation was performed using the PDF for the full trend of ISSRs. Table 5.2 shows the ETS of the ISSRs derived from ERA5 data and predicted from the ANN model. The statistical method outperforms ERA5 in predicting ISSRs, as the latter achieves an ETS of approximately only 0.2. While not a direct comparison within the same time frame, the ANN model excels in forecasting ISSRs, demonstrating superior accuracy with an ETS as high as 0.65.

Chapter 6

Predicted contrail cirrus from improved humidity

In Chapter 5, the possibility has been demonstrated to improve ERA5 RHi using thermodynamic conditions and dynamical states along with their temporal evolution as input and measured humidity as output to an ANN. In this chapter, for climate research applications, the contrail cirrus prediction model CoCiP (in Chapter 3.5) and MSG satellite observed SW and LW irradiances (in Chapter 2.2.3) are combined to reveal the influence of the improved prediction of RHi on the assessments of climate impact of contrail cirrus. CoCiP has adopted different correction methods [Schumann et al., 2021b, Teoh et al., 2022a] to improve humidity which is the key to contrail persistence. In this context, ECMWF IFS forecast data are used instead of the ERA5 reanalysis as input for the ANN model to leverage the contrail prediction capabilities of CoCiP for the upcoming hours and possibly even days. So as to determine the efficiency of humidity prediction improvements from the ANN model developed in Chapter 5.2, CoCiP was run for two experiments first without any correction and then with the humidity correction from the ANN model. The vertical pressure levels used here are between 200 hPa and 400 hPa.

6.1 Contrail cirrus prediction with improved humidity

As an illustrative example, this section compares the simulated optical properties and radiative effects of contrail cirrus using CoCiP with original IFS humidity and that derived from the ANN model at 10:00 UTC on 14 April 2021 (the same case discussed in Chapter 5.5). The case in Figure 6.1 is from the ECLIF-3 campaign and can be validated in details with the aircraft measurements in the future. The contrail cirrus cloudiness in this scene situate above the ocean, extending from west of Ireland to the Apennine Peninsula, and move eastwards, surrounded by thick natural cirrus fields.

In Figure 6.2a, CoCiP simulations show large contrail optical thickness being roughly 0.5 over the North Atlantic flight corridor and reaching up to 0.75 above the continent.

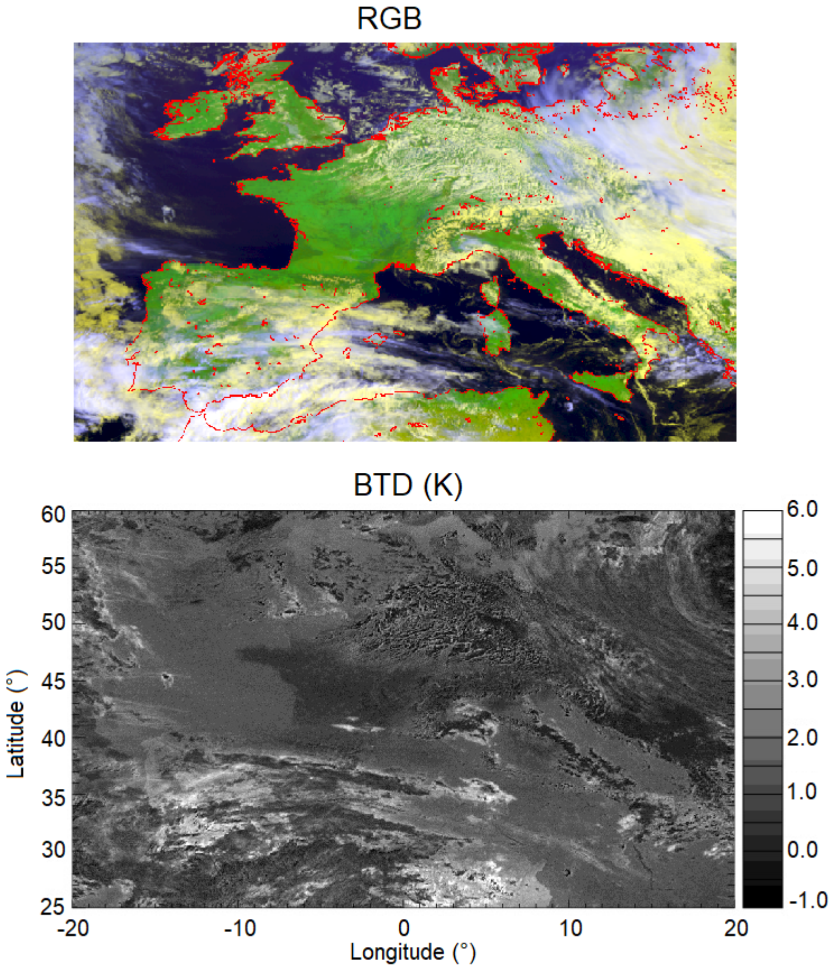

Figure 6.1: RGB and BTD over the NAR and the Europe continent at 10:00 UTC on 14 April 2021.

Upon substituting the input humidity dataset from ECMWF IFS with the corresponding humidity values from the ANN model, a visual comparison of the CoCiP simulated optical thickness reveals an enhanced contrail formation and an expanded classification of pixels as contrails in Figure 6.2b. The IOT values within the cores of contrails increases to levels exceeding 1.0.

For the radiative effects, contrails in Figure 6.2c have larger SW RF (ca. $30\,Wm^{-2}$, negative values also in the following description) over the ocean surface than $20\,Wm^{-2}$ over the Iberian Peninsula. In contrast, the core of contrails simulated with improved humidity in Figure 6.2d shows values around $40\,Wm^{-2}$ and even larger, with values of $20\,Wm^{-2}$ at the edges. Abundant water vapor promotes the growth of contrails and prolongates their life time. The simulated LW RF using humidity data set from ECMWF IFS in Figure 6.2e has values of $20\,Wm^{-2}$ close to the core of contrails. With an increased concentration of moisture, the simulations of LW RF correspondingly increase up to $35\,Wm^{-2}$ in Figure 6.2f, showing subtle variations compared to those observed between Figure 6.2c and d.

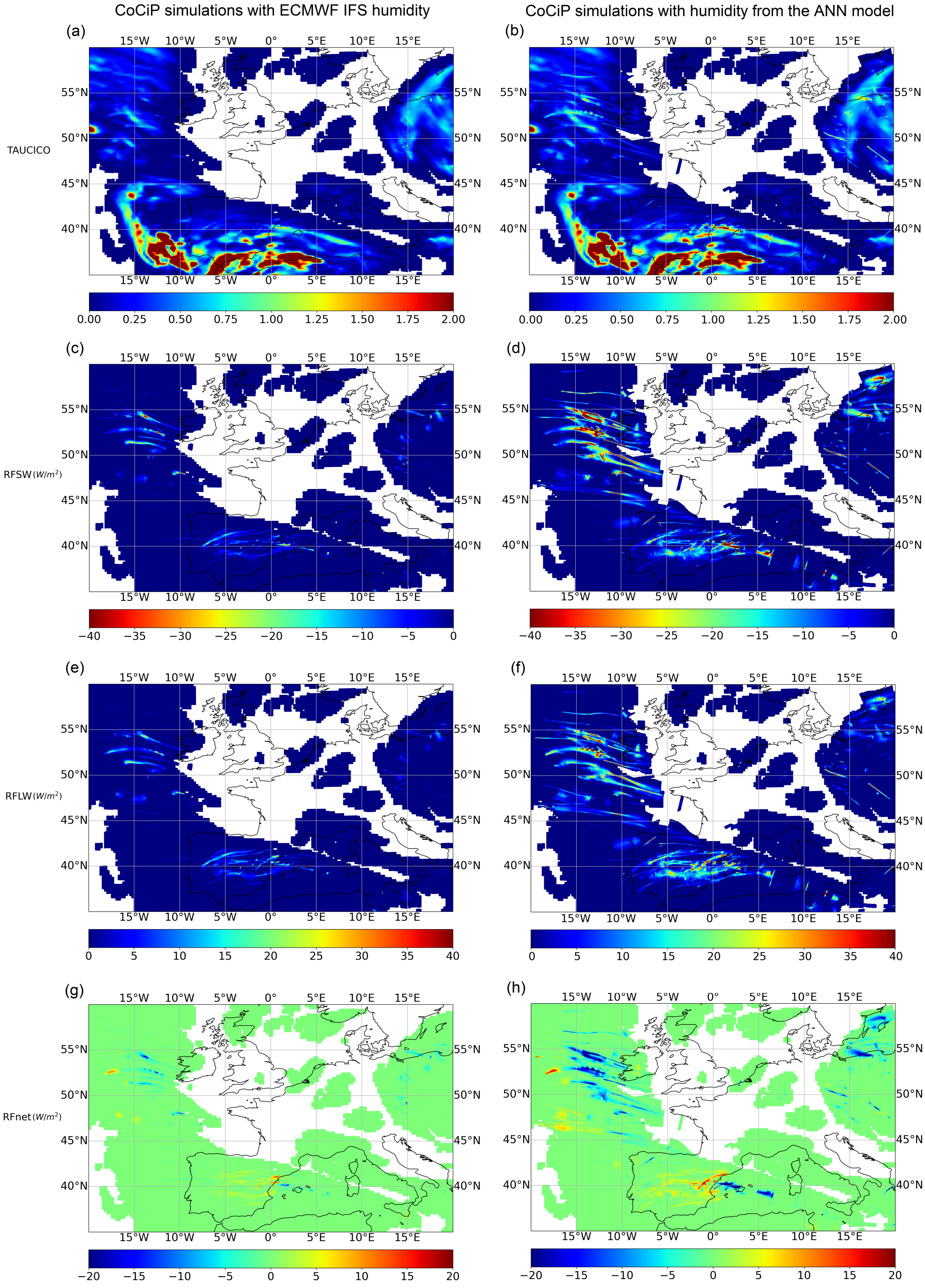
CoCiP simulations with ECMWF IFS humidity
CoCiP simulations with humidity from the ANN model
(a)
(b)
(c)
(d)
(e)
(f)
(g)
(h)
TAUCICO
RFSW (W/m^2)
RFLW (W/m^2)
RFnet (W/m^2)
15°W 10°W 5°W 0° 5°E 10°E 15°E
55°N 50°N 45°N 40°N
0.00 0.25 0.50 0.75 1.00 1.25 1.50 1.75 2.00
−40 −35 −30 −25 −20 −15 −10 −5 0
0 5 10 15 20 25 30 35 40
−20 −15 −10 −5 0 5 10 15 20

Figure 6.2: Comparisons of contrail cirrus derived from CoCiP simulations using humidity from ECMWF IFS and the ANN model for (a) and (b) IOT, (c) and (d) SW RF, (e) and (f) LW RF, and (g) and (h) net RF at 10:00 UTC on 14 April 2021.

Ultimately, negative net RF is found in Figure 6.2g around 10 Wm^{-2} over the ocean and then positive values around 10 Wm^{-2} over Spain. For Figure 6.2h, the significant change is observed in the simulations at the core of the simulated contrails. This observation suggests that the presence of sufficient moisture leads to the increase of both SW and LW radiation, particularly pronounced in the SW range because of the higher reflection from larger IOT. In addition to the influence of increased actual humidity, CoCiP simulations are subject to inherent limitations that could contribute to inaccuracies. The transformation process of IAGOS measured water vapor data sets to specific humidity, as utilized in the training data, has introduced a certain wet bias when compared to the official ECMWF IFS.

6.2 Contrail cirrus predictions against MSG observations

6.2.1 Macrophysical and optical properties

Figure 6.3 and 6.4 provide a comparison of spatial distributions and occurrences of model-simulated and MSG-observed IOT, focusing on the accuracy difference induced from ECMWF IFS humidity and predicted humidity from the ANN model. Regarding microphysical properties, the reference IOT is extracted from MSG observations using the CiPS algorithm, as detailed in Chapter 3.1.1. It is assumed that the observed contrail signatures are not predominantly influenced by model and observation errors. The modeled and observed spatial distributions of IOT exhibit similarities, quantified by assessing the occurrences across the entire NAR area. The distribution of IOT simulated using ECMWF IFS humidity exhibits a decrease from 0.0 to 1.0, with the highest bin encompassing IOT values up to 0.2, and the subsequent bins (second to fourth) indicating lower IOT levels ranging from 0.2 to 0.8. There is a sharp decrease in IOT occurrence from 0.8 to 1.0. Conversely, the IOT distribution simulated using the improved humidity prediction from the ANN model decreases almost smoothly from 0.0 to 2.0, showing a comparable value range and trend to MSG observations, except for an underestimation of IOT between 0.8 and 1.6. Generally, the correlation is higher between simulated results using predicted humidity and observations, followed by simulations with ECMWF IFS and reference values. The inclusion of predicted humidity from the ANN model enhances the model-observation agreement. Notably, contrail cirrus and natural cirrus IOT simulated from CoCiP serve as masks for both model simulations and satellite observations. Due to the challenge in collocating CoCiP grid boxes with MSG observed pixels in different temporal and spatial scales, a pixel-to-pixel comparison is not operationally feasible in this context.

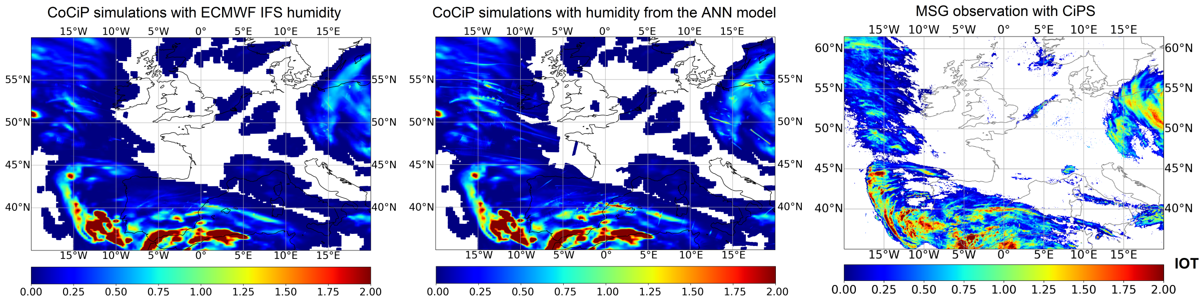
CoCiP simulations with ECMWF IFS humidity
CoCiP simulations with humidity from the ANN model
MSG observation with CiPS
15°W 10°W 5°W 0° 5°E 10°E 15°E
60°N
55°N
50°N
45°N
40°N
IOT
0.00 0.25 0.50 0.75 1.00 1.25 1.50 1.75 2.00

Figure 6.3: Distributions of IOT simulated from the CoCiP model using humidity from ECMWF IFS or the ANN model and that retrieved from MSG observations using the CiPS algorithm at 10:00 UTC on 14 April 2021.

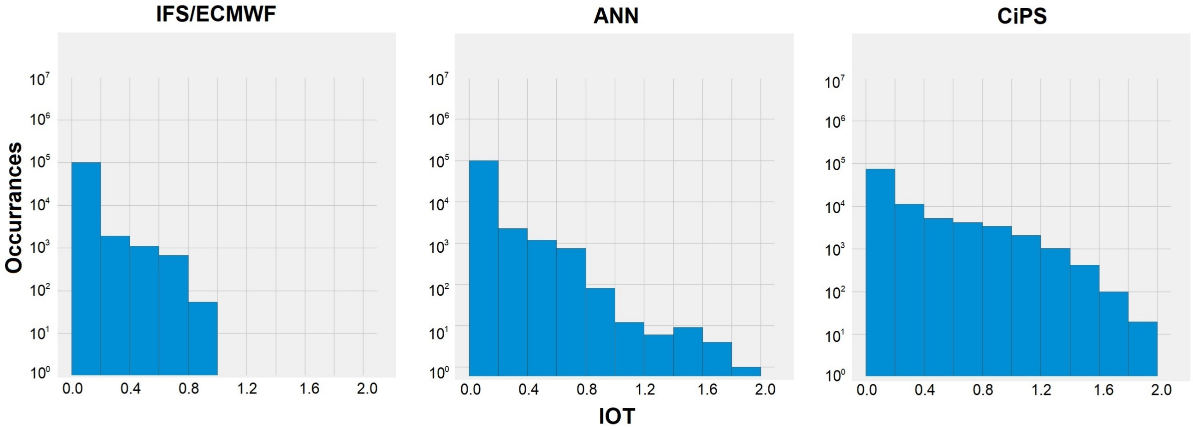

Figure 6.4: Occurrences of IOT simulated from the CoCiP model using humidity from ECMWF IFS or the ANN model and that retrieved from MSG observations using the CiPS algorithm at 10:00 UTC on 14 April 2021. All IOT values are masked with CoCiP simulated cirrus grid boxes for the histogram of the IOT occurrence statistics.

6.2.2 Radiative effects

Figure 6.5 illustrates the spatial distributions of model simulations and satellite observation results for OLR and RSR, highlighting mean differences arising from the utilization of ECMWF IFS humidity versus humidity from the ANN model. In this context, observed OLR and RSR are derived from MSG observations using the RRUMS algorithm, as outlined in Chapter 3.1.2. Consistent with the findings on IOT, regions indicating a significant enhancement of RSR and a noticeable increase in OLR when simulated with improved humidity compared to ECMWF IFS are notably evident over the NAR ocean. The occurrences of SW and LW irradiances have been analysed to explore the mean modeled and observed spatial differences.

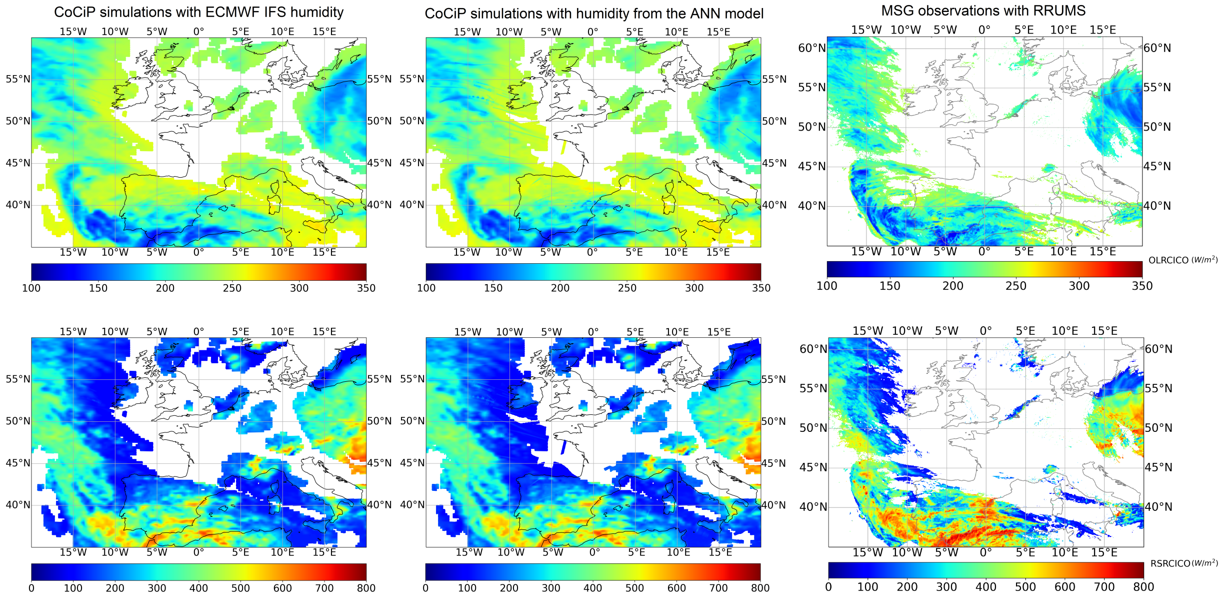
CoCiP simulations with ECMWF IFS humidity
CoCiP simulations with humidity from the ANN model
MSG observations with RRUMS
15°W 10°W 5°W 0° 5°E 10°E 15°E
60°N
55°N
50°N
45°N
40°N
100 150 200 250 300 350
OLRCICO (W/m²)
0 100 200 300 400 500 600 700 800
RSRCICO (W/m²)

Figure 6.5: Distributions of RSR and OLR simulated from the CoCiP model using humidity from ECMWF IFS or the ANN model and those retrieved from MSG observations using the RRUMS algorithm at 10:00 UTC on 14 April 2021.

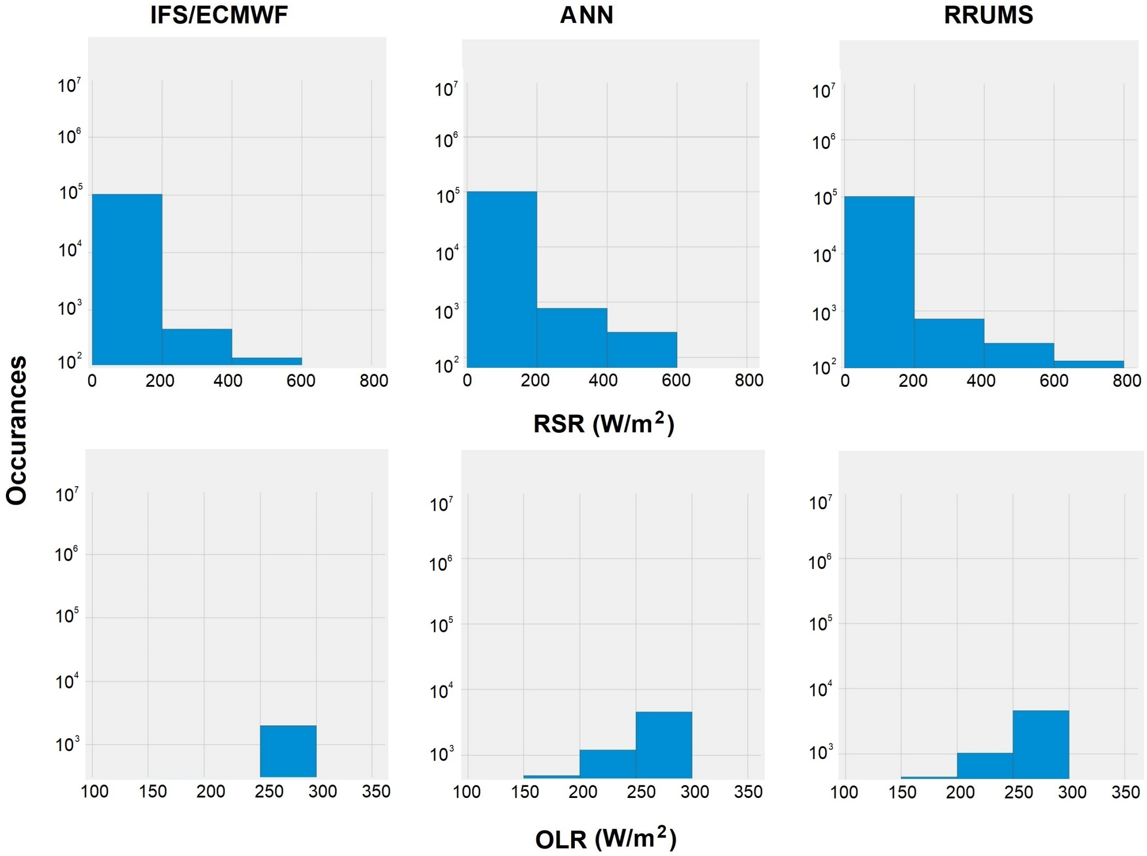

Figure 6.6: Occurrences of RSR and OLR simulated from the CoCiP model using humidity from ECMWF IFS or the ANN model and those retrieved from MSG observations using the RRUMS algorithm at 10:00 UTC on 14 April 2021.

As depicted in Figure 6.6, the RSR distribution observed from MSG spans from 0 to 800 Wm^{-2}, suggesting a combination of contrail cirrus and thick natural cirrus. The initial bin is the highest, concentrating around 200 Wm^{-2}, with a following gradual decrease in RSR occurrence. The model-simulated RSR using ECMWF IFS humidity and improved humidity aligns reasonably well with observed values, exhibiting larger or smaller values, respectively. Regarding OLR, observed values range from 150 to 300 Wm^{-2}. The model-simulated OLR with predicted humidity from the ANN model corresponds closely to MSG observations. However, occurrences of OLR simulations using ECMWF IFS humidity decrease by one order of magnitude when OLR falls between 150 and 250 Wm^{-2}. In general, the model results demonstrate increased comparability with MSG observations when the improved humidity prediction from the ANN model is incorporated. In the test case, contrail cirrus optical thickness and radiative effects increase following this humidity correction. These contrail cirrus simulations provide the basics for addressing contrail cirrus climate impact mitigations. Given that ISSRs typically exhibit large horizontal but shallow vertical extensions [Spichtinger et al., 2003], a minor adjustment in cruising altitude, avoiding regions of high humidity, can potentially reduce contrail forcing.

6.3 Small-scale diversion strategy

Several studies have evaluated different flight diversion strategies to minimize the formation of persistent contrails and their climate impact by avoiding ISSRs [Teoh et al., 2019, Sausen et al., 2023]. Here, an alternative metric that has been used to quantify the contrail climate forcing is the energy forcing (EF, in units of J) integrating local contrail RF, length, and width, and the contrail lifetime.

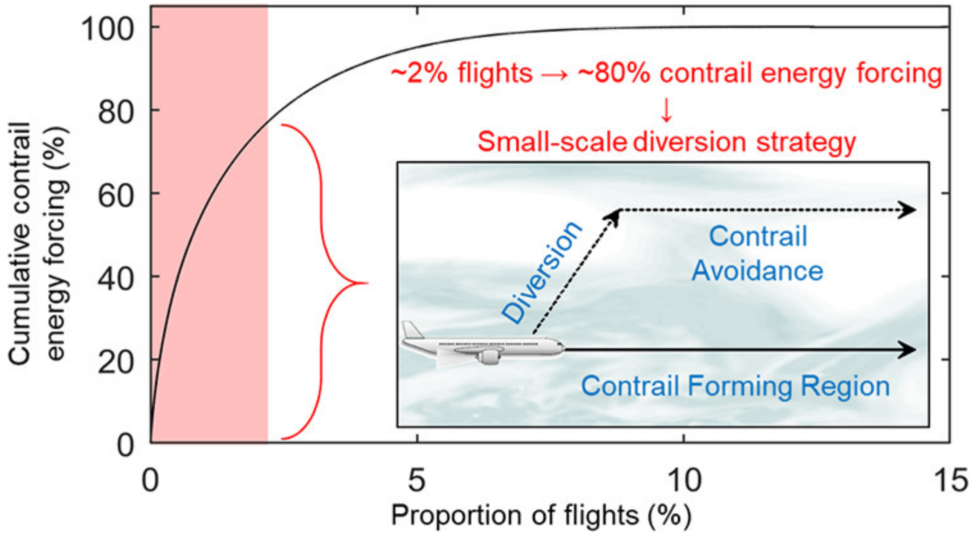

Figure 6.7: The concept of the contrail climate impact mitigation strategy with small scale diversion strategy. Figure from Teoh et al. [2020].

In Figure 6.7, the concept of the contrail avoidance strategy with small scale diversion strategy to avoid the contrail formation region is shown. In fact, a fleet-wide diversion strategy is neither practical nor necessary given that only 2.2% of flights contribute to 80% of the total contrail EF over Japan [Teoh et al., 2020]. In the short term, a small-scale strategy which selectively diverts flights with the largest EF could significantly reduce the contrail climate forcing, minimize disruptions to air traffic management, and be implemented quickly without technological changes.

Previous studies found that ISSRs typically have large horizontal (150 ± 250 km) but shallow vertical extensions (of order 488 m) [Spichtinger et al., 2003]. Therefore, a small adjustment in cruising altitude could minimize the flight distance within regions characterized by high humidity, thereby leading to a reduction in both contrail lifetime and EF. Notably, because of seasonal variations of the tropopause height, contrail EF is more efficiently reduced when the aircraft are directed to lower cruising altitudes in the summer months and conversely during winter.

Over the longer term, widespread adoption of cleaner fuel and engines could reduce the contrail forcing. 50% biofuel blending has the capability to reduce the number of soot particles and further N by 70% [Voigt et al., 2021]. Soot emissions from the lean burn engine are also reduced to a similar degree with the biofuel blending. The water-enhanced turbofan (WET) engine traps the water vapor mixing ratio for the initiation of contrails. Contrail segments produced by hydrogen turbofan combustion have fewer ice particles with larger mean radii than those of biofuel blending [Ström and Gierens, 2002, Bier and Burkhardt, 2022]. For a 50% reduction in N, Bock and Burkhardt [2019] found a 14% reduction in net RF in the Eastern China and Japan region, and for an 80% reduction in N, Burkhardt et al. [2018] calculated a 50% reduction in net RF globally. However, the operation of these strategies takes time.

Chapter 7

Summary, conclusions and outlook

The focus of this dissertation is the investigation of microphysical properties and radiative effects of a contrail cirrus outbreak, and the improvement of relative humidity predictions from a NWP model to better assess contrail cirrus climate impact. The contrail cirrus outbreak study combines detailed airborne in situ and lidar measurements from the HALO aircraft over the NAR and MSG/SEVIRI geostationary satellite observations, and develops a new cirrus classification method and a RTM based TOA irradiance estimation algorithm, with the aim to be applicable to a broader data set of any natural and anthropogenic clouds as far as possible. The novel prediction of humidity uses the modelled thermodynamic conditions and dynamical states with their temporal evolution from ECMWF ERA5 as input and measured humidity from IAGOS as output, and is based on artificial neural networks, targeting to simulate more accurate contrail cirrus radiative effects. This research provides new knowledge on the differences between natural cirrus and contrail cirrus and their evolution, and supplies reference data of clouds and water vapor for numerical and global climate models.

In Chapter 4 the microphysical properties of natural cirrus, contrail cirrus and contrails in similar meteorological conditions were distinguished and identified from in situ measured clouds particles and NO, and the RF of natural cirrus and contrail cirrus are derived by satellite observations based RTM in an air traffic region favorable for contrails formation and evolution. Building upon the non-negligible climate impact of contrail cirrus and the corresponding influences from ambient relative humidity, Chapter 5 described the creation of an extensive training data set, the development of a novel relative humidity prediction, the interpretation and the validation of the method, and the application to the investigation of atmospheric water vapor radiation budget. Finally, Chapter 6 includes the further comparisons of contrail cirrus simulated from numerical model using the humidity from ECMWF IFS and the ANN model and that observed from satellite data, with a discussion on contrail cirrus mitigation strategies. In the following, the main results are summarized in light of the three scientific questions formulated in Chapter 1.2 and corresponding outlooks are given.

1. What are the microphysical properties and radiative effects of contrail cirrus and

natural cirrus in a contrail cirrus outbreak?

To answer this question, a detailed investigation of an ideal contrail cirrus outbreak event using a case study focusing on the NAR on 26 March 2014 during the ML-CIRRUS experiment with in situ probes and lidar measurements from the HALO research aircraft and geostationary satellite observations was conducted. This contrail cirrus outbreak case is chosen because of the large contrail cirrus coverage and high air traffic density. As the flight operation in all altitudes is not easily granted due to the high air traffic load in the NAR, the data presented here are also rare and unique in the sense that HALO was able to operate and acquire in-flight measurements of contrail cirrus perpendicular to the flight tracks of the NAR. From satellite remote sensing, few low-level water clouds and the relatively homogeneous oceanic background increase the sensitivity to retrieve cirrus properties. On the morning of that day, the HALO research aircraft flew for 3 h in or above natural cirrus, contrail cirrus and contrails. Various contrails with related fall streaks have been identified in airborne lidar backscatter data which merge to a larger cloud with a vertical extent of 2 km that dissipates with time. High resolution RGBs and BTDs from MSG/SEVIRI also reveal the presence of various line shaped structures that represent contrails. Simultaneous airborne humidity measurements from AIMS show RHi between 80% and 120%, in line with lidar observations indicating a region where contrails formed, evolved and merged with natural cirrus. Thus, combined evidence from satellite and aircraft data suggest the presence of an ideal contrail cirrus outbreak event.

Aircraft plumes are identified using peaks in NO data with an approach that takes care of the variable NO background and contrasts contrails and contrail cirrus on the basis of measured ice number concentrations. As shown in Figure 4.7, the mean radii of contrails or contrail cirrus is about 18% smaller than that of natural cirrus in that case, suggesting a self-stabilizing mechanism of smaller contrail cirrus particle sizes surviving due to higher ice number concentrations in contrail cirrus compared to natural cirrus. Ice particle sizes increase by about 144% during the transition from contrail to contrail cirrus by deposition of water vapor in regions with ice supersaturation.

For the purpose of obtaining accurate radiative effects of contrail cirrus and natural cirrus, a new TOA RSR and OLR estimation method is developed, which is based on detailed RTM calculations and exploits in situ measurements, satellite observations and ERA5 model atmospheric data. Using IOT from MSG/SEVIRI (CiPS), R_{eff} from in situ, cloud top and bottom height from the lidar, and gas, temperature and liquid water cloud profiles from ERA5, an input atmospheric state for the RTM has been defined that enables to compute RSR and OLR that compare well to MSG measurements (RRUMS). When the ice cloud layer is removed from the RTM input, RSR and OLR for cirrus-free conditions can be computed that are consistent in the background atmospheric states.

In a larger area of 36 × 51 SEVIRI pixels encompassing the HALO race track over NAR, the diurnal cycle of the contrail cirrus outbreak was computed. Cirrus RF is associated with the changes of cirrus coverage, CTH and IOT. Here, a positive net RF of the contrail cirrus outbreak region is found in the early morning, and the contrail cirrus outbreak warms at TOA till 09:00 UTC (Figure 4.11). Then, during the daytime the mean net RF of the contrail cirrus outbreak becomes negative, and the contrail cirrus outbreak cools. This outbreak resulted from uplift of moist air masses in a warm conveyor belt system modified by the jet stream circulation at cruise altitudes. In the long-term observations or hourly resolved simulations of contrail cirrus coverage and RF in the NAR, Graf et al. [2012], Duda et al. [2013] and Vázquez-Navarro et al. [2015] also find that the contrail coverage is important for the corresponding contrail RF and that a high variability of the contrail impact is exhibited. These studies indicate that contrail cirrus warm during the night, while a larger variability in contrail cirrus RF exists during the day. Teoh et al. [2022a,b] show that contrail cirrus often cools during daytime and that the cooling depends on many parameters including solar zenith angle and the surface albedo. For some cases with low clouds, Teoh et al. [2022a,b] also find warming of contrail cirrus during the day. In the absence of sunlight during the night time, however, contrail cirrus warms the atmosphere.

In order to reduce the uncertainty of the contrail cirrus climate impact research, I have developed a new method to derive the RF of contrail cirrus and cirrus, and this approach is tested using in situ and lidar observations in a contrail cirrus outbreak situation. The future study will aim at applying the method to a broader data set to investigate the radiative effects of cirrus and contrail cirrus using RTM simulations involving CTH and IOT from satellite, R_{eff} from in situ values, and CBH and cloud thickness from lidar.

This work is valuable for identifying contrails, contrail cirrus and natural cirrus from different platforms, estimating TOA RF from satellite data, and assessing microphysical properties and climate impacts of anthropogenic cirrus and natural cirrus, and can help to formulate appropriate contrail mitigation options.

2. Is there a possibility to improve the RHi prediction from ERA5 with thermodynamic conditions and dynamical states?

To answer this question, the significance of ice supersaturation on the persistence and climate impact of contrail cirrus from Chapter 4 and the bias of humidity in the UTLS as well as the mechanisms behind were accounted for to investigate the potential in the improvements of humidity prediction in Chapter 5.

The UTLS region is of special interest for dynamical and chemical processes as well as the associated (contrail) cirrus cover and RF. In particular, contrails that are formed in this region can survive for hours if the surrounding air is supersaturated with respect to ice. Persistent contrails have a considerable impact on the radiation budget and represent the large contribution to the ERF of aviation. However, water vapor in the UTLS is subject to uncertain spatial distributions and temporal variations. For instance, IAGOS shows a significantly greater amount of smaller ISSRs compared to ERA-Interim [Reutter et al., 2020]. Sensitivity analyses are also performed in Teoh et al. [2022a] to compare the difference in mean contrail properties from individual flights between the nominal simulation with humidity correction applied to the ERA5 or vice versa. Without correction of the humidity fields, the estimated contrail cirrus net RF is halved relative to the simulation where the humidity correction is applied.

Favorable thermodynamic conditions and dynamical states are linked with RHi in Gierens and Brinkop [2012], Gierens et al. [2020]. Thus, the improvement of ice supersaturation predictions and the associated contrail cirrus RF estimation is possible by accounting for atmospheric quantities. Dyroff et al. [2015] has also assessed that the highest RHi bias in the UTLS originates from low pressure and high latitudes due to vertical stratospheric intrusions and horizontal airmass transport. This highlights the need of accounting for temporal and spatial meteorological variables to evaluate atmospheric water vapor. The temporal and vertical dependence of RHi on meteorological conditions is determined, through calculating the Spearman's correlation coefficient between collocated weather conditions at certain time and level from ERA5 and RHi at the acquisition time and location from IAGOS, focusing on vertical water vapor transport from below and uplift of cold air masses in the UTLS. As is described in Figure 5.4, the correlations between thermodynamic conditions from ERA5 including RHi and temperature and IAGOS RHi at the IAGOS acquisition time stay constant but those from dynamical states, for example vertical and horizontal wind speed, divergency, and relative vorticity, apart from geopotential, vary over time. The impact of thermodynamic conditions and dynamical states on the RHi of the IAGOS acquisition level varies with vertical pressure. Thus I include the atmospheric quantities with time lags and pressure differences in the humidity prediction process. The confidence interval analysis was also performed, and the results exclude the insignificant relationship between RHi and vertical velocity at 5 h before and that and potential vorticity at 1 h and 3 h before. Sensitivity analyses indicate that the combination of previous (-2 h, -6 h) and current atmospheric states within the difference of 2 pressure levels present the high predictive skill for the current humidity status. In the later stage of interpreting the built ANN humidity prediction model with modelling meteorological conditions and measured humidity, relative contributions of multiple meteorological conditions are demonstrated with the calculated quantitative relative change in loss. Humidity, temperature, and geopotential (altitude) in Figure 5.6 show strong influences on the humidity prediction, while the impact from other dynamical states on RHi is also non negligible.

The novel humidity prediction model based on ANN was developed in Chapter 5.2 with the aim to build a general-purpose humidity correction approach for improving the existing humidity data records, and to simulate more precise contrail cirrus radiative effects. Our approach includes mainly two key points: input data for training the model were collected from modelled thermodynamic conditions and dynamical states from ECMWF ERA5, and verified to cover the temporal and vertical dependence of humidity on meteorological conditions; an extensive set of measured humidity from IAGOS as the output data for building the model represents the humidity distribution in the UTLS. Such a wide range of atmospheric states and measurements, especially newly introduced dynamical states and their temporal evolution, constitutes the main difference to other existing humidity correction methods using the general regression.

Our model predicts the specific humidity and RHi mainly in the UTLS region. The performance of the ANN model with respect to different humidity categories and different UTLS regions and cloud-free and cloudy scenarios was investigated by performing systematic tests of the predictions using independent test data set which were created similarly as the original training data. The model predicted humidity shows higher correlation ($R2 \geq 0.75$ w.r.t specific humidity q; $R2 \geq 0.94$ w.r.t. RHi) and lower error ($RMSE \ll 0.09\,\mathrm{g/kg}$ w.r.t q; $RMSE \ll 8.92\%$ w.r.t. RHi) compared with the long term airborne observed humidity from IAGOS (Figure 5.7 and Figure 5.8) than ERA5 data. These improvements are general in cloudy or cloud-free scenarios, and UT or LS. Especially in the LS and UT area, the ERA5 RHi bias is largely reduced, with the increase of correlation by up to 0.25 and the decrease of MAE up to 9.07% and 0.03 g/kg for RHi and q, respectively. It is found that the underestimation of ERA5 q firstly decreases with the MBPE from 25% to 10% when q is smaller than 1 g/kg, and then increases with the MBPE up to 20% until the humidity is 2 g/kg. However, the dry bias from ERA5 RHi presents an continuous increasing trend (see Figure 5.9). The ANN model improves both the q and RHi prediction, with the slight wet bias for lower water vapor and the dry bias when the humidity values are exceeding 1 g/kg or the RHi is saturated.

The ANN prediction model was applied to airborne in situ measurements for a specific contrail cirrus case during the CIRRUS-HL campaign in 2021. The predicted RHi is in very good agreement with the reference in situ data. From Figure 5.10, our developed model can reduce the wet bias of ERA5 from 40% to the values within the range of ± 10%, which confirms the enhanced accuracy of the RHi prediction. Furthermore, the contingency table and the ETS calculation were used to give the quantitative validation of the ISSRs prediction from ERA5 or from the ANN model. The "scores" for the ability of ERA5 to predict ISSRs are 0.05, 0.25, 0.14 and 0.22 in clear, cloudy, LS and UT regions, respectively. The ANN model partly releases the limitation to predict ISSRs, with the increases of the ETS score values about 0.45, 0.65, 0.65 and 0.64. For the updated RTM based simulations of atmospheric water vapor radiation budget, in agreement with the findings from Forster and Shine [1999], a decreased q in part of the UT but an increase of q in the LS of the vertical profiles induces a warming effect at the surface and a locally smaller warming effect in the UTLS in Figure 5.14.

To conclude, the validation showed that the dynamic-based humidity prediction model is able to perform with reasonable accuracy over a wide range of atmospheric conditions as well as application scenarios. Especially the satisfying results for different UTLS regions and cloud-free and cloudy areas indicate that the approach can be applied to arbitrary meteorological conditions. This study has the potential to improve humidity forecasts in the UTLS region, to constrain uncertainties in the assessment of contrail cirrus radiative impacts, and to formulate and evaluate contrail mitigation options for climate research.

3. How does an improved prediction of RHi influence the predicted climate impact of contrail cirrus?

To answer this question, the humidity from both ECMWF IFS data sets (not ERA5) and the ANN model in Chapter 5 were used to perform two experiments without or with humidity correction by contrail prediction model CoCiP simulations for the next hours in Chapter 6. Here, one case during the ECLIF-3 campaign in 2021 was selected for the comparisons (see Figure 6.2). An elongated contrail formation stretches from northwest of Ireland to the Iberian Peninsula, characterized by increased cirrus cloudiness resulting from the forecasted humidity, surpassing that obtained from ECMWF IFS. The improved humidity predictions lead to an increase in IOT, and the variation of the cirrus warming and cooling proportions.

As indicated in the introduction, one important field of application of satellite observed contrail cirrus radiative effects is the comparison with numerical model predictions for configuration and validation. Here, satellite observed macro-microphysical properties and TOA irradiances for the selected contrail cirrus case were compared to the model simulations in Figure 6.3 - Figure 6.6. The occurrence of IOT simulated using ECMWF IFS decreases from 0.0 to 1.0, with the sharp fall from 0.8 to 1.0. The IOT frequency simulated with improved humidity prediction from the ANN model decreases almost smoothly from 0.0 to 2.0, which are consistent with MSG observations in both range of values and trend. The RSR, simulated with ECMWF IFS humidity and predicted humidity, closely aligns with observed values. In contrast, the OLR, when simulated with predicted humidity from the ANN model, exhibits stronger agreement with MSG observations. Notably, instances of OLR simulations using ECMWF IFS humidity decrease significantly by an order of magnitude when OLR is between 150 and 250 Wm^{-2}. Generally, the simulated results with predicted humidity from the ANN model display higher consistency with observations, outperforming the experiment with ECMWF IFS. The humidity from the ANN model is more suitable to simulate contrail cirrus.

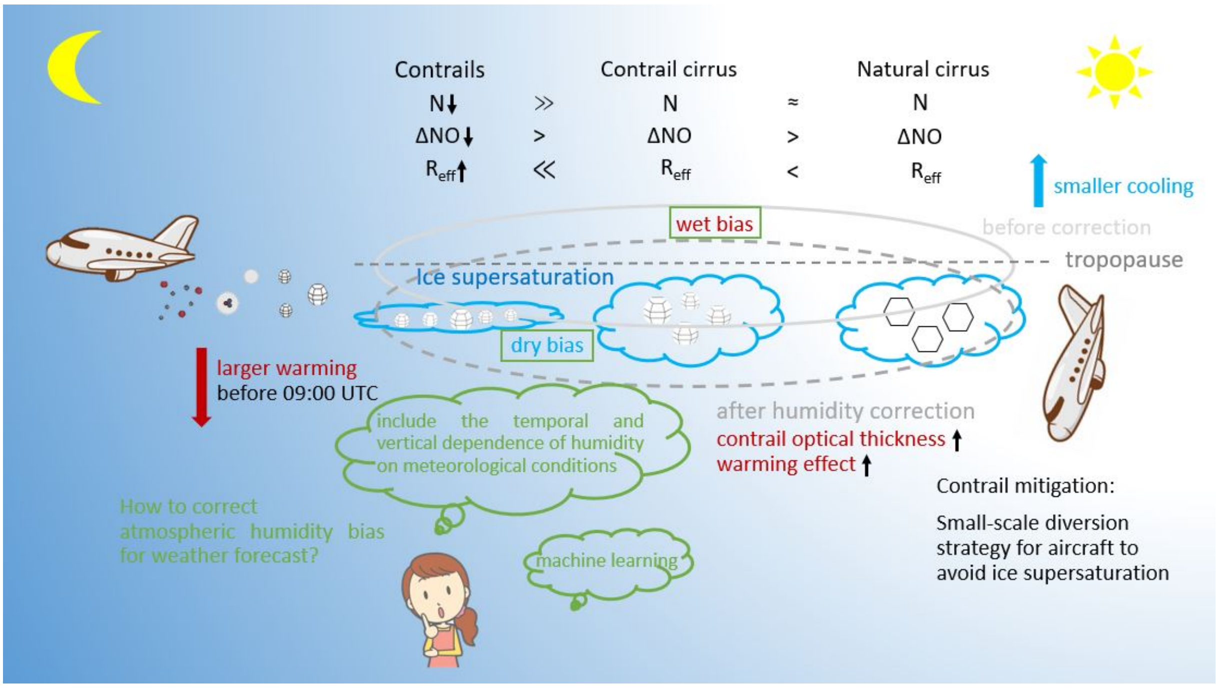
Contrails
Contrail cirrus
Natural cirrus
N↓ ≫ N ≈ N
ΔNO↓ > ΔNO > ΔNO
R_{eff}↑ ≪ R_{eff} < R_{eff}
smaller cooling
before correction
wet bias
tropopause
Ice supersaturation
dry bias
larger warming
before 09:00 UTC
include the temporal and vertical dependence of humidity on meteorological conditions
after humidity correction
contrail optical thickness ↑
warming effect ↑
Contrail mitigation:
Small-scale diversion strategy for aircraft to avoid ice supersaturation
How to correct atmospheric humidity bias for weather forecast?
machine learning

Figure 7.1: The sketch of climate impact of a contrail cirrus outbreak and a novel prediction of relative humidity for weather forecast.

A critical component of the tool, ISSRs prediction, has undergone significant improvement, potentially facilitating the implementation of contrail avoidance measures and mitigating the contrail climate forcing (See Figure 6.7). A small-scale diversion strategy for aircraft to avoid the ISSRs and warming contrails is then operational, based on the ice supersaturation prediction using the novel ANN method with the consideration of dynamical states, and the investigations of microphysical properties and radiative effects of contrail cirrus and natural cirrus in Chapter 4.

The conclusive outcomes of this thesis are eventually summarized in a sketch in Figure 7.1.

Outlook

This thesis firstly provides new insights in the microphysical properties and radiative effects of a contrail cirrus outbreak, combining airborne in situ and lidar measurements with geostationary satellite observations, and developing a new cirrus classification method and a RTM based TOA irradiance estimation algorithm. It also opens up for further studies. A broader data set with more contrail cirrus clouds could be identified and analysed in order to have a stronger statistical significance. This can be done by (1) extending the time period from one case study and the geographic location over the North Atlantic to several months or years and on a global scale; (2) including temporal evolution of cirrus clouds in the wider range of spatiotemporal scales as well. Extending the size of the used data set, however, requires a more automatized method for detecting the contrail cirrus, which has received increased attention nowadays [Hoffman et al., 2023]. Moreover, as aerosols can act as cloud condensation nuclei, it would be interesting to perform a similar study on anthropogenic cirrus clouds not produced by aviation but influenced by different aerosol sources, and compare the life cycles and the temporal evolution between them [Lohmann and Gasparini, 2017].

This research also develops a novel humidity prediction method, and analyzes the influences of humidity variations on the estimation of contrail cirrus climate impact, using the modelled thermodynamic conditions and dynamical states from ECMWF ERA5 as input and measured humidity from long term aircraft measurements from IAGOS as output, and profiting from the artificial neural network technique and contrail prediction modelling. Concerning further improvements of humidity prediction capacities building upon this developed approach, three pathways are available. First, the training data set can be expanded and the ANN can be retrained. Samples with collocated meteorological conditions and measured water vapor from the tropics or the polar regions could be included, as geographic locations influence dynamical processes of water vapor due to various dynamical states. Second, one could try to make the ANN more robust by applying further regularization to all inputs. Third, one could focus on further processing the retrieval outputs. It might be promising to evaluate the origin of the humidity once more and verify the mechanisms of vertical stratospheric intrusions and horizontal airmass transport. One ongoing next step involves comparing humidity predictions generated by the ANN model with those produced by other existing methods, such as the IAGOS statistical approach proposed by Teoh et al. [2022a]. The humidity prediction could serve as a benchmark for the measurements of further aircraft campaigns, and work as the reference or assimilation data set of the NWP model for a better parameterization of ice supersaturation [Schumann et al., 2021a]. The method could also be applied to other weather forecast models from ECMWF and from German or French Weather Services, which are used for daily weather predictions.

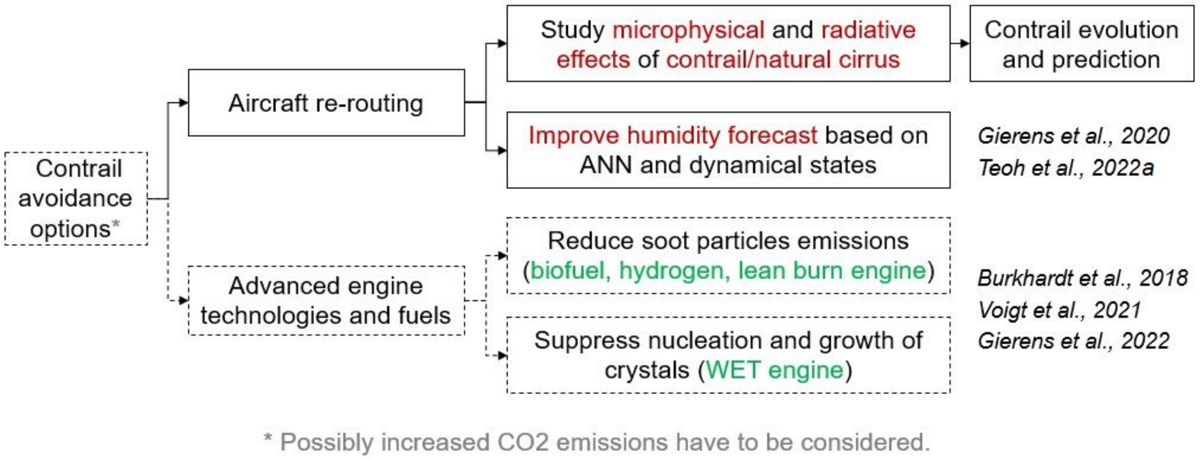
Contrail avoidance options*
Aircraft re-routing
Study microphysical and radiative effects of contrail/natural cirrus
Contrail evolution and prediction
Improve humidity forecast based on ANN and dynamical states
Gierens et al., 2020
Teoh et al., 2022a
Advanced engine technologies and fuels
Reduce soot particles emissions (biofuel, hydrogen, lean burn engine)
Suppress nucleation and growth of crystals (WET engine)
Burkhardt et al., 2018
Voigt et al., 2021
Gierens et al., 2022
* Possibly increased CO2 emissions have to be considered.

Figure 7.2: The sketch for contrail mitigation proposed based on addressing key scientific questions, including detailed assessments of contrail cirrus RF and enhancements in the RHi prediction using the ANN model for weather forecast.

This ANN method, with the better parameterization of ice supersaturation, could improve and consolidate first attempts to avoid contrails in international airlines. In the next step, I would like to test contrail cirrus mitigation strategies encompassing a wider range of scenarios with the CoCiP model. This can include not only variations in water vapor to support contrail growth but also reductions in soot particle emissions for contrail formation. Figure 7.2 presents the summarized contrail mitigation strategies with the aim to reduce the contrail climate forcing in their spreading and formation stage, including (1) a small-scale strategy of diverting flights with the largest contrail ERF, for instance avoiding the ISSRs, based on the investigations of microphysical and radiative effects of contrail and natural cirrus, (2) widespread adoption of aircraft powered by cleaner fuel and engine technologies such as biofuel blending, hydrogen combustion, lean burn engine, and water-enhanced turbofan (WET) engine [Pouzolz et al., 2021].

Besides the correction of ISSRs, other sustainable aviation strategies mentioned above are also applied with CoCiP simulations for the first simple attempt, with the adjustments of soot emissions and available water vapor according to the description in Chapter 6. Figure 7.3 shows the contrail cirrus net RF from modified aircraft emissions and ambient RHi compared to normal conditions as one example. Applications of biofuel blending, hydrogen combustion and WET engine have reduced microphysics (IOT) and absolute net radiative effects of contrail cirrus incrementally. What I haven't shown here from the first

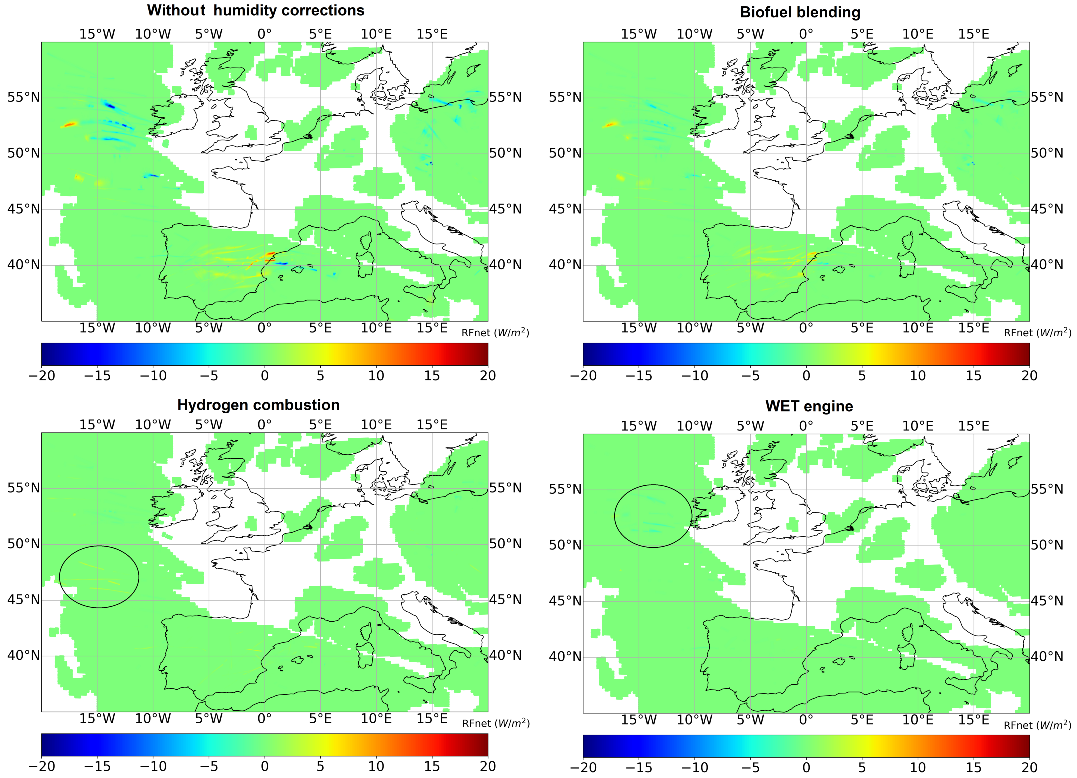

Figure 7.3: Simulations of contrail cirrus net RF pertaining to various contrail mitigation strategies conducted by CoCiP.

simulation results is that the hydrogen combustion has a stronger reduction effect on SW RF of contrail cirrus than on LW RF, and the WET engine contributes to a regional net cooling effect of contrail cirrus. Settings or parametrizations in CoCiP need to be further optimized based on measurements. Possibly increased CO_2 emissions or cost of investment and time have to be discussed when re-scheduling air traffic.

The previous paragraphs clearly show various possibilities to reduce the impact of contrail cirrus on climate. Thus, questions arise: Which is the most suitable option?Grewe and Linke [2017] compared results on the climate impact reduction of operational and technological mitigation options achieved within various projects. For example, AHEAD (a multi-fuel blended wing body) has a large eco-efficiency (ratio between climate impact reduction and operational costs) and hence seems to be well suited to be developed but the potential starting time of this option is far in the future. On the other side, ISO (intermediate stop operations to reduce fuel consumption) actually are already adopted. Yet the goal of the current implementation is rather exploiting cheap fueling possibilities and the eco-efficiency ways. A good strategy should mix different approaches, e.g., operational mitigation measures such as REACT4C (lateral and vertical changes in flight trajectories to avoid climate sensitive regions) or WeCare-CRA (climate restricted areas related to climate sensitive regions), to obtain some reductions in the climate impact from aviation by complementing it with further technology options on the longer term. Obviously, there is no clear answer to these questions, regarding ranking of mitigation options and measures, and further discussions are still ongoing.

The prediction of ice supersaturation in this thesis can also be applied to the investigation of microphysical processes of mixed-phase clouds (MPCs, a mixture of supercooled liquid droplets and ice crystals). Herein, the Wegener–Bergeron–Findeisen process (or "cold-rain process") is predominant, during which ice crystals grow in MPCs with the depletion of liquid droplets in a subsaturated environment for liquid water but a supersaturated environment for ice [Korolev and Mazin, 2003]. Under the condition that the density of ice is smaller compared to liquid water, the ice crystals can grow large enough to fall out of the cloud, melting into rain droplets if lower level temperatures are warm. When the fraction of liquid droplets decreases from 100% to 0, more ice particles in the warming environment will melt to liquid droplets with the higher reflection and let more energy back to the space, and then offset the temperature to decrease about 2 °C. Thus the supercooled liquid fraction (SLF) in MPCs is an essential variable of cloud microphysical processes and climate sensitivity. I have retrieved the SLF in MPCs based on the differences in radiative properties of supercooled liquid droplets and ice particles at visible and shortwave-infrared channels of the geostationary Himawari-8 (Figure 7.4, Wang et al. 2024), thus the retrieval results could be linked with ice supersaturation distribution predicted from the ANN model and meteorological conditions from ECMWF to investigate the evolution of MPCs in the future study.

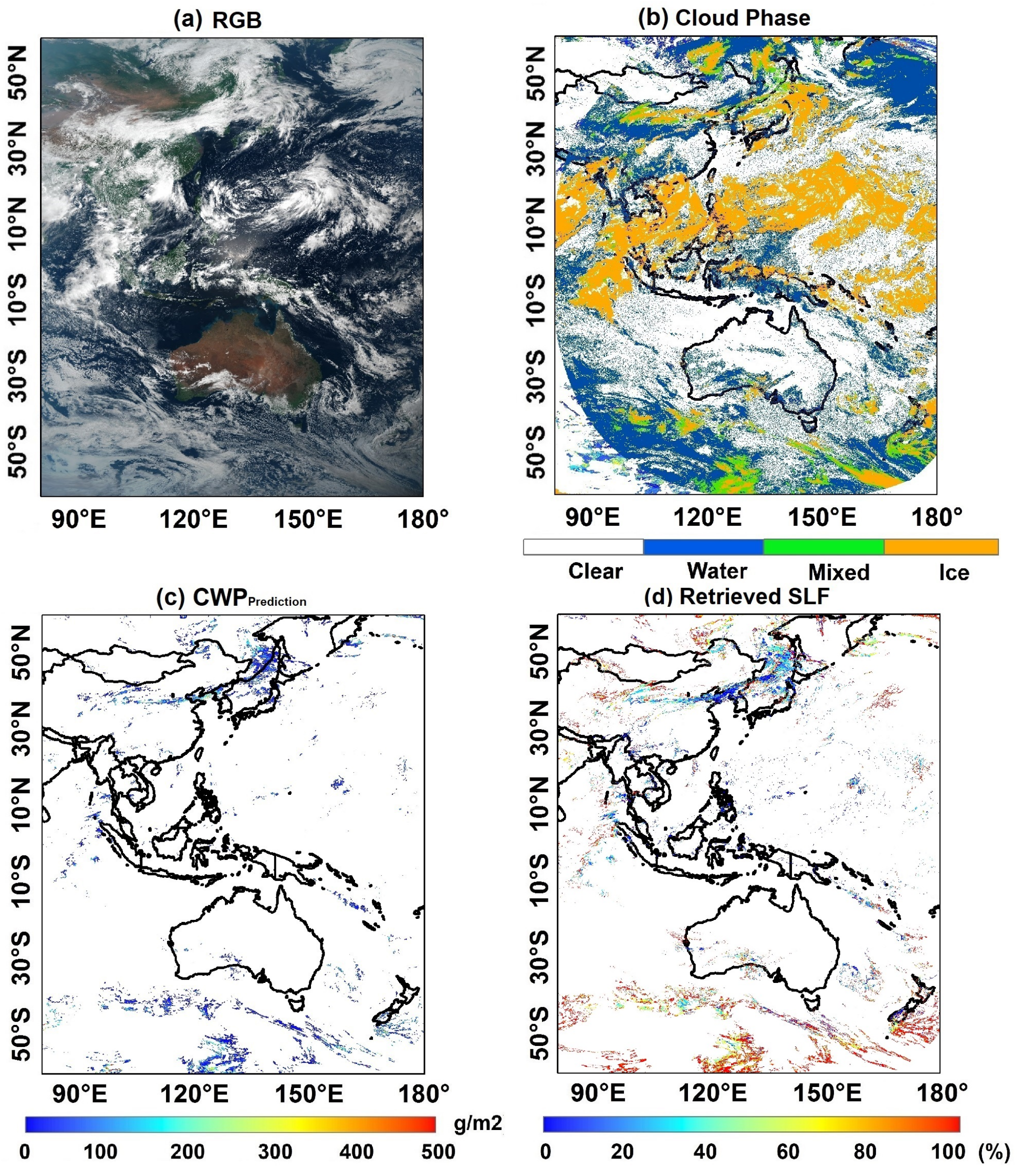
(a) RGB
(b) Cloud Phase
(c) CWP Prediction
(d) Retrieved SLF
50°S
30°S
10°S
10°N
30°N
50°N
90°E
120°E
150°E
180°
Clear
Water
Mixed
Ice
g/m2
0
100
200
300
400
500
0
20
40
60
80
100 (%)

Figure 7.4: The general cloud situation and retrieved SLF in the detected MPCs at 4:00 UTC on 28 August 2017. a. RGB. b. Cloud top phase. c. Cloud water path predicted based on the collocated Himawari-8 and CALIPSO observations. d. SLF in MPCs.

Appendix A

List of abbreviations

ABI	Advanced Baseline Imager
ACTA	Automatic Contrail Tracking Algorithm
AENEAS	AtmosphEric Nitrogen oxides mEAsuring System
agg	aggregates
AI	Artificial Intelligence
AIC	Aircraft-Induced Clouds
AIMS	Atmospheric Ionization Mass Spectrometer
AIRS	Atmospheric InfRared Sounder
ANN	Artificial Neural Networks
AR5	Fifth Assessment Report
AVHRR	Advanced Very High Resolution Radiometer
BADA	Base of Aircraft Data
BAHAMAS	Basis HALO Measurement and Sensor System
BTD	Brightness Temperature Difference
CALIPSO	Cloud Aerosol Lidar and Infrared Pathfinder Satellite Observations
CARIBIC	Civil Aircraft for the Regular Investigation of the atmosphere Based on an Instrument Container
CAS-DPOL	Cloud and Aerosol Spectrometer with Detector for Polarization
CBH	Cirrus Bottom Height
CC	Correlation Coefficient
CDA	Contrail Detection Algorithm
CERES	Clouds and the Earth's Radiant Energy System
CIP	Cloud Imaging Probe
CiPS	Cirrus Properties from SEVIRI
CO_2	Carbon Dioxide
CoCiP	Contrail Cirrus Prediction model

CONCERT	CONtrail and Cirrus ExpeRimenT
CTH	Cloud Top Height
ECMWF	European Centre for Medium-Range Weather Forecasts
ERA5	Fifth generation ECMWF ReAnalysis
EF	Energy Forcing
ERF	Effective Radiative Forcing
ETS	Equitable Threat Score
ghm	general habit mixture
GERB	Geostationary Earth Radiation Budget
HALO	High Altitude and LOng range research aircraft
HRV	High Resolution Visible
IAGOS	In-Service Aircraft for Global Observing System
ICE	International Cirrus Experiment
IFS	Integrated Forecast System
IOT	Ice Optical Thickness
IPCC	Intergovernmental Panel on Climate Change
ISSRs	Ice Supersaturation Regions
IWC	Ice Water Content
LWC	Liquid Water Content
LMS	LowerMost Stratosphere
LW	LongWave
MAE	Mean Absolute Error
MBPE	Mean Bias Percentage Error
MSE	Mean Squared Error
MSG	Meteosat Second Generation
ML-CIRRUS	Midlatitude Cirrus
MLP	MultiLayer Perceptron
MODIS	Moderate Resolution Imaging Spectroradiometer
MOZAIC	Measurement of Ozone and Water Vapor by Airbus In-Service Aircraft
MPCs	Mixed-Phase Clouds
NAR	North Atlantic Region
NATS	North Atlantic Tracks
NO	Nitrogen Oxide
NO$_x$	Nitrogen Oxides
nvPM	non-volatile Particulate Matter
NWP	Numerical Weather Prediction
OLR	Outgoing Longwave Radiation
R2	R-Square
R_{eff}	Effective Radii
ReLU	Rectified Linear Unit
RF	Radiative Forcing

RGB	Red Green Blue image
RHi	Ice Supersaturation Regions
RMSE	Root Mean Square Error
RRUMS	Rapid Retrieval of Upwelling Irradiances from MSG/SEVIRI
RSR	Reflective Solar Radiation
RTM	Radiative Transfer Model
SAC	Schmidt-Appleman Criterion
SEVIRI	Spinning Enhanced Visible and InfraRed Imager
SLF	Supercooled Liquid Fraction
SW	ShortWave
TOA	Top-Of-Atmosphere
TTL	Tropical Tropopause Layer
UTLS	Upper Troposphere and Lower Stratosphere
WALES	Water vapor Lidar Experiment in Space

List of Figures

1.1 Structures of contrail cirrus from a satellite image 1
1.2 Climate forcing terms from global aviation 2
1.3 Origins of model humidity bias 4
1.4 The variation of contrail cirrus net RF induced from humidity correction . 5

2.1 Atmospheric window 11
2.2 Angular distributions of visible radiation at 0.5 µm by spherical particles of three sizes 12
2.3 Processes influencing the contrail formation stage 16
2.4 Classification of aircraft wake evolution into four regimes 17
2.5 Zonal means of ice supersaturation occurrence frequencies from AIRS . . . 24
2.6 Vertical profiles of RHi for IAGOS and ERA 26
2.7 Radiative effects of the enhanced mixing simulation for water vapor 26
2.8 The structure of an artificial neural network 29

3.1 Coverage with the SEVIRI sensor on the MSG satellites 34
3.2 Cumulative distribution of RHi in the IAGOS and ERA data sets. 37
3.3 Distribution of natural cirrus and contrail cirrus from CoCiP simulations . 41

4.1 The general situation of the contrail cirrus outbreak 45
4.2 Time series of contrail cirrus and surrounding clouds from MSG/SEVIRI observations 46
4.3 Three lidar legs with backscatter ratios at 1064 nm and 532 nm 48
4.4 RHi from three lidar legs in Figure 4.3 49
4.5 In situ measurements from the research aircraft HALO 51
4.6 Histograms of in situ measured N_{ice} and ΔNO 53
4.7 R_{eff} of natural cirrus, contrail cirrus and contrails from HALO in situ measurements 54
4.8 Comparison of TOA RSR and OLR from RRUMS algorithm results and revised-GERB data sets 56
4.9 Structure of input data in the forward RTM simulations using LibRadtran 57
4.10 Comparison of TOA RSR and OLR from RTM simulations and RRUMS algorithm results 59

4.11 Diurnal cycle of cirrus macrophysical and microphysical properties, and radiative effects . . . 60

5.1 Schematic framework of meteorological variables selection, humidity prediction model building, and model interpretation and evaluation . . . 64
5.2 Comparisons of temperature from ERA5 and IAGOS in the UTLS . . . 66
5.3 Comparisons of RHi from ERA5 and IAGOS in the UTLS . . . 67
5.4 Temporal dependence of the measured RHi on the modelled thermodynamic and dynamical variables . . . 69
5.5 Distributions of input variables from ERA5 and target RHi from IAGOS . 71
5.6 Relative contributions of multiple variables to humidity predictions . . . 73
5.7 Overall test of specific humidity in the UTLS from ERA5 and the ANN model 76
5.8 Overall test of RHi in the UTLS from ERA5 and the ANN model . . . 77
5.9 Overall accuracy of humidities against IAGOS measurements in the UTLS from ERA5 and the ANN model . . . 78
5.10 Comparisons of RHi from ERA5 and the ANN model against independent aircraft measurements . . . 79
5.11 The contingency table used for the evaluation of ISSRs prediction . . . 80
5.12 Water vapor number density from ERA5 or the ANN model and the differences 82
5.13 TOA RSR and OLR from RTM simulations using the humidity from ERA5 or the ANN model and the comparison with ERA5 radiation products . . . 82
5.14 Atmospheric heating rate profiles influenced by the humidity from ERA5 or the ANN model and the variations . . . 83
5.15 Overall accuracy of specific humidity from ERA5 and the ANN model against IAGOS measurements in other geographic regions . . . 84

6.1 Satellite images of contrail cirrus . . . 88
6.2 Comparisons of contrail cirrus derived from CoCiP simulations using humidity from ECMWF IFS and the ANN model . . . 89
6.3 Distributions of IOT simulated from the CoCiP model without or with humidity improvement and retrieved from MSG observations . . . 91
6.4 Occurrences of IOT simulated from the CoCiP model without or with humidity improvement and retrieved from MSG observations . . . 91
6.5 Distributions of RSR and OLR simulated from the CoCiP model without or with humidity improvement and retrieved from MSG observations . . . 92
6.6 Occurrences of RSR and OLR simulated from the CoCiP model without or with humidity improvement and retrieved from MSG observations . . . 92
6.7 The concept of the contrail climate impact mitigation with small scale diversion strategy . . . 93

7.1 The sketch of this research . . . 100
7.2 The sketch for contrail mitigation strategies . . . 102

7.3 Simulations of contrail cirrus net RF pertaining to various contrail mitigation strategies 103
7.4 The general cloud situation and retrieved supercooled liquid fraction from Himawari-8 105

List of Tables

4.1 Cirrus classification based on aircraft measurements 52
4.2 The sensitivities of cirrus radiative effects to R_{eff} and assumed crystal shapes 61

5.1 Overview of the used variables in humidity improvement from ERA5 and IAGOS 65
5.2 Recorded ETS values for the prediction of ISSRs from ERA5 and the ANN model 81

Bibliography

A. F. Agarap. Deep learning using rectified linear units (relu). *arXiv preprint arXiv:1803.08375*, 2018.

H. Appleman. The formation of exhaust condensation trails by jet aircraft. *Bulletin of the American Meteorological Society*, 34(1):14 – 20, 1953. doi: https://doi.org/10.1175/1520-0477-34.1.14.

D. Atlas, Z. Wang, and D. P. Duda. Contrails to cirrus—morphology, microphysics, and radiative properties. *Journal of Applied Meteorology and Climatology*, 45(1):5 – 19, 2006. doi: https://doi.org/10.1175/JAM2325.1.

P. Bauer, A. Thorpe, and G. Brunet. The quiet revolution of numerical weather prediction. *Nature*, 525:47–55, 2015. doi: https://doi.org/10.1038/nature14956.

B. A. Baum, P. Yang, A. J. Heymsfield, A. Bansemer, B. H. Cole, A. Merrelli, C. Schmitt, and C. Wang. Ice cloud single-scattering property models with the full phase matrix at wavelengths from 0.2 to 100µm. *Journal of Quantitative Spectroscopy and Radiative Transfer*, 146:123–139, 2014. ISSN 0022-4073. doi: https://doi.org/10.1016/j.jqsrt.2014.02.029. Electromagnetic and Light Scattering by Nonspherical Particles XIV.

D. Baumgardner, J. Brenguier, A. Bucholtz, H. Coe, P. DeMott, T. Garrett, J. Gayet, M. Hermann, A. Heymsfield, A. Korolev, M. Krämer, A. Petzold, W. Strapp, P. Pilewskie, J. Taylor, C. Twohy, M. Wendisch, W. Bachalo, and P. Chuang. Airborne instruments to measure atmospheric aerosol particles, clouds and radiation: A cook's tour of mature and emerging technology. *Atmospheric Research*, 102(1):10–29, 2011. ISSN 0169-8095. doi: https://doi.org/10.1016/j.atmosres.2011.06.021.

D. Baumgardner, S. J. Abel, D. Axisa, R. Cotton, J. Crosier, P. Field, C. Gurganus, A. Heymsfield, A. Korolev, M. Krämer, P. Lawson, G. McFarquhar, Z. Ulanowski, and J. Um. Cloud ice properties: In situ measurement challenges. *Meteorological Monographs*, 58:9.1 – 9.23, 2017. doi: https://doi.org/10.1175/AMSMONOGRAPHS-D-16-0011.1.

F. Berkes, P. Neis, M. G. Schultz, U. Bundke, S. Rohs, H. G. J. Smit, A. Wahner, P. Konopka, D. Boulanger, P. Nédélec, V. Thouret, and A. Petzold. In situ temperature measurements in the upper troposphere and lowermost stratosphere from 2 decades of iagos long-term routine observation. *Atmospheric Chemistry and Physics*, 17(20): 12495–12508, 2017. doi: 10.5194/acp-17-12495-2017.

M. Bickel, M. Ponater, L. Bock, U. Burkhardt, and S. Reineke. Estimating the effective radiative forcing of contrail cirrus. *Journal of Climate*, 33(5):1991 – 2005, 2020. doi: https://doi.org/10.1175/JCLI-D-19-0467.1.

A. Bier and U. Burkhardt. Impact of parametrizing microphysical processes in the jet and vortex phase on contrail cirrus properties and radiative forcing. *Journal of Geophysical Research: Atmospheres*, 127(23):e2022JD036677, 2022. doi: https://doi.org/10.1029/2022JD036677.

A. Bier, U. Burkhardt, and L. Bock. Synoptic control of contrail cirrus life cycles and their modification due to reduced soot number emissions. *Journal of Geophysical Research: Atmospheres*, 122(21):11,584–11,603, 2017. doi: https://doi.org/10.1002/2017JD027011.

C. M. Bishop. *Neural Networks for Pattern Recognition.* Clarendon Press, Oxford, United Kingdom, 1995. ISBN 9780198538646.

L. Bock and U. Burkhardt. The temporal evolution of a long-lived contrail cirrus cluster: Simulations with a global climate model. *Journal of Geophysical Research: Atmospheres*, 121(7):3548–3565, 2016a. doi: https://doi.org/10.1002/2015JD024475.

L. Bock and U. Burkhardt. Reassessing properties and radiative forcing of contrail cirrus using a climate model. *Journal of Geophysical Research: Atmospheres*, 121(16):9717–9736, 2016b. doi: https://doi.org/10.1002/2016JD025112.

L. Bock and U. Burkhardt. Contrail cirrus radiative forcing for future air traffic. *Atmospheric Chemistry and Physics*, 19(12):8163–8174, 2019. doi: 10.5194/acp-19-8163-2019.

R. C. Braga, D. Rosenfeld, R. Weigel, T. Jurkat, M. O. Andreae, M. Wendisch, M. L. Pöhlker, T. Klimach, U. Pöschl, C. Pöhlker, C. Voigt, C. Mahnke, S. Borrmann, R. I. Albrecht, S. Molleker, D. A. Vila, L. A. T. Machado, and P. Artaxo. Comparing parameterized versus measured microphysical properties of tropical convective cloud bases during the acridicon–chuva campaign. *Atmospheric Chemistry and Physics*, 17(12):7365–7386, 2017a. doi: 10.5194/acp-17-7365-2017.

R. C. Braga, D. Rosenfeld, R. Weigel, T. Jurkat, M. O. Andreae, M. Wendisch, U. Pöschl, C. Voigt, C. Mahnke, S. Borrmann, R. I. Albrecht, S. Molleker, D. A. Vila, L. A. T. Machado, and L. Grulich. Further evidence for ccn aerosol concentrations determining the height of warm rain and ice initiation in convective clouds over the amazon basin. *Atmospheric Chemistry and Physics*, 17(23):14433–14456, 2017b. doi: 10.5194/acp-17-14433-2017.

T. Bräuer, C. Voigt, D. Sauer, S. Kaufmann, V. Hahn, M. Scheibe, H. Schlager, F. Huber, P. Le Clercq, R. H. Moore, and B. E. Anderson. Reduced ice number concentrations in contrails from low-aromatic biofuel blends. *Atmospheric Chemistry and Physics*, 21(22): 16817–16826, 2021. doi: 10.5194/acp-21-16817-2021.

S. Buehler, V. John, A. Kottayil, M. Milz, and P. Eriksson. Efficient radiative transfer simulations for a broadband infrared radiometer—combining a weighted mean of representative frequencies approach with frequency selection by simulated annealing. *Journal of Quantitative Spectroscopy and Radiative Transfer*, 111(4):602–615, 2010. ISSN 0022-4073. doi: https://doi.org/10.1016/j.jqsrt.2009.10.018.

L. Bugliaro, T. Zinner, C. Keil, B. Mayer, R. Hollmann, M. Reuter, and W. Thomas. Validation of cloud property retrievals with simulated satellite radiances: a case study for seviri. *Atmospheric Chemistry and Physics*, 11(12):5603–5624, 2011. doi: 10.5194/acp-11-5603-2011.

L. Bugliaro, D. Piontek, S. Kox, M. Schmidl, B. Mayer, R. Müller, M. Vázquez-Navarro, D. M. Peters, R. G. Grainger, J. Gasteiger, and J. Kar. Vadugs: a neural network for the remote sensing of volcanic ash with msg/seviri trained with synthetic thermal satellite observations simulated with a radiative transfer model. *Natural Hazards and Earth System Sciences*, 22(3):1029–1054, 2022. doi: 10.5194/nhess-22-1029-2022.

U. Burkhardt and B. Kärcher. Process-based simulation of contrail cirrus in a global climate model. *Journal of Geophysical Research: Atmospheres*, 114(D16), 2009. doi: https://doi.org/10.1029/2008JD011491.

U. Burkhardt and B. Kärcher. Global radiative forcing from contrail cirrus. *Nature Climate Change*, 2011.

U. Burkhardt, L. Bock, and A. Bier. Mitigating the contrail cirrus climate impact by reducing aircraft soot number emissions. *npj Climate and Atmospheric Science*, 2018.

M. Cain, J. Lynch, M. R. Allen, J. S. Fuglestvedt, D. J. Frame, and A. H. Macey. Improved calculation of warming-equivalent emissions for short-lived climate pollutants. *NPJ climate and atmospheric science*, 2(1):29, 2019. doi: https://doi.org/10.1038/s41612-019-0086-4.

A. M. Carleton, D. J. Travis, K. Master, and S. Vezhapparambu. Composite atmospheric environments of jet contrail outbreaks for the united states. *Journal of Applied Meteorology and Climatology*, 47(2):641 – 667, 2008. doi: https://doi.org/10.1175/2007JAMC1481.1.

T. N. Carlson. Mid-latitude weather systems by t. n. carlson. *Weather*, 48(2):46–46, 1993. doi: https://doi.org/10.1002/j.1477-8696.1993.tb07226.x.

A. Chauvigné, O. Jourdan, A. Schwarzenboeck, C. Gourbeyre, J. F. Gayet, C. Voigt, H. Schlager, S. Kaufmann, S. Borrmann, S. Molleker, A. Minikin, T. Jurkat, and U. Schumann. Statistical analysis of contrail to cirrus evolution during the contrail and cirrus experiment (concert). *Atmospheric Chemistry and Physics*, 18(13):9803–9822, 2018. doi: 10.5194/acp-18-9803-2018.

C.-C. Chen, A. Gettelman, C. Craig, P. Minnis, and D. P. Duda. Global contrail coverage simulated by cam5 with the inventory of 2006 global aircraft emissions. *Journal of Advances in Modeling Earth Systems*, 4(2), 2012. doi: https://doi.org/10.1029/2011MS000105.

N. Clerbaux, J. Russell, S. Dewitte, C. Bertrand, D. Caprion, B. De Paepe, L. Gonzalez Sotelino, A. Ipe, R. Bantges, and H. Brindley. Comparison of gerb instantaneous radiance and flux products with ceres edition-2 data. *Remote Sensing of Environment*, 113(1): 102–114, 2009. ISSN 0034-4257. doi: https://doi.org/10.1016/j.rse.2008.08.016.

C. Cox and W. Munk. Measurement of the roughness of the sea surface from photographs of the sun's glitter. *J. Opt. Soc. USA*, 44:838–850, 1954a.

C. Cox and W. Munk. Statistics of the sea surface derived from sun glitter. *J. Mar. Res.*, 13:198–227, 1954b.

M. de Reus, S. Borrmann, A. Bansemer, A. J. Heymsfield, R. Weigel, C. Schiller, V. Mitev, W. Frey, D. Kunkel, A. Kürten, J. Curtius, N. M. Sitnikov, A. Ulanovsky, and F. Ravegnani. Evidence for ice particles in the tropical stratosphere from in-situ measurements. *Atmospheric Chemistry and Physics*, 9(18):6775–6792, 2009. doi: 10.5194/acp-9-6775-2009.

D. P. Dee, S. M. Uppala, A. J. Simmons, P. Berrisford, P. Poli, S. Kobayashi, U. Andrae, M. A. Balmaseda, G. Balsamo, P. Bauer, P. Bechtold, A. C. M. Beljaars, L. van de Berg, J. Bidlot, N. Bormann, C. Delsol, R. Dragani, M. Fuentes, A. J. Geer, L. Haimberger, S. B. Healy, H. Hersbach, E. V. Hólm, L. Isaksen, P. Kållberg, M. Köhler, M. Matricardi, A. P. McNally, B. M. Monge-Sanz, J.-J. Morcrette, B.-K. Park, C. Peubey, P. de Rosnay, C. Tavolato, J.-N. Thépaut, and F. Vitart. The era-interim reanalysis: configuration and performance of the data assimilation system. *Quarterly Journal of the Royal Meteorological Society*, 137(656):553–597, 2011. doi: https://doi.org/10.1002/qj.828.

G. Dekoutsidis, S. Groß, M. Wirth, M. Krämer, and C. Rolf. Characteristics of supersaturation in midlatitude cirrus clouds and their adjacent cloud-free air. *Atmospheric Chemistry and Physics*, 23(5):3103–3117, 2023. doi: 10.5194/acp-23-3103-2023.

N. C. Dickson, K. M. Gierens, H. L. Rogers, and R. L. Jones. Probabilistic description of ice-supersaturated layers in low resolution profiles of relative humidity. *Atmospheric Chemistry and Physics*, 10(14):6749–6763, 2010. doi: 10.5194/acp-10-6749-2010.

D. P. Duda, P. Minnis, and L. Nguyen. Estimates of cloud radiative forcing in contrail clusters using goes imagery. *Journal of Geophysical Research: Atmospheres*, 106(D5): 4927–4937, 2001. doi: https://doi.org/10.1029/2000JD900393.

D. P. Duda, P. Minnis, K. Khlopenkov, T. L. Chee, and R. Boeke. Estimation of 2006 northern hemisphere contrail coverage using modis data. *Geophysical Research Letters*, 40(3):612–617, 2013. doi: https://doi.org/10.1002/grl.50097.

C. Dyroff, A. Zahn, E. Christner, R. Forbes, A. M. Tompkins, and P. F. J. van Velthoven. Comparison of ecmwf analysis and forecast humidity data with caribic upper troposphere and lower stratosphere observations. *Quarterly Journal of the Royal Meteorological Society*, 141(688):833–844, 2015. doi: https://doi.org/10.1002/qj.2400.

D. Efremenko and A. Kokhanovsky. *Light Scattering, Absorption, Extinction, and Propagation in the Terrestrial Atmosphere*, pages 77–147. Springer International Publishing, Cham, 2021. ISBN 978-3-030-66745-0. doi: 10.1007/978-3-030-66745-0_3.

C. Emde, R. Buras-Schnell, A. Kylling, B. Mayer, J. Gasteiger, U. Hamann, J. Kylling, B. Richter, C. Pause, T. Dowling, and L. Bugliaro. The libradtran software package for radiative transfer calculations (version 2.0.1). *Geoscientific Model Development*, 9(5): 1647–1672, 2016. doi: 10.5194/gmd-9-1647-2016.

A. Filges, C. Gerbig, H. Chen, H. Franke, C. Klaus, and A. Jordan. The iagos-core greenhouse gas package: a measurement system for continuous airborne observations of co2, ch4, h2o and co. *Tellus B: Chemical and Physical Meteorology*, Jan 2015. doi: 10.3402/tellusb.v67.27989.

M. A. Fischler and R. C. Bolles. Random sample consensus: A paradigm for model fitting with applications to image analysis and automated cartography. *Commun. ACM*, 24(6): 381–395, jun 1981. ISSN 0001-0782. doi: 10.1145/358669.358692.

P. M. Forster and K. P. Shine. Stratospheric water vapour changes as a possible contributor to observed stratospheric cooling. *Geophysical Research Letters*, 26(21):3309–3312, 1999. doi: https://doi.org/10.1029/1999GL010487.

Q. Fu and K. N. Liou. On the correlated k-distribution method for radiative transfer in nonhomogeneous atmospheres. *Journal of Atmospheric Sciences*, 49(22):2139 – 2156, 1992. doi: https://doi.org/10.1175/1520-0469(1992)049<2139:OTCDMF>2.0.CO;2.

M. Gardner and S. Dorling. Artificial neural networks (the multilayer perceptron)—a review of applications in the atmospheric sciences. *Atmospheric Environment*, 32(14): 2627–2636, 1998. ISSN 1352-2310. doi: https://doi.org/10.1016/S1352-2310(97)00447-0.

J. Gasteiger, C. Emde, B. Mayer, R. Buras, S. Buehler, and O. Lemke. Representative wavelengths absorption parameterization applied to satellite channels and spectral bands. *Journal of Quantitative Spectroscopy and Radiative Transfer*, 148:99–115, 2014. ISSN 0022-4073. doi: https://doi.org/10.1016/j.jqsrt.2014.06.024.

J.-F. Gayet, G. Febvre, G. Brogniez, H. Chepfer, W. Renger, and P. Wendling. Microphysical and optical properties of cirrus and contrails: Cloud field study on 13 october 1989. *Journal of Atmospheric Sciences*, 53(1):126 – 138, 1996. doi: https://doi.org/10.1175/1520-0469(1996)053<0126:MAOPOC>2.0.CO;2.

J.-F. Gayet, V. Shcherbakov, C. Voigt, U. Schumann, D. Schäuble, P. Jessberger, A. Petzold, A. Minikin, H. Schlager, O. Dubovik, and T. Lapyonok. The evolution of microphysical and optical properties of an a380 contrail in the vortex phase. *Atmospheric Chemistry and Physics*, 12(14):6629–6643, 2012. doi: 10.5194/acp-12-6629-2012.

T. Gerz, T. Dürbeck, and P. Konopka. Transport and effective diffusion of aircraft emissions. *Journal of Geophysical Research: Atmospheres*, 103(D20):25905–25913, 1998. doi: https://doi.org/10.1029/98JD02282.

A. Gettelman, X. Liu, S. J. Ghan, H. Morrison, S. Park, A. J. Conley, S. A. Klein, J. Boyle, D. L. Mitchell, and J.-L. F. Li. Global simulations of ice nucleation and ice supersaturation with an improved cloud scheme in the community atmosphere model. *Journal of Geophysical Research: Atmospheres*, 115(D18), 2010. doi: https://doi.org/10.1029/2009JD013797.

A. Gettelman, C.-C. Chen, and C. G. Bardeen. The climate impact of covid-19-induced contrail changes. *Atmospheric Chemistry and Physics*, 21(12):9405–9416, 2021. doi: 10.5194/acp-21-9405-2021.

K. Gierens and S. Brinkop. Dynamical characteristics of ice supersaturated regions. *Atmospheric Chemistry and Physics*, 12(24):11933–11942, 2012. doi: 10.5194/acp-12-11933-2012.

K. Gierens and P. Spichtinger. On the size distribution of ice-supersaturated regions in the upper troposphere and lowermost stratosphere. *Annales Geophysicae*, 18(4):499–504, 2000. doi: 10.1007/s00585-000-0499-7.

K. Gierens, S. Matthes, and S. Rohs. How well can persistent contrails be predicted? *Aerospace*, 7(12), 2020. ISSN 2226-4310. doi: 10.3390/aerospace7120169.

K. Graf, U. Schumann, H. Mannstein, and B. Mayer. Aviation induced diurnal north atlantic cirrus cover cycle. *Geophysical Research Letters*, 39(16):L16804, 2012. doi: https://doi.org/10.1029/2012GL052590.

V. Grewe and F. Linke. Eco-efficiency in aviation. *Meteorologische Zeitschrift*, 26(6): 689–696, 12 2017. doi: 10.1127/metz/2017/0762.

V. Grewe, K. Dahlmann, J. Flink, C. Frömming, R. Ghosh, K. Gierens, R. Heller, J. Hendricks, P. Jöckel, S. Kaufmann, K. Kölker, F. Linke, T. Luchkova, B. Lührs, J. Van Manen, S. Matthes, A. Minikin, M. Niklaß, M. Plohr, M. Righi, S. Rosanka, A. Schmitt, U. Schumann, I. Terekhov, S. Unterstrasser, M. Vázquez-Navarro, C. Voigt, K. Wicke, H. Yamashita, A. Zahn, and H. Ziereis. Mitigating the climate impact from aviation: Achievements and results of the dlr wecare project. *Aerospace*, 4(3), 2017. ISSN 2226-4310. doi: 10.3390/aerospace4030034.

S. Groß, M. Wirth, A. Schäfler, A. Fix, S. Kaufmann, and C. Voigt. Potential of airborne lidar measurements for cirrus cloud studies. *Atmospheric Measurement Techniques*, 7 (8):2745–2755, 2014. doi: 10.5194/amt-7-2745-2014.

J. E. Hansen and L. D. Travis. Light scattering in planetary atmospheres. *Space Science Reviews*, 16:527–610, 1974. doi: https://doi.org/10.1007/BF00168069.

J. E. Harries, J. E. Russell, J. A. Hanafin, H. Brindley, J. Futyan, J. Rufus, S. Kellock, G. Matthews, R. Wrigley, A. Last, J. Mueller, R. Mossavati, J. Ashmall, E. Sawyer, D. Parker, M. Caldwell, P. M. Allan, A. Smith, M. J. Bates, B. Coan, B. C. Stewart, D. R. Lepine, L. A. Cornwall, D. R. Corney, M. J. Ricketts, D. Drummond, D. Smart, R. Cutler, S. Dewitte, N. Clerbaux, L. Gonzalez, A. Ipe, C. Bertrand, A. Joukoff, D. Crommelynck, N. Nelms, D. T. Llewellyn-Jones, G. Butcher, G. L. Smith, Z. P. Szewczyk, P. E. Mlynczak, A. Slingo, R. P. Allan, and M. A. Ringer. The geostationary earth radiation budget project. *Bulletin of the American Meteorological Society*, 86(7): 945 – 960, 2005. doi: https://doi.org/10.1175/BAMS-86-7-945.

J. M. Haywood, R. P. Allan, J. Bornemann, P. M. Forster, P. N. Francis, S. Milton, G. Rädel, A. Rap, K. P. Shine, and R. Thorpe. A case study of the radiative forcing of persistent contrails evolving into contrail-induced cirrus. *Journal of Geophysical Research: Atmospheres*, 114(D24):D24201, 2009. doi: https://doi.org/10.1029/2009JD012650.

M. I. Hegglin, D. A. Plummer, T. G. Shepherd, J. F. Scinocca, J. Anderson, L. Froidevaux, B. Funke, D. F. Hurst, A. Rozanov, J. Urban, T. von Clarmann, K. A. Walker, H. J. R. Wang, S. Tegtmeier, and K. Weigel. Vertical structure of stratospheric water vapour trends derived from merged satellite data. *Nature geoscience*, 7:768–776, 2014. doi: https://doi.org/10.1038/ngeo2236.

H. Hersbach, B. Bell, P. Berrisford, S. Hirahara, A. Horányi, J. Muñoz-Sabater, J. Nicolas, C. Peubey, R. Radu, D. Schepers, A. Simmons, C. Soci, S. Abdalla, X. Abellan, G. Balsamo, P. Bechtold, G. Biavati, J. Bidlot, M. Bonavita, G. De Chiara, P. Dahlgren, D. Dee, M. Diamantakis, R. Dragani, J. Flemming, R. Forbes, M. Fuentes, A. Geer, L. Haimberger, S. Healy, R. J. Hogan, E. Hólm, M. Janisková, S. Keeley, P. Laloyaux, P. Lopez, C. Lupu, G. Radnoti, P. de Rosnay, I. Rozum, F. Vamborg, S. Villaume, and J.-N. Thépaut. The era5 global reanalysis. *Quarterly Journal of the Royal Meteorological Society*, 146(730):1999–2049, 2020. doi: https://doi.org/10.1002/qj.3803.

A. Heymsfield, D. Baumgardner, P. DeMott, P. Forster, K. Gierens, and B. Kärcher. Contrail microphysics. *Bulletin of the American Meteorological Society*, 91(4):465 – 472, 2010a. doi: https://doi.org/10.1175/2009BAMS2839.1.

A. J. Heymsfield, P. C. Kennedy, S. Massie, C. Schmitt, Z. Wang, S. Haimov, and A. Rangno. Aircraft-induced hole punch and canal clouds: Inadvertent cloud seeding. *Bulletin of the American Meteorological Society*, 91(6):753 – 766, 2010b. doi: https://doi.org/10.1175/2009BAMS2905.1.

J. P. Hoffman, T. F. Rahmes, A. J. Wimmers, and W. F. Feltz. The application of a convolutional neural network for the detection of contrails in satellite imagery. *Remote Sensing*, 15(11), 2023. ISSN 2072-4292. doi: 10.3390/rs15112854.

Y. Hong and G. Liu. The characteristics of ice cloud properties derived from cloudsat and calipso measurements. *Journal of Climate*, 28(9):3880 – 3901, 2015. doi: https://doi.org/10.1175/JCLI-D-14-00666.1.

K. Hornik, M. Stinchcombe, and H. White. Multilayer feedforward networks are universal approximators. *Neural Networks*, 2(5):359–366, 1989. ISSN 0893-6080. doi: https://doi.org/10.1016/0893-6080(89)90020-8.

W. W. Hsieh and B. Tang. Applying neural network models to prediction and data analysis in meteorology and oceanography. *Bulletin of the American Meteorological Society*, 79(9): 1855 – 1870, 1998. doi: https://doi.org/10.1175/1520-0477(1998)079<1855:ANNMTP>2.0.CO;2.

H. Iwabuchi, P. Yang, K. N. Liou, and P. Minnis. Physical and optical properties of persistent contrails: Climatology and interpretation. *Journal of Geophysical Research: Atmospheres*, 117(D6), 2012. doi: https://doi.org/10.1029/2011JD017020.

E. J. Jensen, A. S. Ackerman, D. E. Stevens, O. B. Toon, and P. Minnis. Spreading and growth of contrails in a sheared environment. *Journal of Geophysical Research: Atmospheres*, 103(D24):31557–31567, 1998. doi: https://doi.org/10.1029/98JD02594.

E. J. Jensen, P. Lawson, B. Baker, B. Pilson, Q. Mo, A. J. Heymsfield, A. Bansemer, T. P. Bui, M. McGill, D. Hlavka, G. Heymsfield, S. Platnick, G. T. Arnold, and S. Tanelli. On the importance of small ice crystals in tropical anvil cirrus. *Atmospheric Chemistry and Physics*, 9(15):5519–5537, 2009. doi: 10.5194/acp-9-5519-2009.

P. Jeßberger, C. Voigt, U. Schumann, I. Sölch, H. Schlager, S. Kaufmann, A. Petzold, D. Schäuble, and J.-F. Gayet. Aircraft type influence on contrail properties. *Atmospheric Chemistry and Physics*, 13(23):11965–11984, 2013. doi: 10.5194/acp-13-11965-2013.

J. Jiang and M. Razeghi. Chapter 4 - gainas(p) based qwips on gaas, inp, and si substrates for focal plane arrays. In M. Henini and M. Razeghi, editors, *Handbook of Infra-red Detection Technologies*, pages 121–158. Elsevier Science, Amsterdam, 2002. ISBN 978-1-85617-388-9. doi: https://doi.org/10.1016/B978-185617388-9/50004-6.

T. Jurkat, C. Voigt, F. Arnold, H. Schlager, J. Kleffmann, H. Aufmhoff, D. Schäuble, M. Schaefer, and U. Schumann. Measurements of hono, no, noy and so2 in aircraft exhaust plumes at cruise. *Geophysical Research Letters*, 38(10):L10807, 2011. doi: https://doi.org/10.1029/2011GL046884.

C. Kadow, D. M. Hall, and U. Ulbrich. Artificial intelligence reconstructs missing climate information. *Nature Geoscience*, 2020.

S. Kato, T. P. Ackerman, J. H. Mather, and E. E. Clothiaux. The k-distribution method and correlated-k approximation for a shortwave radiative transfer model. *Journal of Quantitative Spectroscopy and Radiative Transfer*, 62(1):109–121, 1999. ISSN 0022-4073. doi: https://doi.org/10.1016/S0022-4073(98)00075-2.

S. Kaufmann, C. Voigt, T. Jurkat, T. Thornberry, D. W. Fahey, R.-S. Gao, R. Schlage, D. Schäuble, and M. Zöger. The airborne mass spectrometer aims – part 1: Aims-h_2o for utls water vapor measurements. *Atmospheric Measurement Techniques*, 9(3):939–953, 2016. doi: 10.5194/amt-9-939-2016.

S. Kaufmann, C. Voigt, R. Heller, T. Jurkat-Witschas, M. Krämer, C. Rolf, M. Zöger, A. Giez, B. Buchholz, V. Ebert, T. Thornberry, and U. Schumann. Intercomparison of midlatitude tropospheric and lower-stratospheric water vapor measurements and comparison to ecmwf humidity data. *Atmospheric Chemistry and Physics*, 18(22):16729–16745, 2018. doi: 10.5194/acp-18-16729-2018.

C. Kiemle, M. Wirth, A. Fix, G. Ehret, U. Schumann, T. Gardiner, C. Schiller, N. Sitnikov, and G. Stiller. First airborne water vapor lidar measurements in the tropical upper troposphere and mid-latitudes lower stratosphere: accuracy evaluation and intercomparisons with other instruments. *Atmospheric Chemistry and Physics*, 8(17):5245–5261, 2008. doi: 10.5194/acp-8-5245-2008.

M. King, Y. Kaufman, W. Menzel, and D. Tanre. Remote sensing of cloud, aerosol, and water vapor properties from the moderate resolution imaging spectrometer (modis). *IEEE Transactions on Geoscience and Remote Sensing*, 30(1):2–27, 1992. doi: 10.1109/36.124212.

J. Kleine, C. Voigt, D. Sauer, H. Schlager, M. Scheibe, T. Jurkat-Witschas, S. Kaufmann, B. Kärcher, and B. E. Anderson. In situ observations of ice particle losses in a young persistent contrail. *Geophysical Research Letters*, 45(24):13,553–13,561, 2018. doi: https://doi.org/10.1029/2018GL079390.

A. V. Korolev and I. P. Mazin. Supersaturation of water vapor in clouds. *Journal of the Atmospheric Sciences*, 60(24):2957 – 2974, 2003. doi: https://doi.org/10.1175/1520-0469(2003)060<2957:SOWVIC>2.0.CO;2.

S. Kox, L. Bugliaro, and A. Ostler. Retrieval of cirrus cloud optical thickness and top altitude from geostationary remote sensing. *Atmospheric Measurement Techniques*, 7 (10):3233–3246, 2014. doi: 10.5194/amt-7-3233-2014.

M. Krämer, C. Schiller, A. Afchine, R. Bauer, I. Gensch, A. Mangold, S. Schlicht, N. Spelten, N. Sitnikov, S. Borrmann, M. de Reus, and P. Spichtinger. Ice supersaturations and cirrus cloud crystal numbers. *Atmospheric Chemistry and Physics*, 9(11):3505–3522, 2009. doi: 10.5194/acp-9-3505-2009.

M. Krautstrunk and A. Giez. *The Transition From FALCON to HALO Era Airborne Atmospheric Research*, pages 609–624. Springer Berlin Heidelberg, Berlin, Heidelberg, 2012. ISBN 978-3-642-30183-4. doi: 10.1007/978-3-642-30183-4_37.

K. Krüger, A. Schäfler, M. Wirth, M. Weissmann, and G. C. Craig. Vertical structure of the lower-stratospheric moist bias in the era5 reanalysis and its connection to mixing processes. *Atmospheric Chemistry and Physics*, 22(23):15559–15577, 2022. doi: 10.5194/acp-22-15559-2022.

M. Kübbeler, M. Hildebrandt, J. Meyer, C. Schiller, T. Hamburger, T. Jurkat, A. Minikin, A. Petzold, M. Rautenhaus, H. Schlager, U. Schumann, C. Voigt, P. Spichtinger, J.-F. Gayet, C. Gourbeyre, and M. Krämer. Thin and subvisible cirrus and contrails in a subsaturated environment. *Atmospheric Chemistry and Physics*, 11(12):5853–5865, 2011. doi: 10.5194/acp-11-5853-2011.

B. Kärcher. Formation and radiative forcing of contrail cirrus. *Nature Communications*, 2018.

B. Kärcher and C. Voigt. Susceptibility of contrail ice crystal numbers to aircraft soot particle emissions. *Geophysical Research Letters*, 44(15):8037–8046, 2017. doi: https://doi.org/10.1002/2017GL074949.

B. Kärcher, U. Burkhardt, A. Bier, L. Bock, and I. J. Ford. The microphysical pathway to contrail formation. *Journal of Geophysical Research: Atmospheres*, 120(15):7893–7927, 2015. doi: https://doi.org/10.1002/2015JD023491.

R. Lam, A. Sanchez-Gonzalez, M. Willson, P. Wirnsberger, M. Fortunato, F. Alet, S. Ravuri, T. Ewalds, Z. Eaton-Rosen, W. Hu, A. Merose, S. Hoyer, G. Holland, O. Vinyals, J. Stott, A. Pritzel, S. Mohamed, and P. Battaglia. Learning skillful medium-range global weather forecasting. *Science*, 382(6677):1416–1421, 2023. doi: 10.1126/science.adi2336.

N. Lamquin, C. J. Stubenrauch, K. Gierens, U. Burkhardt, and H. Smit. A global climatology of upper-tropospheric ice supersaturation occurrence inferred from the atmospheric infrared sounder calibrated by mozaic. *Atmospheric Chemistry and Physics*, 12(1):381–405, 2012. doi: 10.5194/acp-12-381-2012.

H. Lawrence, N. Bormann, I. Sandu, J. Day, J. Farnan, and P. Bauer. Use and impact of arctic observations in the ecmwf numerical weather prediction system. *Quarterly Journal of the Royal Meteorological Society*, 145(725):3432–3454, 2019. doi: https://doi.org/10.1002/qj.3628.

D. Lee, D. Fahey, A. Skowron, M. Allen, U. Burkhardt, Q. Chen, S. Doherty, S. Freeman, P. Forster, J. Fuglestvedt, A. Gettelman, R. De León, L. Lim, M. Lund, R. Millar, B. Owen, J. Penner, G. Pitari, M. Prather, R. Sausen, and L. Wilcox. The contribution of global aviation to anthropogenic climate forcing for 2000 to 2018. *Atmospheric Environment*, 244:117834, 2021. ISSN 1352-2310. doi: https://doi.org/10.1016/j.atmosenv.2020.117834.

D. S. Lee, D. W. Fahey, P. M. Forster, P. J. Newton, R. C. Wit, L. L. Lim, B. Owen, and R. Sausen. Aviation and global climate change in the 21st century. *Atmospheric Environment*, 43(22):3520–3537, 2009. ISSN 1352-2310. doi: https://doi.org/10.1016/j.atmosenv.2009.04.024.

H. Letu, H. Ishimoto, J. Riedi, T. Y. Nakajima, L. C.-Labonnote, A. J. Baran, T. M. Nagao, and M. Sekiguchi. Investigation of ice particle habits to be used for ice cloud remote sensing for the gcom-c satellite mission. *Atmospheric Chemistry and Physics*, 16 (18):12287–12303, 2016. doi: 10.5194/acp-16-12287-2016.

W. Li, M. Migliavacca, M. Forkel, J. M. C. Denissen, M. Reichstein, H. Yang, G. Duveiller, U. Weber, and R. Orth. Widespread increasing vegetation sensitivity to soil moisture. *Nature Communications*, 13, 2022. doi: https://doi.org/10.1038/s41467-022-31667-9.

W. Li, J. Pacheco-Labrador, M. Migliavacca, D. Miralles, A. H. van Dijke, M. Reichstein, M. Forkel, W. Zhang, C. Frankenberg, A. Panwar, Q. Zhang, U. Weber, P. Gentine, and R. Orth. Widespread and complex drought effects on vegetation physiology inferred from space. *Nature Communications*, 14, 2023a. doi: https://doi.org/10.1038/s41467-023-40226-9.

Y. Li, C. Mahnke, S. Rohs, U. Bundke, N. Spelten, G. Dekoutsidis, S. Groß, C. Voigt, U. Schumann, A. Petzold, and M. Krämer. Upper-tropospheric slightly ice-subsaturated regions: frequency of occurrence and statistical evidence for the appearance of contrail cirrus. *Atmospheric Chemistry and Physics*, 23(3):2251–2271, 2023b. doi: 10.5194/acp-23-2251-2023.

K. Liou. *An Introduction to Atmospheric Radiation.* Academic Press, San Diego, CA, USA and London, United Kingdom, 2nd edition, 2002. ISBN 9780124514515.

U. Lohmann and B. Gasparini. A cirrus cloud climate dial? *Science*, 357(6348):248–249, 2017. doi: 10.1126/science.aan3325.

S. Manabe and R. F. Strickler. Thermal equilibrium of the atmosphere with a convective adjustment. *Journal of Atmospheric Sciences*, 21(4):361 – 385, 1964. doi: https://doi.org/10.1175/1520-0469(1964)021<0361:TEOTAW>2.0.CO;2.

H. Mannstein and U. Schumann. Aircraft induced contrail cirrus over europe. *Meteorologische Zeitschrift*, 14(4):549–554, 09 2005. doi: 10.1127/0941-2948/2005/0058.

H. Mannstein, R. Meyer, and P. Wendling. Operational detection of contrails from noaa-avhrr-data. *International Journal of Remote Sensing*, 20(8):1641–1660, 1999. doi: 10.1080/014311699212650.

H. Mannstein, A. Brömser, and L. Bugliaro. Ground-based observations for the validation of contrails and cirrus detection in satellite imagery. *Atmospheric Measurement Techniques*, 3(3):655–669, 2010. doi: 10.5194/amt-3-655-2010.

B. Mayer and A. Kylling. Technical note: The libradtran software package for radiative transfer calculations - description and examples of use. *Atmospheric Chemistry and Physics*, 5(7):1855–1877, 2005. doi: 10.5194/acp-5-1855-2005.

J. Mayer, F. Ewald, L. Bugliaro, and C. Voigt. Cloud top thermodynamic phase from synergistic lidar-radar cloud products from polar orbiting satellites: Implications for observations from geostationary satellites. *Remote Sensing*, 15(7), 2023. ISSN 2072-4292. doi: 10.3390/rs15071742.

J. E. McDonald. The saturation adjustment in numerical modelling of fog. *Journal of Atmospheric Sciences*, 20(5):476 – 478, 1963. doi: https://doi.org/10.1175/1520-0469(1963)020<0476:TSAINM>2.0.CO;2.

G. M. McFarquhar and A. J. Heymsfield. The definition and significance of an effective radius for ice clouds. *Journal of the Atmospheric Sciences*, 55(11):2039 – 2052, 1998. doi: https://doi.org/10.1175/1520-0469(1998)055<2039:TDASOA>2.0.CO;2.

V. R. Meijer, L. Kulik, S. D. Eastham, F. Allroggen, R. L. Speth, S. Karaman, and S. R. H. Barrett. Contrail coverage over the united states before and during the covid-19 pandemic. *Environmental Research Letters*, 2022.

D. Meinert, E. Raschke, and R. Stuhlmann. Ein versuch zur erkennung von kondensstreifen in satellitenbildern unter verwendung kuenstlicher neuronaler netzwerke. abschlussbericht zum forschungsvorhaben einfluss von kondensstreifen auf den strahlungshaushalt ueber nordwesteuropa und dem nordatlantik. GKSS 97-E-50, 1997.

W. P. Menzel, R. A. Frey, H. Zhang, D. P. Wylie, C. C. Moeller, R. E. Holz, B. Maddux, B. A. Baum, K. I. Strabala, and L. E. Gumley. Modis global cloud-top pressure and amount estimation: Algorithm description and results. *Journal of Applied Meteorology and Climatology*, 47(4):1175 – 1198, 2008. doi: https://doi.org/10.1175/2007JAMC1705.1.

P. Minnis, J. K. Ayers, R. Palikonda, and D. Phan. Contrails, cirrus trends, and climate. *Journal of Climate*, 17(8):1671 – 1685, 2004. doi: https://doi.org/10.1175/1520-0442(2004)017<1671:CCTAC>2.0.CO;2.

J.-J. Morcrette and C. Jakob. The response of the ecmwf model to changes in the cloud overlap assumption. *Monthly Weather Review*, 128(6):1707 – 1732, 2000. doi: https://doi.org/10.1175/1520-0493(2000)128<1707:TROTEM>2.0.CO;2.

D. M. Murphy and T. Koop. Review of the vapour pressures of ice and supercooled water for atmospheric applications. *Quarterly Journal of the Royal Meteorological Society*, 131(608):1539–1565, 2005. doi: https://doi.org/10.1256/qj.04.94.

S. Müller, P. Hoor, F. Berkes, H. Bozem, M. Klingebiel, P. Reutter, H. G. J. Smit, M. Wendisch, P. Spichtinger, and S. Borrmann. In situ detection of stratosphere-troposphere exchange of cirrus particles in the midlatitudes. *Geophysical Research Letters*, 42(3):949–955, 2015. doi: https://doi.org/10.1002/2014GL062556.

T. Nakajima and M. D. King. Determination of the optical thickness and effective particle radius of clouds from reflected solar radiation measurements. part i: Theory. *Journal of Atmospheric Sciences*, 47(15):1878 – 1893, 1990. doi: https://doi.org/10.1175/1520-0469(1990)047<1878:DOTOTA>2.0.CO;2.

T. Nakajima and M. Tanaka. Effect of wind-generated waves on the transfer of solar radiation in the atmosphere-ocean system. *J. Quant. Spectrosc. Ra.*, 29:521–537, 1983. doi: https://doi.org/10.1016/0022-4073(83)90129-2.

A. Nuic, D. Poles, and V. Mouillet. Bada: An advanced aircraft performance model for present and future atm systems. *International Journal of Adaptive Control and Signal Processing*, 24(10):850–866, 2010. doi: https://doi.org/10.1002/acs.1176.

J. Ovarlez, J.-F. Gayet, K. Gierens, J. Ström, H. Ovarlez, F. Auriol, R. Busen, and U. Schumann. Water vapour measurements inside cirrus clouds in northern and southern hemispheres during inca. *Geophysical Research Letters*, 29(16):60–1–60–4, 2002. doi: https://doi.org/10.1029/2001GL014440.

R. Palikonda, P. Minnis, D. P. Duda, and H. Mannstein. Contrail coverage derived from 2001 avhrr data over the continental united states of america and surrounding areas. *Meteorologische Zeitschrift*, 14(4):525–536, 09 2005. doi: 10.1127/0941-2948/2005/0051.

R. Paoli and K. Shariff. Contrail modeling and simulation. *Annual Review of Fluid Mechanics*, 48(1):393–427, 2016. doi: 10.1146/annurev-fluid-010814-013619.

A. Petzold, V. Thouret, C. Gerbig, A. Zahn, C. A. M. Brenninkmeijer, M. Gallagher, M. Hermann, M. Pontaud, H. Ziereis, D. Boulanger, J. Marshall, P. Nédélec, H. G. J. Smit, U. Friess, J.-M. Flaud, A. Wahner, J.-P. Cammas, A. Volz-Thomas, and I. Team. Global-scale atmosphere monitoring by in-service aircraft – current achievements and future prospects of the european research infrastructure iagos. *Tellus B: Chemical and Physical Meteorology*, Jan 2015. doi: 10.3402/tellusb.v67.28452.

A. Petzold, P. Neis, M. Rütimann, S. Rohs, F. Berkes, H. G. J. Smit, M. Krämer, N. Spelten, P. Spichtinger, P. Nédélec, and A. Wahner. Ice-supersaturated air masses in the northern mid-latitudes from regular in situ observations by passenger aircraft: vertical distribution, seasonality and tropospheric fingerprint. *Atmospheric Chemistry and Physics*, 20(13):8157–8179, 2020. doi: 10.5194/acp-20-8157-2020.

D. Piontek, L. Bugliaro, J. Kar, U. Schumann, F. Marenco, M. Plu, and C. Voigt. The new volcanic ash satellite retrieval vacos using msg/seviri and artificial neural networks: 2. validation. *Remote Sensing*, 13(16), 2021a. ISSN 2072-4292. doi: 10.3390/rs13163128.

D. Piontek, L. Bugliaro, M. Schmidl, D. K. Zhou, and C. Voigt. The new volcanic ash satellite retrieval vacos using msg/seviri and artificial neural networks: 1. development. *Remote Sensing*, 13(16), 2021b. ISSN 2072-4292. doi: 10.3390/rs13163112.

D. Poll and U. Schumann. An estimation method for the fuel burn and other performance characteristics of civil transport aircraft during cruise: part 2, determining the aircraft's characteristic parameters. *The Aeronautical Journal*, 125(1284):296–340, 2021. doi: 10.1017/aer.2020.124.

R. Pouzolz, O. Schmitz, and H. Klingels. Evaluation of the climate impact reduction potential of the water-enhanced turbofan (wet) concept. *Aerospace*, 8(3), 2021. ISSN 2226-4310. doi: 10.3390/aerospace8030059.

H. Pruppacher and J. Klett. Microphysics of clouds and precipitation. In *Atmospheric and Oceanographic Sciences Library*, volume 18. Springer, 2010. ISBN 978-0-7923-4211-3.

M. Reichstein, G. Camps-Valls, B. Stevens, M. Jung, J. Denzler, N. Carvalhais, and Prabhat. Deep learning and process understanding for data-driven earth system science. *Nature*, page 195–204, 2019. doi: https://doi.org/10.1038/s41586-019-0912-1.

P. Reutter, P. Neis, S. Rohs, and B. Sauvage. Ice supersaturated regions: properties and validation of era-interim reanalysis with iagos in situ water vapour measurements. *Atmospheric Chemistry and Physics*, 20(2):787–804, 2020. doi: 10.5194/acp-20-787-2020.

M. Riese, F. Ploeger, A. Rap, B. Vogel, P. Konopka, M. Dameris, and P. Forster. Impact of uncertainties in atmospheric mixing on simulated utls composition and related radiative effects. *Journal of Geophysical Research: Atmospheres*, 117(D16), 2012. doi: https://doi.org/10.1029/2012JD017751.

M. Righi, J. Hendricks, U. Lohmann, C. G. Beer, V. Hahn, B. Heinold, R. Heller, M. Krämer, M. Ponater, C. Rolf, I. Tegen, and C. Voigt. Coupling aerosols to (cirrus) clouds in the global emac-made3 aerosol–climate model. *Geoscientific Model Development*, 13(3):1635–1661, 2020. doi: 10.5194/gmd-13-1635-2020.

G. Rädel and K. P. Shine. Radiative forcing by persistent contrails and its dependence on cruise altitudes. *Journal of Geophysical Research: Atmospheres*, 113(D7), 2008. doi: https://doi.org/10.1029/2007JD009117.

I. Sanz-Morère, S. D. Eastham, F. Allroggen, R. L. Speth, and S. R. H. Barrett. Impacts of multi-layer overlap on contrail radiative forcing. *Atmospheric Chemistry and Physics*, 21(3):1649–1681, 2021. doi: 10.5194/acp-21-1649-2021.

R. Sausen, S. Hofer, K. Gierens, L. Bugliaro, R. Ehrmanntraut, I. Sitova, K. Walczak, A. Burridge-Diesing, M. Bowman, and N. Miller. Can we successfully avoid persistent contrails by small altitude adjustments of flights in the real world? *Meteorologische Zeitschrift*, pages –, 07 2023. doi: 10.1127/metz/2023/1157.

H. Schlager, P. Konopka, P. Schulte, U. Schumann, H. Ziereis, F. Arnold, M. Klemm, D. E. Hagen, P. D. Whitefield, and J. Ovarlez. In situ observations of air traffic emission signatures in the north atlantic flight corridor. *Journal of Geophysical Research: Atmospheres*, 102(D9):10739–10750, 1997. doi: https://doi.org/10.1029/96JD03748.

J. Schmetz, P. Pili, S. Tjemkes, D. Just, J. Kerkmann, S. Rota, and A. Ratier. An introduction to meteosat second generation (msg). *Bulletin of the American Meteorological Society*, 83(7):977 – 992, 2002. doi: https://doi.org/10.1175/1520-0477(2002)083<0977:AITMSG>2.3.CO;2.

T. J. Schmit, S. J. Goodman, M. M. Gunshor, J. Sieglaff, A. K. Heidinger, A. S. Bachmeier, S. S. Lindstrom, A. Terborg, J. Feltz, K. Bah, S. Rudlosky, D. T. Lindsey, R. M. Rabin, and C. C. Schmidt. Rapid refresh information of significant events: Preparing users for the next generation of geostationary operational satellites. *Bulletin of the American Meteorological Society*, 96(4):561 – 576, 2015. doi: https://doi.org/10.1175/BAMS-D-13-00210.1.

F. Schröder, C. A. Brock, R. Baumann, A. Petzold, R. Busen, P. Schulte, and M. Fiebig. In situ studies on volatile jet exhaust particle emissions: Impact of fuel sulfur content and environmental conditions on nuclei mode aerosols. *Journal of Geophysical Research: Atmospheres*, 105(D15):19941–19954, 2000. doi: https://doi.org/10.1029/2000JD900112.

F. Schröder, B. Kärcher, M. Fiebig, and A. Petzold. Aerosol states in the free troposphere at northern midlatitudes. *Journal of Geophysical Research: Atmospheres*, 107(D21):LAC 8–1–LAC 8–8, 2002. doi: https://doi.org/10.1029/2000JD000194.

U. Schumann. On conditions for contrail formation from aircraft exhausts. *Meteorologische Zeitschrift*, 5(1):4–23, 03 1996. doi: 10.1127/metz/5/1996/4.

U. Schumann. A contrail cirrus prediction model. *Geoscientific Model Development*, 5(3): 543–580, 2012. doi: 10.5194/gmd-5-543-2012.

U. Schumann, H. Schlager, F. Arnold, R. Baumann, P. Haschberger, and O. Klemm. Dilution of aircraft exhaust plumes at cruise altitudes. *Atmospheric Environment*, 32 (18):3097–3103, 1998. ISSN 1352-2310. doi: https://doi.org/10.1016/S1352-2310(97) 00455-X.

U. Schumann, B. Mayer, K. Graf, and H. Mannstein. A parametric radiative forcing model for contrail cirrus. *Journal of Applied Meteorology and Climatology*, 51(7):1391 – 1406, 2012. doi: https://doi.org/10.1175/JAMC-D-11-0242.1.

U. Schumann, P. Jeßberger, and C. Voigt. Contrail ice particles in aircraft wakes and their climatic importance. *Geophysical Research Letters*, 40(11):2867–2872, 2013. doi: https://doi.org/10.1002/grl.50539.

U. Schumann, J. E. Penner, Y. Chen, C. Zhou, and K. Graf. Dehydration effects from contrails in a coupled contrail–climate model. *Atmospheric Chemistry and Physics*, 15 (19):11179–11199, 2015. doi: 10.5194/acp-15-11179-2015.

U. Schumann, R. Baumann, D. Baumgardner, S. T. Bedka, D. P. Duda, V. Freudenthaler, J.-F. Gayet, A. J. Heymsfield, P. Minnis, M. Quante, E. Raschke, H. Schlager, M. Vázquez-Navarro, C. Voigt, and Z. Wang. Properties of individual contrails: a compilation of observations and some comparisons. *Atmospheric Chemistry and Physics*, 17 (1):403–438, 2017. doi: 10.5194/acp-17-403-2017.

U. Schumann, L. Bugliaro, A. Dörnbrack, R. Baumann, and C. Voigt. Aviation contrail cirrus and radiative forcing over europe during 6 months of covid-19. *Geophysical Research Letters*, 48(8):e2021GL092771, 2021a. doi: https://doi.org/10.1029/2021GL092771. e2021GL092771 2021GL092771.

U. Schumann, I. Poll, R. Teoh, R. Koelle, E. Spinielli, J. Molloy, G. S. Koudis, R. Baumann, L. Bugliaro, M. Stettler, and C. Voigt. Air traffic and contrail changes over europe during covid-19: a model study. *Atmospheric Chemistry and Physics*, 21(10):7429–7450, 2021b. doi: 10.5194/acp-21-7429-2021.

A. J. Simmons, P. Poli, D. P. Dee, P. Berrisford, H. Hersbach, S. Kobayashi, and C. Peubey. Estimating low-frequency variability and trends in atmospheric temperature using era-interim. *Quarterly Journal of the Royal Meteorological Society*, 140(679):329–353, 2014. doi: https://doi.org/10.1002/qj.2317.

W. L. Smith, S. Ackerman, H. Revercomb, H. Huang, D. H. DeSlover, W. Feltz, L. Gumley, and A. Collard. Infrared spectral absorption of nearly invisible cirrus clouds. *Geophysical Research Letters*, 25(8):1137–1140, 1998. doi: https://doi.org/10.1029/97GL03491.

D. Sperber and K. Gierens. Towards a more reliable forecast of ice supersaturation: concept of a one-moment ice-cloud scheme that avoids saturation adjustment. *Atmospheric Chemistry and Physics*, 23(24):15609–15627, 2023. doi: 10.5194/acp-23-15609-2023.

P. Spichtinger, K. Gierens, U. Leiterer, and H. Dier. Ice supersaturation in the tropopause region over lindenberg, germany. *Meteorologische Zeitschrift*, 12(3):143–156, 06 2003. doi: 10.1127/0941-2948/2003/0012-0143.

P. Spichtinger, K. Gierens, H. G. J. Smit, J. Ovarlez, and J.-F. Gayet. On the distribution of relative humidity in cirrus clouds. *Atmospheric Chemistry and Physics*, 4(3):639–647, 2004. doi: 10.5194/acp-4-639-2004.

K. Stamnes, S.-C. Tsay, W. Wiscombe, and I. Laszlo. *DISORT, a general-purpose Fortran program for discrete-ordinate-method radiative transfer in scattering and emitting layered media: documentation of methodology.* Tech. rep., Dept. of Physics and Engineering Physics, Stevens Institute of Technology, 2000.

F. Stordal, G. Myhre, E. J. G. Stordal, W. B. Rossow, D. S. Lee, D. W. Arlander, and T. Svendby. Is there a trend in cirrus cloud cover due to aircraft traffic? *Atmospheric Chemistry and Physics*, 5(8):2155–2162, 2005. doi: 10.5194/acp-5-2155-2005.

J. Strandgren, L. Bugliaro, F. Sehnke, and L. Schröder. Cirrus cloud retrieval with msg/seviri using artificial neural networks. *Atmospheric Measurement Techniques*, 10 (9):3547–3573, 2017a. doi: 10.5194/amt-10-3547-2017.

J. Strandgren, J. Fricker, and L. Bugliaro. Characterisation of the artificial neural network cips for cirrus cloud remote sensing with msg/seviri. *Atmospheric Measurement Techniques*, 10(11):4317–4339, 2017b. doi: 10.5194/amt-10-4317-2017.

G. Stratmann, H. Ziereis, P. Stock, C. Brenninkmeijer, A. Zahn, A. Rauthe-Schöch, P. Velthoven, H. Schlager, and A. Volz-Thomas. No and noy in the upper troposphere: Nine years of caribic measurements onboard a passenger aircraft. *Atmospheric Environment*, 133:93–111, 2016. ISSN 1352-2310. doi: https://doi.org/10.1016/j.atmosenv.2016.02.035.

L. Ström and K. Gierens. First simulations of cryoplane contrails. *Journal of Geophysical Research: Atmospheres*, 107(D18):AAC 2–1–AAC 2–13, 2002. doi: https://doi.org/10.1029/2001JD000838.

N. Stuber, P. Forster, G. Rädel, and K. Shine. The importance of the diurnal and annual cycle of air traffic for contrail radiative forcing. *Nature*, 2006.

R. Teoh, M. E. Stettler, A. Majumdar, U. Schumann, B. Graves, and A. M. Boies. A methodology to relate black carbon particle number and mass emissions. *Journal of Aerosol Science*, 132:44–59, 2019. ISSN 0021-8502. doi: https://doi.org/10.1016/j.jaerosci.2019.03.006.

R. Teoh, U. Schumann, A. Majumdar, and M. E. J. Stettler. Mitigating the climate forcing of aircraft contrails by small-scale diversions and technology adoption. *Environmental Science & Technology*, 54(5):2941–2950, 2020. doi: 10.1021/acs.est.9b05608. PMID: 32048502.

R. Teoh, U. Schumann, E. Gryspeerdt, M. Shapiro, J. Molloy, G. Koudis, C. Voigt, and M. E. J. Stettler. Aviation contrail climate effects in the north atlantic from 2016 to 2021. *Atmospheric Chemistry and Physics*, 22(16):10919–10935, 2022a. doi: 10.5194/acp-22-10919-2022.

R. Teoh, U. Schumann, C. Voigt, T. Schripp, M. Shapiro, Z. Engberg, J. Molloy, G. Koudis, and M. E. J. Stettler. Targeted use of sustainable aviation fuel to maximize climate benefits. *Environmental Science & Technology*, 56(23):17246–17255, 2022b. doi: 10.1021/acs.est.2c05781. PMID: 36394538.

R. Teoh, Z. Engberg, U. Schumann, C. Voigt, M. Shapiro, S. Rohs, and M. Stettler. Global aviation contrail climate effects from 2019 to 2021. *EGUsphere*, 2023:1–32, 2023. doi: 10.5194/egusphere-2023-1859.

M. Tesche, P. Achtert, P. Glantz, and K. J. Noone. Aviation effects on already-existing cirrus clouds. *Nature Communications*, 2016.

A. M. Tompkins, K. Gierens, and G. Rädel. Ice supersaturation in the ecmwf integrated forecast system. *Quarterly Journal of the Royal Meteorological Society*, 133(622):53–63, 2007. doi: https://doi.org/10.1002/qj.14.

S. Unterstrasser. Properties of young contrails – a parametrisation based on large-eddy simulations. *Atmospheric Chemistry and Physics*, 16(4):2059–2082, 2016. doi: 10.5194/acp-16-2059-2016.

S. Unterstrasser, K. Gierens, I. Sölch, and M. Lainer. Numerical simulations of homogeneously nucleated natural cirrus and contrail-cirrus. part 1: How different are they? *Meteorologische Zeitschrift*, 26(6):621–642, 12 2017a. doi: 10.1127/metz/2016/0777.

S. Unterstrasser, K. Gierens, I. Sölch, and M. Wirth. Numerical simulations of homogeneously nucleated natural cirrus and contrail-cirrus. part 2: Interaction on local scale. *Meteorologische Zeitschrift*, 26(6):643–661, 12 2017b. doi: 10.1127/metz/2016/0780.

B. Urbanek, S. Groß, M. Wirth, C. Rolf, M. Krämer, and C. Voigt. High depolarization ratios of naturally occurring cirrus clouds near air traffic regions over europe. *Geophysical Research Letters*, 45(23):13,166–13,172, 2018. doi: https://doi.org/10.1029/2018GL079345.

R. van der Linden, P. Knippertz, A. H. Fink, B. Ingleby, M. Maranan, and A. Benedetti. The influence of dacciwa radiosonde data on the quality of ecmwf analyses and forecasts over southern west africa. *Quarterly Journal of the Royal Meteorological Society*, 146 (729):1719–1739, 2020. doi: https://doi.org/10.1002/qj.3763.

M. Vazquez-Navarro, H. Mannstein, and B. Mayer. An automatic contrail tracking algorithm. *Atmospheric Measurement Techniques*, 3(4):1089–1101, 2010. doi: 10.5194/amt-3-1089-2010.

M. Vázquez-Navarro, B. Mayer, and H. Mannstein. A fast method for the retrieval of integrated longwave and shortwave top-of-atmosphere upwelling irradiances from msg/seviri (rrums). *Atmospheric Measurement Techniques*, 6(10):2627–2640, 2013. doi: 10.5194/amt-6-2627-2013.

M. Vázquez-Navarro, H. Mannstein, and S. Kox. Contrail life cycle and properties from 1 year of msg/seviri rapid-scan images. *Atmospheric Chemistry and Physics*, 15(15): 8739–8749, 2015. doi: 10.5194/acp-15-8739-2015.

P. Verma and U. Burkhardt. Contrail formation within cirrus: Icon-lem simulations of the impact of cirrus cloud properties on contrail formation. *Atmospheric Chemistry and Physics*, 22(13):8819–8842, 2022. doi: 10.5194/acp-22-8819-2022.

C. Voigt, U. Schumann, T. Jurkat, D. Schäuble, H. Schlager, A. Petzold, J.-F. Gayet, M. Krämer, J. Schneider, S. Borrmann, J. Schmale, P. Jessberger, T. Hamburger, M. Lichtenstern, M. Scheibe, C. Gourbeyre, J. Meyer, M. Kübbeler, W. Frey, H. Kalesse, T. Butler, M. G. Lawrence, F. Holzäpfel, F. Arnold, M. Wendisch, A. Döpelheuer, K. Gottschaldt, R. Baumann, M. Zöger, I. Sölch, M. Rautenhaus, and A. Dörnbrack. In-situ observations of young contrails – overview and selected results from the concert campaign. *Atmospheric Chemistry and Physics*, 10(18):9039–9056, 2010. doi: 10.5194/acp-10-9039-2010.

C. Voigt, U. Schumann, P. Jessberger, T. Jurkat, A. Petzold, J.-F. Gayet, M. Krämer, T. Thornberry, and D. W. Fahey. Extinction and optical depth of contrails. *Geophysical Research Letters*, 38(11), 2011. doi: https://doi.org/10.1029/2011GL047189.

C. Voigt, U. Schumann, A. Minikin, A. Abdelmonem, A. Afchine, S. Borrmann, M. Boettcher, B. Buchholz, L. Bugliaro, A. Costa, J. Curtius, M. Dollner, A. Dörnbrack, V. Dreiling, V. Ebert, A. Ehrlich, A. Fix, L. Forster, F. Frank, D. Fütterer, A. Giez, K. Graf, J.-U. Grooß, S. Groß, K. Heimerl, B. Heinold, T. Hüneke, E. Järvinen, T. Jurkat, S. Kaufmann, M. Kenntner, M. Klingebiel, T. Klimach, R. Kohl, M. Krämer, T. C. Krisna, A. Luebke, B. Mayer, S. Mertes, S. Molleker, A. Petzold, K. Pfeilsticker, M. Port, M. Rapp, P. Reutter, C. Rolf, D. Rose, D. Sauer, A. Schäfler, R. Schlage, M. Schnaiter, J. Schneider, N. Spelten, P. Spichtinger, P. Stock, A. Walser, R. Weigel, B. Weinzierl, M. Wendisch, F. Werner, H. Wernli, M. Wirth, A. Zahn, H. Ziereis, and M. Zöger. Ml-cirrus: The airborne experiment on natural cirrus and contrail cirrus with the high-altitude long-range research aircraft halo. *Bulletin of the American Meteorological Society*, 98(2):271 – 288, 2017. doi: https://doi.org/10.1175/BAMS-D-15-00213.1.

C. Voigt, J. Kleine, D. Sauer, R. H. Moore, T. Bräuer, P. L. Clercq, S. Kaufmann, M. Scheibe, T. Jurkat-Witschas, M. Aigner, U. Bauder, Y. Boose, S. Borrmann, E. Crosbie, G. S. Diskin, J. DiGangi, V. Hahn, C. Heckl, F. Huber, J. B. Nowak, M. Rapp, B. Rauch, C. Robinson, T. Schripp, M. Shook, E. Winstead, L. Ziemba, H. Schlager, and B. E. Anderson. Cleaner burning aviation fuels can reduce contrail cloudiness. *communications earth and environment*, 2021.

C.-C. Wang. On the calculation and correction of equitable threat score for model quantitative precipitation forecasts for small verification areas: The example of taiwan. *Weather and Forecasting*, 29(4):788 – 798, 2014. doi: https://doi.org/10.1175/WAF-D-13-00087.1.

Z. Wang, L. Bugliaro, T. Jurkat-Witschas, R. Heller, U. Burkhardt, H. Ziereis, G. Dekoutsidis, M. Wirth, S. Groß, S. Kirschler, S. Kaufmann, and C. Voigt. Observations of microphysical properties and radiative effects of a contrail cirrus outbreak over the north atlantic. *Atmospheric Chemistry and Physics*, 23(3):1941–1961, 2023. doi: 10.5194/acp-23-1941-2023.

Z. Wang, H. Letu, H. Shang, and L. Bugliaro. Technical note: Retrieval of the supercooled liquid fraction in mixed-phase clouds from himawari-8 observations. *EGUsphere*, 2024: 1–24, 2024. doi: 10.5194/egusphere-2023-2667.

B. A. Wielicki, B. R. Barkstrom, E. F. Harrison, R. B. Lee, G. L. Smith, and J. E. Cooper. Clouds and the earth's radiant energy system (ceres): An earth observing system experiment. *Bulletin of the American Meteorological Society*, 77(5):853 – 868, 1996. doi: https://doi.org/10.1175/1520-0477(1996)077<0853:CATERE>2.0.CO;2.

L. Wilhelm, K. Gierens, and S. Rohs. Meteorological conditions that promote persistent contrails. *Applied Sciences*, 12(9), 2022. ISSN 2076-3417. doi: 10.3390/app12094450.

D. R. Wilson and S. P. Ballard. A microphysically based precipitation scheme for the uk meteorological office unified model. *Quarterly Journal of the Royal Meteorological Society*, 125(557):1607–1636, 1999. doi: https://doi.org/10.1002/qj.49712555707.

M. Wirth, A. Fix, P. Mahnke, H. Schwarzer, F. Schrandt, and G. Ehret. The airborne multi-wavelength water vapor differential absorption lidar wales: system design and performance. *Appl. Phys. B*, 96:201–213, 2009. doi: https://doi.org/10.1007/s00340-009-3365-7.

P. Yang, K.-N. Liou, L. Bi, C. Liu, B. Yi, and B. A. Baum. On the radiative properties of ice clouds: Light scattering, remote sensing, and radiation parameterization. *Advances in Atmospheric Sciences*, 32:32–63, 2015. doi: https://doi.org/10.1007/s00376-014-0011-z.

P. Yang, S. Hioki, M. Saito, C.-P. Kuo, B. A. Baum, and K.-N. Liou. A review of ice cloud optical property models for passive satellite remote sensing. *Atmosphere*, 9(12), 2018. ISSN 2073-4433. doi: 10.3390/atmos9120499.

G. Zhang, J. Zhang, and J. Shang. Contrail recognition with convolutional neural network and contrail parameterizations evaluation. *SOLA*, 14:132–137, 2018. doi: 10.2151/sola.2018-023.

H. Ziereis, P. Hoor, J.-U. Grooß, A. Zahn, G. Stratmann, P. Stock, M. Lichtenstern, J. Krause, V. Bense, A. Afchine, C. Rolf, W. Woiwode, M. Braun, J. Ungermann, A. Marsing, C. Voigt, A. Engel, B.-M. Sinnhuber, and H. Oelhaf. Redistribution of total reactive nitrogen in the lowermost arctic stratosphere during the cold winter 2015/2016. *Atmospheric Chemistry and Physics*, 22(5):3631–3654, 2022. doi: 10.5194/acp-22-3631-2022.

Acknowledgements

The completion of this thesis owes to the invaluable guidance and support provided by numerous individuals. To begin, I want to thank Prof. Dr. Christiane Voigt who gave me the opportunity to start my doctoral research at the Institute of Atmospheric Physics of German Aerospace Center, always stayed behind me no matter where I would like to go or what kind of difficulty I met, and inspired me about my future academic career. Thank you 3000 times! Next, I express profound gratitude to Prof. Dr. Bernhard Mayer, for his supervision of my work, his essential guidance in the research direction, and indispensable feedback and comments on my thesis. Also, I want to express my deep appreciation to Dr. Luca Bugliaro, who shared his time, patience and knowledge with me. He always had an open door for me to discuss questions, and he thoroughly reviewed all my thesis, papers, posters, and presentations. It was a huge pleasure to work with you.

Furthermore, I am thankful to numerous other people who helped me in one way or another. To my mentor Dr. Ulrike Burkhardt for sharing her knowledge on cirrus cloud conditions and evolution and ice supersaturation parameterization. To Prof. Dr. Ulrich Schumann for sharing his expertise on contrail cirrus prediction model CoCiP simulations. To Dr. Klaus Gierens for introducing me to the atmospheric humidity correction using dynamical states. To Prof. Dr. Michaela I. Hegglin for providing the guidance on humidity correction after we met by chances during the conference. To Dr. Romy Heller for providing all the aircraft in situ sets of the ML-CIRRUS campaign. To Dr. Helmut Ziereis for providing the airborne measurements of nitrogen oxide and the sum of all reactive nitrogen species. To Dr. Martin Wirth, Dr. Silke Groß, and Georgios Dekoutsidis for providing the lidar measurements of contrail cirrus and relative humidity also during the ML-CIRRUS campaign. To Dr. Susanne Rohs and Dr. Andreas Petzold for providing long term IAGOS measurements. To Björn Brötz, Winfried Beer and Natalie Keur for helping me with all kinds of technical and administrative issues, respectively. To Dr. Andreas Schäfler and Dr. Simon Kirschler for helpful comments on parts of this manuscript. I would like to stress again my gratitude to all the co-authors of the presented papers for discussing the results and reviewing the paper drafts.

I am thankful to Dr. Tina Jurkat-Witschas and Dr. Benjamin Witschas for their care and kindness not only as my colleagues but also my landlords. To my office colleagues Dr. Dennis Piontek, Rebecca Dischl, Johannes Lucke, Manuel Moser, Gregor Neumann, and Deniz Menekay as well as Johanna Mayer, Dr. Tiziana Bräuer and all members of the cloud physics department for a productive and always enjoyable working environment,

and extended parties during the free time.

This work was financially supported by DLR/DAAD Research Fellowship – Doctoral Studies in Germany from the joint program of DLR and Deutscher Akademischer Austauschdienst (German Academic Exchange Service) under grant agreement No. 57540125. I am also grateful to European Organisation for the Exploitation of Meteorological Satellites (EUMETSAT) and ECMWF for providing the satellite and model data, respectively. In addition, I am thankful to the "DLR Graduate Program" for letting me participate in various conferences and workshops.

A heartfelt thank you to my parents, Fei Wang and Lanfang Jia, for their unwavering belief in me and their steadfast support from the very start. Thank you immensely! Thanks for the close company from Siyuan Wang while I was writing this thesis. I dedicate this thesis to my beloved grandparents, Dianchen Wang and Fengmin Wang, who have sadly passed away during my three years of studying abroad. Your memory will forever remain in my heart.